



UNIVERSIDADE ESTADUAL DE CAMPINAS
Instituto de Física “Gleb Wataghin”

RODRIGO CEZAR DE CAMPOS FERREIRA

ENGINEERING MOLECULAR NANOSTRUCTURES WITH
PORPHYRIN DERIVATIVES ON WELL-DEFINED SURFACES:
THE ROLE OF MOLECULE-SUBSTRATE INTERACTION

ENGENHARIA DE NANOESTRUTURAS MOLECULARES COM
DERIVADOS DE PORFIRINA EM SUPERFÍCIES BEM
DEFINIDAS: O PAPEL DA INTERAÇÃO
MOLECULA-SUBSTRATO

Campinas
2020

RODRIGO CEZAR DE CAMPOS FERREIRA

ENGINEERING MOLECULAR NANOSTRUCTURES WITH PORPHYRIN
DERIVATIVES ON WELL-DEFINED SURFACES: THE ROLE OF
MOLECULE-SUBSTRATE INTERACTION

ENGENHARIA DE NANOESTRUTURAS MOLECULARES COM DERIVADOS
DE PORFIRINA EM SUPERFÍCIES BEM DEFINIDAS: O PAPEL DA
INTERAÇÃO MOLÉCULA-SUBSTRATO

Tese de Doutorado apresentada ao Instituto de Física “Gleb Wataghin” da Universidade Estadual de Campinas como parte dos requisitos para a obtenção do título de Doutor em Ciências, na área de Física.

Thesis presented to the Institute of Physics “Gleb Wataghin” of the University of Campinas in partial fulfillment of the requirements for the degree of Doctor in Science, in the field of Physics.

Supervisor/Orientador: Prof. Dr. Abner de Siervo

ESTE EXEMPLAR CORRESPONDE À
VERSÃO FINAL DA TESE DE DOUTORADO
DEFENDIDA POR RODRIGO CEZAR DE
CAMPOS FERREIRA E ORIENTADA PELO
PROF. DR. ABNER DE SIERVO.

Campinas
2020

Ficha catalográfica
Universidade Estadual de Campinas
Biblioteca do Instituto de Física Gleb Wataghin
Lucimeire de Oliveira Silva da Rocha - CRB 8/9174

F413e Ferreira, Rodrigo Cezar de Campos, 1987-
Engineering molecular nanostructures with porphyrin derivatives on well-defined surfaces : the role of molecule-substrate interaction / Rodrigo Cezar de Campos Ferreira. – Campinas, SP : [s.n.], 2020.

Orientador: Abner de Siervo.

Tese (doutorado) – Universidade Estadual de Campinas, Instituto de Física Gleb Wataghin.

1. Porfirinas. 2. Reação de acoplamento de Ullmann. 3. Microscopia de tunelamento de elétrons. 4. Espectroscopia fotoeletrônica de raio X. I. Siervo, Abner de, 1972-. II. Universidade Estadual de Campinas. Instituto de Física Gleb Wataghin. III. Título.

Informações para Biblioteca Digital

Título em outro idioma: Engenharia de nanoestruturas moleculares com derivados de porfirina em superfícies bem definidas : o papel da interação molécula-substrato

Palavras-chave em inglês:

Porphyrins

Ullmann coupling reaction

Scanning tunneling microscopy

X-ray photoelectron spectroscopy

Área de concentração: Física

Titulação: Doutor em Ciências

Banca examinadora:

Abner de Siervo [Orientador]

Edmar Avellar Soares

Carlos César Bof Bufon

Júlio Criginski Cezar

Tulio Costa Rizuti da Rocha

Data de defesa: 27-11-2020

Programa de Pós-Graduação: Física

Identificação e informações acadêmicas do(a) aluno(a)

- ORCID do autor: <https://orcid.org/0000-0002-9866-7238>

- Currículo Lattes do autor: <http://lattes.cnpq.br/2688652045158459>



UNIVERSIDADE ESTADUAL DE CAMPINAS
Instituto de Física “Gleb Wataghin”
FOLHA DE APROVAÇÃO

A Comissão Julgadora dos trabalhos de Defesa de Tese de Doutorado, composta pelos Professores Doutores a seguir descritos, em sessão pública realizada em 27 de novembro de 2020, considerou o candidato Rodrigo Cezar de Campos Ferreira aprovado.

Prof. Dr. Abner de Siervo

Presidente da Comissão Julgadora

Prof. Dr. Edmar Avellar Soares

ICEx/UFMG

Dr. Carlos César Bof Bufon

LNNano/CNPEN

Dr. Júlio Criginski César

LNLS/CNPEN

Dr. Tulio Costa Rizuti da Rocha

LNLS/CNPEN

A Ata de Defesa com as respectivas assinaturas dos membros encontra-se no SIGA/Sistema de Fluxo de Dissertações/Teses e na Secretaria do Programa de Pós-Graduação em Física do Instituto de Física “Gleb Wataghin” .

Campinas, 27 de novembro de 2020

Agradecimentos

Durante todos estes anos de graduação e pós graduação tive a oportunidade e felicidade de trabalhar com pessoas excepcionais que me inspiraram e, acima de tudo, incentivaram a continuar acreditando neste tão longo e complexo caminho na academia. Foram muitas experiências engrandecedoras e necessárias para que eu pudesse formar o profissional que sou hoje.

Gostaria primeiramente de agradecer, em especial, ao meu orientador Prof. Abner de Siervo por sua imensa dedicação e paciência em ensinar, além da motivação e conhecimentos que sempre me transmitiu. Foi uma longa jornada desde o mestrado trabalhando contigo e com todos os nossos colaboradores que fizemos neste período e tenho certeza que convivi e aprendi entre os melhores.

Sou grato também a todos os membros do Grupo de Física de Superfícies com quem tive contato: ao Prof. Richard Landers e suas sábias palavras; aos técnicos e ex-técnicos Terezinha, Rita, Edson e Idalício que sempre mantiveram o ambiente de trabalho bastante agradável; a todos os alunos e ex-alunos Luís, Lucas, Alisson, Jean, Nataly, Gabriela e Isabela pelos momentos de bate papo descontraído no café. Agradeço também a todos os funcionários em geral do IFGW, que mantêm a estrutura e funcionamento da instituição e que muitas vezes passam despercebidos.

Agradeço também a forma como fui bem recebido no grupo do Prof. Hans-Peter Steinrück na FAU-Erlangen durante o período de sanduíche. Obrigado a todos do grupo, em especial: Dr. Hubertus Marbach por me orientar, aos colegas Michael Lepper, Jan Kuliga, Stephen Massicot, Rajan Adhikari.

Aos colaboradores que tiveram uma participação fundamental nesta tese: Juan Moreno-López, Alejandro Paz e Duncan Mowbray.

Também agradeço ao órgão de fomento CNPq pelo apoio indispensável a mim e a toda a comunidade de estudantes que, apesar de tudo, lutam pelos seus ideais, pela ciência e desenvolvimento do país e à Coordenação de Aperfeiçoamento de Pessoal de Nível Superior - Brasil (CAPES) - Código de Financiamento 001.

E por fim, agradeço principalmente a minha família pelo apoio durante todos esses anos na universidade, por acreditarem em mim e em minhas escolhas. Meu pai João e minha mãe Tânia, sem vocês eu jamais chegaria aqui. Obrigado Rayanna, vó Nina, Tê. Muito obrigado minha parceira Vanessa que esteve ao meu lado nestes 4 anos, caminhar contigo foi muito mais fácil, você é a paz na minha guerra.

Abstract

The bottom-up approach for the synthesis of nanostructures is a promising field of nanoscience that has been gaining prominence in the last 20 years. The basic idea is to promote the assembly of nano “building blocks” (atoms and/or molecules) with the intention of construct larger and more elaborated structures that show interesting physical-chemical properties and that are applicable in the most diverse areas of nanotechnology. When synthesis reactions are confined to well-defined surfaces, the so-called “on-surface synthesis”, there is a high chance of forming low-dimensional materials, such as graphene (Gr), graphene nanoribbons, hexagonal boron nitride (*h*BN), nanoporous molecular networks, among others. To obtain these types of nanoarchitecture, a widely used technique is the polymerization via on-surface Ullmann coupling reaction. Particularly, it is a process that involves reactivity between molecular precursors and substrate, which motivates the scientific community to study and understand the fundamental physical-chemical phenomena involved.

In this work, we chose to use free-base porphyrin molecules as our elementary precursors, which are very versatile structures from a structural and chemical perspective: the 5,10,15,20-(tetra-4-chlorophenyl)porphyrin (Cl₄TPP) and the 5,10,15,20-(tetra-4-cyanophenyl)porphyrin (2H-TCNPP). Thus, we studied the behavior of both precursors on different reactive metallic surfaces: Cu (111), Ag (111) and Gr on Ir (111), following the adsorption configuration of molecules, as well as mobility, chemical changes and by-products of the reactions as a function of temperature. The studies were carried out in an appropriate ultra-high vacuum (UHV) environment by means of combined experimental techniques of scanning tunneling microscopy (STM) and X-ray photoemission spectroscopy (XPS), in addition to complementary calculations and simulations by density functional theory (DFT).

The results showed that the molecule-substrate interaction present different degrees of intensity on each surface (Gr < Ag < Cu) so the halogen dissociation from Cl₄TPP also follows this hierarchy through the on-surface Ullmann reaction. On Cu (111), we verified a distorted adsorption configuration (“inverted structure”) for the free-base porphyrins due to the covalent interaction with the surface, which contributed to hinder the formation of a large two-dimensional framework. For the Ag (111) and Gr / Ir (111) cases, the weak molecule-substrate interaction favored the diffusion and reorganization of the precursors on highly compact 2D supramolecular networks. The results also showed that the availability of adatoms on surface is an important factor for the precise growth control of these nanoarchitectures. Remarkably, for the 2H-TCNPP case on Cu (111) within the presence of Pd, we observed the formation of a two-dimensional framework never seen on similar experiments in the literature.

Resumo

A técnica de *bottom-up* para síntese de nanoestruturas é um promissor campo da nanociência que vem ganhando bastante destaque nos últimos 20 anos. A idéia básica é promover o agrupamento de “nanoblocos” de construção (átomos e/ou moléculas) com a intenção de construir estruturas maiores e mais elaboradas que apresentem propriedades físico-químicas interessantes e que sejam aplicáveis nas mais diversas áreas da nanotecnologia. Quando as reações de síntese são confinadas em superfícies bem definidas, há grande possibilidade de formação de materiais de baixa dimensionalidade, tais como grafeno (Gr), nanofitas de grafeno, nitreto de boro hexagonal (*h*BN), redes moleculares nanoporosas, entre outros. Para obtenção destas nanoarquiteturas, uma técnica amplamente utilizada é a polimerização via reação de Ullmann em superfícies. Este é, particularmente, um processo que envolve o grau de reatividade dos precursores moleculares com o substrato, o que motiva a comunidade científica a buscar compreender os fenômenos físico-químicos fundamentais envolvidos.

Neste trabalho, escolhemos utilizar moléculas baseadas em porfirinas de base livre como sendo nossos precursores elementares, que são estruturas muito versáteis do ponto de vista estrutural e químico: a 5,10,15,20-(tetra-4-clorofenil)porfirina (Cl_4TPP) e a 5,10,15,20-(tetra-4-cianofenil)porfirina (2H-TCNPP). Assim, estudamos o comportamento de ambas em diferentes superfícies metálicas reativas: Cu(111), Ag(111) e Gr sobre Ir(111), acompanhando a configuração de adsorção das moléculas, bem como a mobilidade e as mudanças químicas e subprodutos das reações em função da temperatura. Os estudos foram realizados em um ambiente apropriado de ultra alto vácuo (UHV) por meio de uma combinação de técnicas experimentais de microscopia de varredura por tunelamento (STM) e espectroscopia de fotoemissão por raios-X (XPS), além de cálculos e simulações complementares por teoria do funcional da densidade (DFT).

Os resultados mostraram que as interações molécula-substrato apresentam diferentes graus de intensidade em cada superfície ($\text{Gr} < \text{Ag} < \text{Cu}$), portanto a dissociação dos átomos halogênios da Cl_4TPP também segue essa hierarquia na reação de acoplamento Ullmann. Em Cu(111), verificamos uma configuração de adsorção distorcida (*inverted structure*) para as porfirinas de base livre devido à interação do tipo covalente com a superfície, o que contribuiu para dificultar a formação de uma rede bidimensional de grande extensão. Já para os casos da Ag(111) e Gr/Ir(111), a fraca interação molécula-substrato favoreceu a difusão e reorganização dos precursores em redes supramoleculares 2D altamente compactas. Os resultados também indicaram que a disponibilidade de adátomos na superfície é um fator importante para controle de fabricação das nanoarquiteturas. Notavelmente, para o caso 2H-TCNPP sobre Cu(111) na presença de Pd, observamos a formação de uma rede bidimensional jamais observada em experimentos similares na literatura.

List of Figures

2.1	Tetrapyrrole macrocycles found in nature	19
2.2	The parent macrocycle of porphyrins	20
2.3	Bottom-up approach technique	22
2.4	STM images of TPP's on strong Cu(111) and weak Ag(111) interacting substrates	24
2.5	STM contrast of free-base and metalated porphine on Cu(111)	25
2.6	Adsorption-induced deformation of Co-TPP on Ag(111) in saddle shape conformation.	26
2.7	TPA+Fe metal-organic frameworks on Cu(100)	28
2.8	Surface-assisted Ullmann coupling	30
2.9	Hierarchical on-surface Ullmann coupling	31
2.10	Dehalogenation reaction and activation energy barriers	32
4.1	One-dimentional square potential well/Lateral resolution	35
4.2	HOMO-LUMO	39
4.3	Photoemission in the single-particle picture/XPS survey from an Al sample	41
4.4	Chemical and surface sensitivity	43
4.5	STM and XPS chambers	47
4.6	STM Aarhus 150 model	48
4.7	SPECS Phoibos 150 HSA	50
4.8	STM image of Cu(111) surface	52
4.9	STM image of Ag(111) surface	53
4.10	STM image of Graphene on Ir(111) surface	53
4.11	STM image of Pd on Cu(111) surface	54
4.12	Cl ₄ TPP and TCNPP	55
5.1	Optimized gas-phase structure for Cl ₄ TPP	58
5.2	Cl ₄ TPP on Cu(111) at submonolayer deposition	59
5.3	Arrhenius analysis for Cl ₄ TPP on Cu(111)	60
5.4	Arrhenius plot for migration and rotation rates	62
5.5	Experimental and theoretical Cl ₂ TPP on Cu(111)	63
5.6	STM simulations of Cl ₄ TPP on Cu(111) with Cu adatoms below Cl atoms	64
5.7	Cl ₄ TPP on Cu(111) side-on interactions	65
5.8	XPS and STM of Cl ₄ TPP on Cu(111) dechlorination	67
5.9	XPS and STM of Cl ₄ TPP on Cu(111) self-metalation	68
5.10	DFT and STM of Cl ₄ TPP head-on interaction.	69
5.11	DFT reaction pathway	70
5.12	Cl ₄ TPP on Ag(111)	74
5.13	Submonolayer and ML coverage of Cl ₄ TPP on Ag(111)	75

5.14	<i>porous</i> and <i>zigzag</i> overlayers	76
5.15	STM image and XPS spectrum for a ML of Cl ₄ TPP on Ag(111)	77
5.16	Optimal adsorption sites for Cl ₄ TPP on Ag(111)	78
5.17	Bridge/Atop-Rotated adsorption sites	79
5.18	Calculated <i>porous</i> overlayer	80
5.19	Calculated <i>zigzag</i> overlayer	81
5.20	Cl ₄ TPP on Ag(111) after 30 minutes annealing at 350 K	82
5.21	Cl 2p XPS measurements after 400 K heat treatment	83
5.22	Thermally treated Cl ₄ TPP adsorbed on Ag(111)	84
5.23	DFT calculation of “dome-like” structure on Ag(111)	85
5.24	Model for controlled deposition of atomic hydrogen in Gr/Ir(111) and bandgap opening calculation in the function of atomic hydrogen concen- tration.	87
5.25	STM and LEED of graphene on Ir(111)	88
5.26	Submonolayer and ML coverage of Cl ₄ TPP on Gr/Ir(111)	89
5.27	HR-XPS spectra for a Cl ₄ TPP ML on Gr/Ir(111)	90
5.28	STM image of Cl ₄ TPP on Gr/Ir(111) after 590 K annealing	92
5.29	ARPES of Cl ₄ TPP on Gr/Ir(111) before and after H ⁺ deposition	93
5.30	STM image of 2H-TCNPP on Cu(111) as grown and after mild annealing .	95
5.31	2H-TCNPP on Cu(111) after Fe adatoms deposition	97
5.32	2H-TCNPP on Pd/Cu(111) deposited at RT	99
5.33	2H-TCNPP on Pd/Cu(111) after annealing to 350 K for 10 minutes	100
5.34	2H-TCNPP on Pd/Cu(111) after annealing at 400 K for 10 minutes	101
5.35	2H-TCNPP on Pd/Cu(111) as function of the annealing time at 400 K for 30 and 60 minutes	102
5.36	Lattice vectors of the periodic 2H-TCNPP porous 2D network	104
5.37	Models for 2H-TCNPP molecules undergoing dehydrogenation	105
A.1	States in potential well (Bardeen approach)	128

List of Abbreviations

<i>h</i> BN	Hexagonal boron nitride
<i>XC</i>	Exchange and correlation functional
2H-TCNPP	2H-tetrakis(<i>p</i> -cyano)-phenylporphyrin
2HP	Porphin
ARPES	Angle-resolved photoemission spectroscopy
Cl ₄ TPP	5,10,15,20-(tetra-4-chlorophenyl)porphyrin
CVD	Chemical vapor deposition
DFT	Density functional theory
GMR	Giant magnetoresistance
GNR	Graphene nanoribbons
Gr	Graphene
HOMO	Highest occupied molecular orbital
HOPG	Highly ordered pyrolytic graphite
IMFP	Inelastic mean free path
IUPAC	International Union of Pure and Applied Chemistry
LDOS	Local density of states
LED	Light-emitting diode
LEED	Low energy electron diffraction
LUMO	Lowest unoccupied molecular orbital
ML	Monolayer
RT	Room temperature
SMOF	Surface metal-organic framework
STM	Scanning tunneling microscopy
STS	Scanning tunneling spectroscopy

TMD	Transition metal dichalcogenides
TPA	Terephthalic acid
TPP	Tetraphenylporphyrin
TSP	Titanium sublimation pump
UHV	Ultra-high vacuum
XPS	X-ray photoemission spectroscopy

List of Publications

I. Moreno-López, J.C., Mowbray, D.J., Pérez Paz, A., De Campos Ferreira, R.C., Dos Santos, A.C., Ayala, P. and De Siervo, A. Roles of Precursor Conformation and Adatoms in Ullmann Coupling: An Inverted Porphyrin on Cu(111). *Chemistry of Materials* **31**, 3009–3017 (2019).

II. Dos Santos*, A.C., De Campos Ferreira*, R.C., Moreno-López, J.C., Barreto, L., Lepper, M., Landers, R., Steinrück, H.-P., Marbach, H. and De Siervo, A. Cyano-Functionalized Porphyrins on Cu(111) from One-Dimensional Wires to Two-Dimensional Molecular Frameworks: On the Role of Co-Deposited Metal Atoms. *Chemistry of Materials* **32**, 2114–2122 (2020). *Co-first authors.

III. De Campos Ferreira*, R.C., Pérez Paz, A., Mowbray, D.J., Roulet, J.-Y., Landers, R. and De Siervo, A. Supramolecular Ordering and Reactions of a Chlorophenyl Porphyrin on Ag(111). *The Journal of Physical Chemistry C* **124**, 14220–14228 (2020).

IV. Chlorophenyl Porphyrin on Graphene: Self-Assembly and Atomic Hydrogen Irradiation. *In Preparation*.

Contents

1	Introduction	14
2	Literature Review	18
2.1	Free-base Porphyrins	18
2.2	Tetraphenylporphyrins on reactive surfaces	21
2.3	Organometallic complexes	26
2.4	On-surface Ullmann coupling	29
3	Objectives	33
4	Experimental Methods	34
4.1	Scanning Tunneling Microscopy (STM)	34
4.1.1	Basic Principles of STM	35
4.1.2	Organic Adsorbates on Metal Surfaces	38
4.2	X-ray Photoelectron Spectroscopy (XPS)	40
4.2.1	Basic Principles of XPS	41
4.2.2	Surface and chemical sensitivity	42
4.3	Experimental setup	45
4.3.1	Background information	45
4.3.2	UHV system used in this thesis	47
4.3.3	Sample preparation	51
5	Results	56
5.1	Introduction	56
5.2	Cl ₄ TPP on Cu(111)	58
5.3	Cl ₄ TPP on Ag(111)	73
5.4	Cl ₄ TPP on Gr/Ir(111)	86
5.5	2H-TCNPP on Cu(111) with co-adsorbed metal atoms	94
	Conclusions and perspective	107
	References	110
A	Bardeen Approach	127
B	Density Functional Theory calculations	131

Chapter 1

Introduction

Together with the advent of nanotechnology and technical advances of precise structural and chemical characterization that allowed the exploration of matter on atomic and molecular scale, a promising new field of science emerges inspired to develop novel nanodevices, resulting in possible direct applications on nanomedicine, nanoelectronics, biomaterials energy, and consumer products. Nowadays, one of the great challenges for the scientific community is the mastery control of advanced synthesis and manipulation techniques at the atomic level. A promising approach that has been showing significant success is the bottom-up synthesis, which consists of building complex supramolecular structures starting from elementary building blocks such as atoms, molecules, and nanoparticles. Those precursors are exposed to reactions in a controlled environment in order to group them in a controlled fashion. In particular, when reactions are confined to a surface, there is a high probability of zero-, one- or two-dimensional materials synthesis.

More recently, the use of organic elementary precursors as building blocks has shown interesting and promising results in the synthesis of supramolecular complexes like self-assembled metal-organic porous networks and long-range ordered polymeric structures, all such materials that have potential application in high-performance electronic devices, gas sensors, organic LED's, biocompatible devices that mimic vital biological processes, self-healing materials, graphene-like materials, templates for catalysts nanoparticles, etc.

The successful realization of this nanoarchitecture involves the correct choice of molecular precursors. The geometry of these nanostructured building blocks will dictate the grouping rules and the structural complexity of the network formed. In general,

rigid flat molecules that show resistance to relatively high temperatures are promising structures. Among them, we may highlight the well-known porphyrin-like molecules, which presents wide structural and chemical diversity and have been explored extensively. These macromolecules have been studied because they are important compounds present in nature and that participate in vital processes to the life of living beings, for instance, in hemoglobin inside the blood of vertebrates, in chlorophyll responsible for photosynthesis, and even in vitamin B12. They have a rigid and reactive macrocycle that can be functionalized by basically any element of the periodic table. In its periphery, there is also the possibility of adapting flexible functional structures that interact in the presence of other precursors besides the reactive surface. When these precursors are sublimated on the reactive template surface, depending on the nature of the interaction, they might be steered to a possible formation of supramolecular self-assembly, metal-organic coordination in a porous network, or coupling reaction forming polymeric complexes. Polymeric networks, if large and highly ordered, present efficient electron transport, high chemical stability, interesting optical properties as well as mechanical strength due to the covalent nature of connections between molecules. This makes 2D porous networks promising candidates for carrying out synthesis of molecular membranes and atomically accurate templates with nanotechnological applications in organic semiconductors, optoelectronic devices, gas sensors, catalysts, just to mention a few.

Among the several processes of on-surface reaction synthesis, the surface-assisted Ullmann coupling is an interesting approach widely studied and reported in the literature. The process consists of using molecular precursors functionalized with halogen atoms in their peripheries so we catalytically split off these elements on the surface, subsequently inducing the precursors to diffusion and regrouping by polymerization. Several successful examples can be found in the literature, with special emphasis on the synthesis of carbon-like materials such as graphene nanoribbons, highly ordered graphene, etc. The reason behind the choice of atoms in group 17 of the periodic table is due to the fact that these elements have relatively low dissociation energy and thus the reaction can be activated in a controlled way by temperature or by the co-deposition of reactive atoms. It is possible to find many complete works exploring molecules functionalized with atoms of Br and I. The absence of studies with Cl encouraged us to initiate this exploration using strategically precursors based on free-base porphyrins: in particular, the 5,10,15,20-(tetra-

4-chlorophenyl) porphyrin (Cl_4TPP) adsorbed on several single-crystal surfaces with different intensity levels of reactivity. Cu(111) as a highly reactive surface, Ag (111) moderately reactive, and Graphene/Ir(111) as weakly reactive. In parallel, we also made use of precursors with carbonitrile termination (2H-tetrakis(*p*-cyano)phenylporphyrin) 2H-TCNPP, which shows highly propensity to perform organometallic coordination with adatoms on reactive surfaces. An organometallic compound is usually an intermediate state of surface-assisted Ullmann coupling, which leads us to consider it an essential topic in our study. Herein, we deposit 2H-TCNPP on Cu (111) with co-adsorbed Fe and Pd atoms, which are highly reactive to induce metal-coordination and polymerization.

In this context, the scientific problem proposed for this thesis is to synthesize and structurally/chemically characterize the supramolecular organic networks and its by-products obtained through the surface-assisted Ullmann coupling method for free-base porphyrins on single-crystal metals. In order to perform an appropriate study, we need facilities for ultra-high vacuum environment (UHV) experiments and proper surface science technical apparatus. The experiments were carried out in the Surface Science Group at the Department of Applied Physics of the Institute of Physics “Gleb Wataghin” (DFA-IFGW), located in the State University of Campinas (UNICAMP). The laboratory was equipped in a way that we were able to perform, mainly, atomic high-resolution scanning tunneling microscopy (STM) for structural determination, and surface-sensitive spectroscopy by X-ray photoemission spectroscopy (XPS) for chemical monitoring the reactions and their by-products. We were also supported by theoreticians collaborators who implemented density functional theory (DFT) calculations and simulations to assist us in the interpretation of experimental data. The computational simulations were carried out in the Imbabura cluster at the Yachay Tech University and made fundamental importance in corroborating our results.

This thesis is organized as following: Chapter 2, a brief review of the literature on porphyrin-like molecules, their influence on different reactive interfaces as well as the relevant intermediate complexes and by-products resulting from the on-surface Ullmann coupling reaction. In Chapter 3, a brief introduction to the techniques and methodology used. In sequence, Chapter 4 presents the results and analytic discussion for Cl_4TPP on Cu(111), Ag(111), and Gr/Ir(111); and the 2H-TCNPP on Cu(111) with co-adsorbed

metal atoms. Finally, Chapter 5 brings some concluding remarks as well as perspectives for future works.

Chapter 2

Literature Review

2.1 Free-base Porphyrins

Porphyrins are fundamental molecular structures and part of a larger group of cofactors denominated tetrapyrrole macrocycles. The chemical structure of these compounds serves as essential structural blocks in the formation of several proteins indispensable to life in a way that their performance in biological processes can vary from oxygen transport to electron transfer and oxidation reactions in the photosynthesis [1]. Figure 2.1 illustrates a set of cofactors among the most important found in nature that present a wide variety of functional properties related to vital biological processes. Among them, we may highlight chlorin, which is a fundamental element for the formation of chlorophyll a (Chl a), actuator in photosynthesis. This organic complex is responsible for the light absorption through electronic excitation of Mg(II) ion, actively participating in the energy conversion process of plants and algae. Another important cofactor is corrin, which is coordinated with Co ion and forms the chemical basis present in vitamin B12, also known as cobalamin, an essential organic compound for the growth of many microorganisms. In human metabolism, it is vitally important for maintaining the nervous system function and auxiliary in the production of red blood cells. We can also mention, in particular, the porphyrin, which forms the heme B when functionalized with a Fe(II) ion in its core nucleus. This cofactor is an essential part of the hemoglobin, responsible for the oxygen transport to the cells through the blood of vertebrates, invertebrates, and exceptionally in some microorganisms.

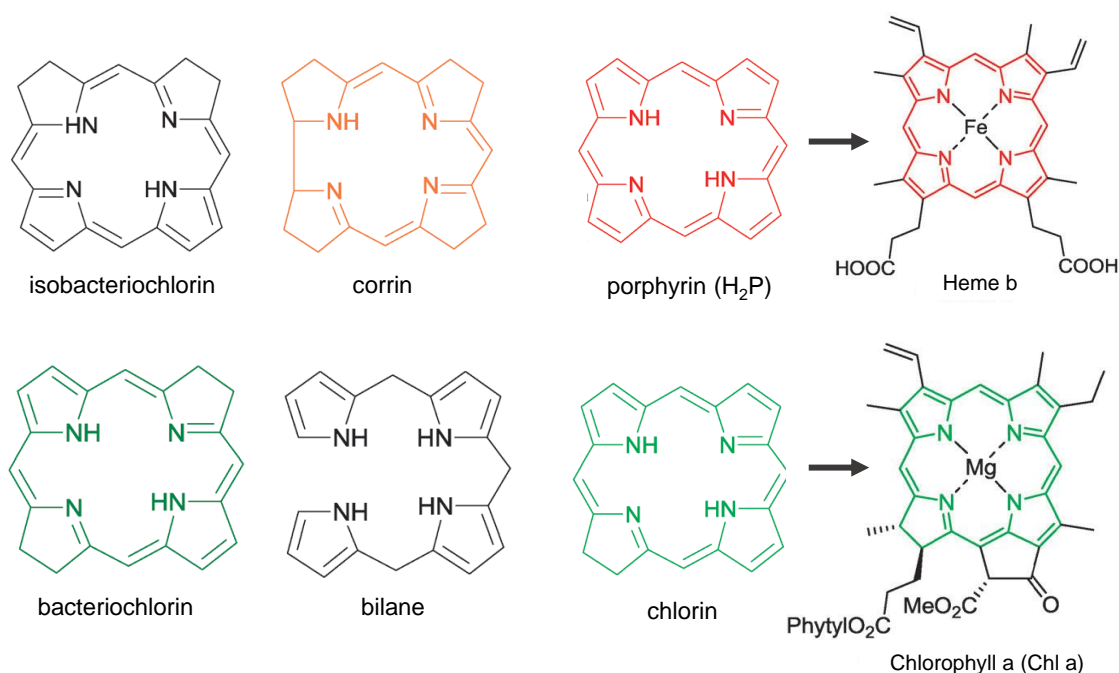


Figure 2.1: Illustrative scheme of the main tetrapyrrole macrocycles found in nature. Special emphasis on chlorin, an essential compound in the formation of chlorophyll a (Chl a), and on porphyrin (H₂P), essential in the formation of Heme b. Adapted from Reference [1].

Structurally, the parent macrocycle of all porphyrins is porphin (2HP), as illustrated in Figure 2.2(a). The tetrapyrrole follows the numbering scheme according to the current International Union of Pure and Applied Chemistry (IUPAC) nomenclature. It consists of four pyrrole moieties connected by methine groups ($=\text{CH}-$) in α -positions, while the *meso*- and β -positions are functional branches that can be adapted by peripheral substituents. The core has two pyrrolic hydrogen atoms ($-\text{NH}-$) and a reactive iminic nitrogen ($=\text{N}-$) in such a way that the macrocycle is subject to a constant double proton exchange mechanism, which characterizes it as a tautomer compound [2–5]. Porphins that have peripheral substituents at the 5, 10, 15 or 20 positions are named *meso*-substituted porphyrins and are frequently explored in surface science studies. The example showed in Figure 2.2(b) represents one of the most basic model of a porphyrin-based molecule: four phenyl groups in the *meso*- positions forming the tetraphenylporphyrin (TPP) [6, 7]. In their most fundamental structural form at equilibrium, the phenyl groups are not coplanar with the macrocycle due to the intramolecular steric repulsion between the hydrogen atoms located in the *ortho*-positions and the macrocycle hydrogens, which brings interesting flexibility that helps in eventual intermolecular bonds. It is worth mentioning

that the presence of a reactive core, often functionalized with metals (metal complexes) may serve as a catalyst to reactions, or assist in the capture and storage of gases, for example.

Porphyrins that may not have a functionalized core are called free-base porphyrins and are susceptible to incorporating free chemical elements available in the environment. In general, the core is able to bind with practically all elements that have stable isotopes, except nitrogen, halogens and rare gases [8]. For the specific case of 3d transition metals, the ionic radius perfectly fits in the macrocycle and between the nitrogen atoms, so that the formed metal complex has a flat structure. For larger metal ions such as Sn(II), Pb(II), Ce(II), or some early transition metals (Mo, Nb and Zr), the atoms are positioned outside the porphyrin plane and the result is a complex with a “shuttlecock” shape [9].

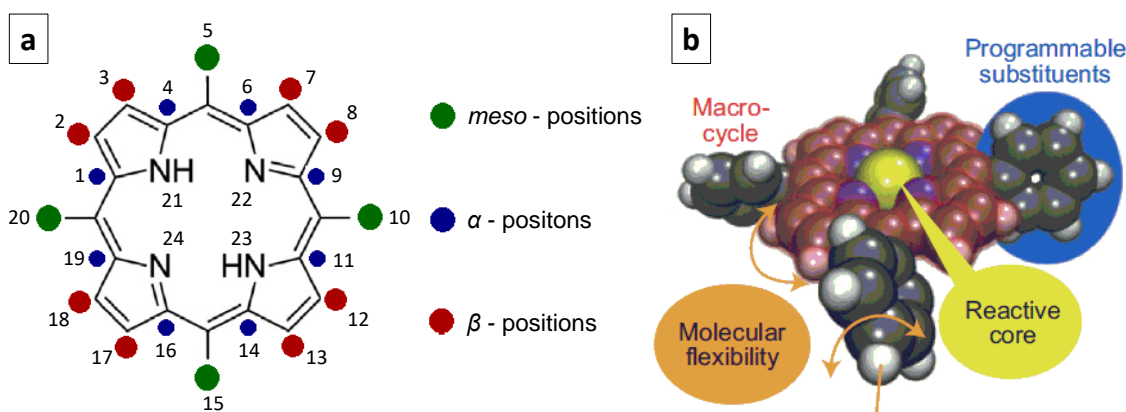


Figure 2.2: (a) The parent macrocycle of porphyrins: 2HP. The numbering scheme is according to IUPAC nomenclature. (b) Space-filling model scheme of *meso*-substituted porphyrin with four phenyl groups forming the 5, 10, 15, 20 - Tetraphenylporphyrin (TPP). Illustration adapted from reference [10].

One of the main interests of the scientific community studying such organic structures and derivatives is the possibility of exploring the intrinsic chemical properties of these elements in the synthesis of biocompatible compounds so that we could use them in industrial applications such as pigments and oxidation catalysis, or even explore their photosensitivity in photodynamic cancer therapy, artificial photosynthesis, gas sensors, optics and nanomaterials [10]. More specifically in the context of surface chemistry, the researches focus on the study of chemical coordination at the solid/vacuum interfaces and

on the chemical-physical influence of the adsorbed elements, as well as the on-surface reactions and their by-products.

In addition to reactivity with the substrate, the macrocycle rigid structure of porphyrin-like precursors combined with its square-planar geometry favors the formation of one- or two-dimensional coordination networks [11, 12]. In this context, the idea is to be able to control the interactions and reactions between molecules and interfaces in order to group them into ordered supramolecular networks that present distinct properties and with potential applications on organic solar cells [13–15], organic light-emitting diodes (LED’s) [16], high-performance organic-electronics [17, 18], optoelectronics [19], biocompatible devices [20–22], graphene and graphene nanoribbon (GNR) synthesis [23–28], molecular porous network templates for catalytic nanoparticles [29–33], just to mention a few.

2.2 Tetraphenylporphyrins on reactive surfaces

Taking advantage of the compact, rigid and simple structure of the porphyrin-based molecules, as well as the great coordinating capacity of these species, the search for the development of ultra-high density and well-defined functional nanostructures has become a major attraction for the nanotechnology field, especially with the emergence of more accurate and advanced techniques for investigation of the microscopic world. However, one of the great challenges nowadays is the mastery of atomically precise manipulation and synthesis techniques of these nanomaterials.

One of the most effective and widely used approaches for this nanoarchitecture is the so-called bottom-up technique [34, 35], which consists of starting with small elementary molecular precursors (building blocks), and then facilitate the self-assembly into large structured blocks (see Figure 2.3). When the reaction is confined to a surface, the building blocks might organize into one-dimensional (1D) or two-dimensional (2D) frameworks. The templates to support precursors are, in general, single-crystal metals and the assembly reactions are either activated thermally or by co-adsorption of reactive elements like metal atoms or nanoparticles. Moreover, the self-assembly can also be interesting and very promising on 2D supported materials, such as graphene (Gr), hexagonal boron nitride (*h*BN) and transition metal dichalcogenides (TMD’s) [29, 36].

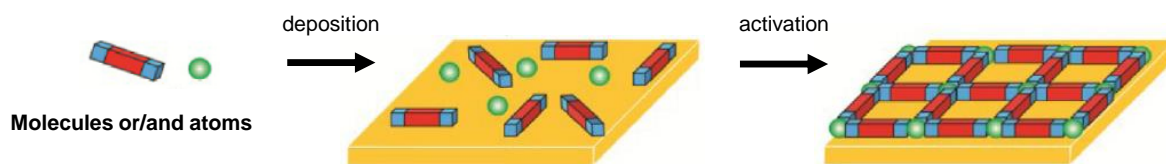


Figure 2.3: Illustrative representation of bottom-up approach technique for on-surface self-assembly. Adapted from reference [37]

Essentially, the formation of well-ordered molecular superstructures is based on the interplay between molecule-molecule (intermolecular) and molecule-substrate interactions. For example, if there is a surface that weakly interacts with precursors, the molecules typically have high surface mobility and group together in a compact way. On the other hand, if the adsorbed molecules interact strongly with the substrate, the lack of mobility or even molecular repulsion can be a problem for the self-assembly. In any case, the molecule-substrate interaction can also dictate the growth directionality of the supramolecular network in an epitaxial way, which is desirable. The great challenge, therefore, is to find a balance in the control of these interactions in order to develop a clean and effective technique path for the synthesis of these low-dimensional functional materials.

In general, the intermolecular interactions can be divided among non-directional weak forces, such as van der Waals (vdW); slightly strong and directional (e.g. hydrogen, metal coordination, dipolar, π - π and T-type stacking); or strong covalent bonds. The vdW bonds are generally predominant when the molecule-substrate interaction is significantly weak. In these cases, the result is closed-pack assemblies where the geometry of the precursors dictates the symmetry of the formed network [38]. On the other hand, strong interactions lead to more varied geometric transformations and open assembling motifs [29, 39, 40].

As mentioned before, in this present work we are especially interested in the study of self-assembly of non-metallated TPP's and derivatives on both weak and strong interacting substrates, as well as the on-surface resulting reactions (induced or not) and their by-products. TPP's on weakly interacting substrates tend to group together forming near-square lattice networks. In the literature, usually Ag, Au and even HOPG surfaces present this characteristic [41]. The Figure 2.4(a) illustrates the assembly of

TPP molecules due to intermolecular interaction on Ag(111) [42]. The squarish network pattern is present for low and high surface coverages, which suggests an attractive non-covalent interaction among adsorbates. On the other hand, a more reactive substrate, like Cu(111), the higher bond intensity might promote peculiar adsorption features as shown in Figure 2.4(b)-(c). Accordingly, at low coverage, the molecules are individually coupled to the surface and aligned to the crystallographic directions $\langle 1\bar{1}0 \rangle$, showing low diffusion mobility. Lepper *et al.* [43] characterized this peculiar adsorption configuration in detail so that the molecules opposing pyrrole rings (NC_4) undergo a drastic rotation and the iminic nitrogens ($=\text{N}-$) point towards the bridge positions on the Cu(111) surface (see details in the inset of Figure 2.4(b)). This distorted adsorption geometry was named “inverted” structure and recently validated by Ryan *et al.* [44]. At higher submonolayer coverages (see Figure 2.4(c)), the precursors interestingly show an intermolecular repulsion among them due to a complex molecule-substrate interaction that culminates in a negative charge surrounding the TPP/Cu interface [45]. When increasing coverage close or slightly higher than a monolayer (ML), there is formation of a checkboard-like motif, as illustrated in Figure 2.4(d). This configuration was observed by Rojas *et al.* [45] and later proposed by Stark *et al.* [46], which consist of a rectangular pseudo-second layer stabilized by π - π stacking interactions between the phenyl rings, as shown in the inset of Figure 2.4(d). Moreover, the molecules in these pseudo-second layers also interact forming a T-type stacking with the molecules at the first layer configuring a pseudo-bilayer complex. These types of stacking were also reported for ML complexes and are recurrent in self-assembled systems [47, 48].

Among all the interactions covered so far, none of them are really strong and stable as the covalent bond. In many cases, to ensure the usefulness of two-dimensional networks in technological applications, it is mandatory to create stronger covalent connections between the precursors. Thus, the most adopted strategy is the well-known on-surface polymerization. Among these techniques, we can mention the Sonogashira coupling, which consists of the formation of a C–C bond between a terminal alkyne and an aryl or vinyl halide [49]; polymerization via alkanes dehydrogenation [50], Ullmann coupling [51], etc. Over the past ten years, one of the most explored polymerization mechanism is the surface-assisted Ullmann coupling of aromatic molecules with halogenic

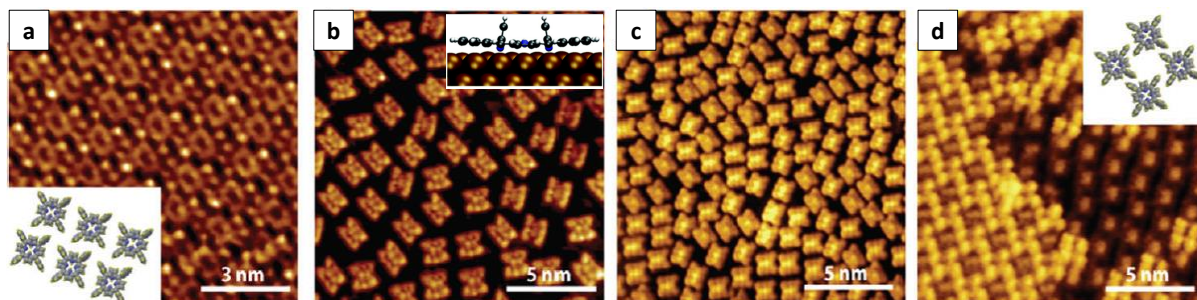


Figure 2.4: STM images of TPP on Ag(111) (a) and Cu(111) (b-d). (a) Predominant intermolecular interactions forming a coldest-pack assembly at 0.6 ML molecular coverage. (b) Isolated molecules strongly bonded to the surface at 0.6 ML coverage. The model of the distorted adsorption configuration named “inverted” structure can be seen at the inset of the image. (c) 0.7 ML coverage and molecules reveal a repulsive behavior due to a negative charge induction between molecules and Cu substrate. (d) At 1.2 ML shows a pseudo-second layer forming T-type and π - π stacking interactions. Tunneling parameters: $U = 0.8$ V, $I = 0.4$ nA. Illustration adapted from reference [45].

terminating atoms [52]. This reaction will be one of the main focus of this work and details can be found in section 2.4.

Regarding the molecule-substrate interactions, we must be aware that the direct contact of the surface with the molecular precursors can significantly affect the photochemical, catalytic, transport and magnetic properties of the system. In other words, the electronic states of the supporting substrate induce changes in the molecular orbital electronic occupation. Studies show that the substrate-adsorbate charge transfer may be associated with a change in the oxidation state of the metal complex [53–56]. The impact of this change can even be distinguished in STM images. For example, images recorded at low bias revealed a characteristic protrusion in the center of Co-TPP and Fe-TPP, which is related to the metal center [10] and does not occur for free-base TPP’s due to an absence of metal, see Figure 2.5.

Another observed phenomenon resulting from the molecule-substrate interaction is the Kondo effect, which originates from the interaction of the porphyrin’s spin-active metal center with the substrate and that affects the magnetic properties of the sample. Kondo features were studied for Co-TBrPP on Cu(111)[57], Mn-TPPCl on Co [58], Fe-TPP on Ni and Co films [59], just to mention a few. The development of new spintronic organic materials is quite promising in applications for the data storage device industry like giant magnetoresistance (GMR) read-heads and magnetic random access memory [60].

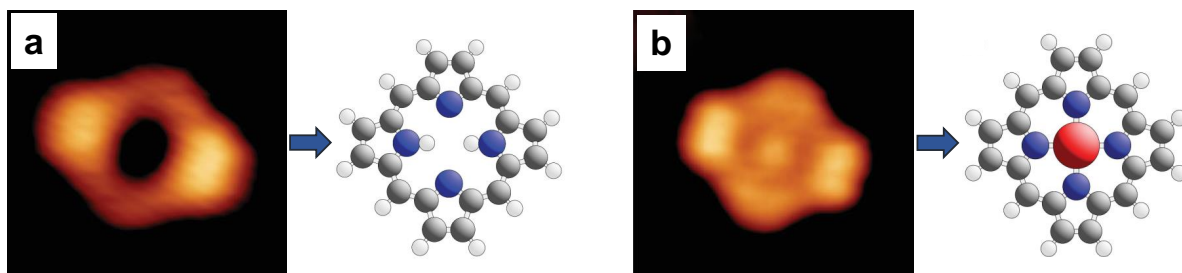


Figure 2.5: STM images of free-base porphines on Cu(111) before (a) and after (b) metalation upon 423 K annealing. In contrast, the molecules show a central bright protrusion after metalation. Adapted from reference [55].

Furthermore, the structural arrangement of the metal centers or ligands in a well-defined pattern (metal-organic coordination) modulated by different adsorption configurations of each molecular species might drastically affect the catalytic property of the material (see section 2.3 for more details). Thiol-functionalized cobalt porphyrins on Au(111) demonstrated significant catalytic activity [61], as well as Mn-porphyrins on Au(111) and on solid-liquid interfaces [62, 63]. An interesting study showed high-catalytic activity of hermin and Fe-porphyrin derivatives upon confinement on graphene support [64]. In addition, Fe-phthalocyanine adsorbed on Ag(110) presented interesting chemical properties and proved to be a possible catalytic agent in fuel cell materials [65]. Thus, establishing different routes to new metal-organic porous networks are very interesting for the development of novel organic-based catalysts for the energy industry.

Porphyrins, in particular, by structurally allowing the attachment of flexible substituents, are able to interact non-uniformly with the surface and directly affect the functionality of the molecule or the formed supramolecular network. For example, the spatially resolved STS study of Co-TPP on Ag(111) by Auwärter *et al.* [56] provided information on occupied and unoccupied electronic states revealing the influence of non-planar geometry on molecular orbitals. These deformations induced in adsorption are an important segment on the study of self-assembly architectures of porphyrin-like molecules, as it significantly affects intermolecular interactions. Studies using high-resolution STM have proven to be very useful in determining the orientation of meso-substituted porphyrins, both in relation to the surface plane of the substrate and to the molecular core (ρ and θ , respectively) [66–68]. Detailed determination of adsorption geometry is particularly powerful if combined with the study of high-resolution STM and complementary DFT

calculations [69, 70]. For instance, free-base and metalized meso-substituted porphyrins adsorbed on single-crystal metals present, for the most cases, the well-known “saddle-shape” conformation. This adsorption configuration is shown in Figure 2.6 for Co-TPP on Ag(111) and it’s in special contrast with the “inverted” structure mentioned before.

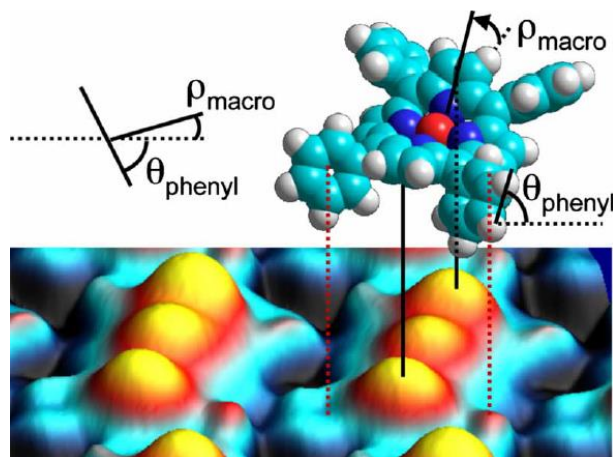


Figure 2.6: Adsorption-induced deformation of Co-TPP on Ag(111) in “saddle-shape” conformation. The scheme shows the non-planar macrocycle with angle $\rho_{macro} = 30^\circ$ related to the Ag(111) surface and rotated phenyl groups $\theta_{phenyl} = 45^\circ$ related to the macrocycle plane. The high-resolution STM image at the bottom of the figure indicates the measured contrasts observed on microscopic scanning. Illustration adapted from reference [56].

2.3 Organometallic complexes

The study of coordinated metal-organic complexes is a branch of Physical-Chemistry that has gained great prominence in the last 20 years [37]. The field involves extensive study of 3D supramolecular frameworks in solution-based chemistry. More recently, the exploration of molecule’s chemical coordination on solid surfaces also became attractive for bringing a complex and vast number of organometallic structures that can be synthesized and explored. Surface metal-organic frameworks (SMOF’s) are structures composed of metal cores (or cations) connected by organic linkers so that the nature of the connection between them is established by the so-called metal-ligand coordination interaction [37]. The established bonds generally involve the charge transfer from metal centers to functional groups of the organic ligand. This type of directional bonds are especially stable at relatively higher temperatures above room temperature (RT) and,

in many cases, reversible because of its intermediate strength, which can eventually be interesting in the development of self-healing materials [71, 72].

A very interesting model system that helps us understand coordination networks at surfaces is the case of terephthalic acid (TPA) with Fe centers on Cu(100). The study performed by Tait *et al.* [73] revealed the existence of several achievable porosities of TPA + Fe phases, which are related to the relative concentrations between metal and organic ligands. Herein, when depositing the molecules initially at RT, was noticed the formation of a simple supramolecular network established by intermolecular hydrogen bond interactions. However, after thermal treatment at 400 K, the complete deprotonation of the TPA carboxylate groups along with controlled Fe deposition enhanced the ability to establish such metal-ligand interactions. Figure 2.7 shows the possible metal-organic well-ordered networks and the respective STM images for different Fe/TPA ratios. At small Fe coverages in figure 2.7(a-b), for each TPA molecule there is only one coordinated oxygen per metal atom forming a $\text{Fe}(\text{TPA})_4$ complex, while at higher coverages, there is a variety of possible coordinations resulting in more complex porous networks, as shown in figure 2.7(c-f). This example enlightens us on the importance of the availability of metal atoms diffusing over the surface to establish connections, whether they are co-adsorbed during molecule sublimation or stimulated from the substrate itself by thermal activation (such as adatoms).

Other examples that are particularly important for us in this thesis, are coordinated networks facilitated by molecular ligands with CN termination groups, also known as carbonitrile organic compounds. These are excellent electron donor and promising intermediate on the assembly of metal-organic precursors since the charge distribution of the CN groups induces the formation of an intrinsic dipole that could be useful either by promoting intermolecular interactions or by facilitating the coupling with free adatoms on the surface [74–79]. The relatively high reactivity of these terminations can be an important tool on availability control of adatoms for the synthesis of metal-organic complexes even at low temperatures. In an interesting work, Lepper *et al.* [80] reported a study of self-metalation control of free-base porphyrins molecules on Cu(111) promoted by the gradual addition of cyano groups at the peripheral phenyl branches. The results showed that the presence of the functional groups coordinated with metals ($\text{CN} \cdot \cdot \cdot \text{M}$) act as “shields” and hinder the diffusion of Cu adatoms on the surface, preventing the

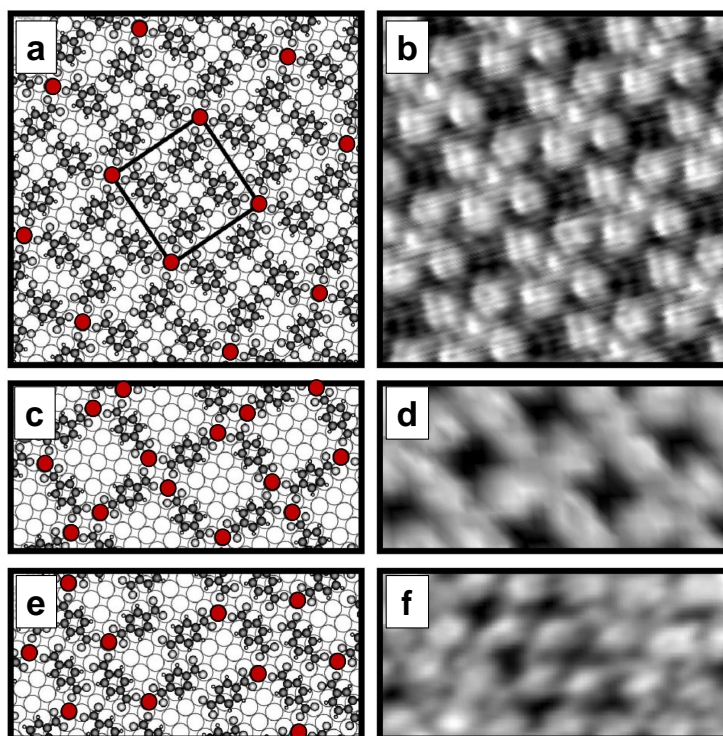


Figure 2.7: TPA+Fe metal-organic frameworks on Cu(100) and respective STM images (scan width 5 nm). The red dots represent the Fe atoms coordinated with terminal carboxy groups. (a-b) 6×6 Fe(TPA)₄ coordination phase at lower Fe coverage after 400 K annealing. (c-f) Multiple coordination structures at higher coverages (high Fe/TPA ratio). Adapted from reference [73].

self-metalation reactions. It means that when the molecules have all their terminations functionalized by CN, there is a great potential to establish side connections and form an organometallic network, besides the fact that the moderate mobility of the free-base precursors also enables a more accurate thermal diffusion control for the synthesis process.

Regarding the on-surface reactions that might occur, especially the Ullmann coupling process (which will be discussed in more details in the next section), the presence of organometallic complexes as intermediate states is extremely common and should be widely understood and taken into account if one want to precisely control the synthesis of functional molecular nanoarchitectures [81].

2.4 On-surface Ullmann coupling

On-surface synthesis in solid/vacuum interfaces is a technique that has been gaining wide attention in the last decade and has been used to study methods for promoting the polymerization of molecular precursors in order to efficiently build covalent organic frameworks with atomic precision. The strong nature of the covalent bond allows the development of highly stable polymeric complexes, preventing any defragmentation process on the surface that may be facilitated when exposed to a chemically or physically hostile environment. So far, it is worth highlighting the success and efficiency of the technique on the synthesis of graphene-related nanostructures such as porous graphene [82], GNR [26, 83, 84], and nanographenes [85]. One of the cleanest and most robust reactions that has been conducted on solid surfaces is the Ullmann coupling [51], which is a covalent aryl-aryl bond formation between aryl halides induced on coinage metal surfaces [52, 86]. The chemical process is not fully explained and remains a mystery since its discovery, but there is a generally accepted consensus that a metal, which may be a surface adatom or a lattice atom, catalytically activate the dehalogenation of the molecular precursor, that might diffuse on surface until another precursor is found to be coupled by C–C covalent bond.

The reaction mechanism is both molecule and substrate-dependent and the necessary conditions for the reaction activation vary in each case. Generally, the molecular building blocks consist of halogen functionalized side groups (aryl halides) and the cleavage of these elements (dehalogenation) are achieved directly upon deposition on the surface at RT or by thermal activation. This is because the bonds of the carbon-halogen groups (C–X) have low dissociation energy at surface contact. After dehalogenation, the next reaction step is diffusion followed by C–C coupling. According to previous studies, the coupling reaction can take place through two distinct mechanisms: 1) in the absence or 2) in the presence of organometallic intermediates [87–89]. The figure 2.8 shows both paths in a simple picture.

For instance, the STM investigation of Br₄TPP on Au(111) [90] identified the formation of dimer polymeric chains, nanowires, and even 2D assemblies without the formation of organometallic intermediates, that is a typical process conducted by mechanism 1. However, the formation of organometallic complexes during the process of on-surface C–C coupling is rather common. In mechanism 2, when surface adatoms are captured by

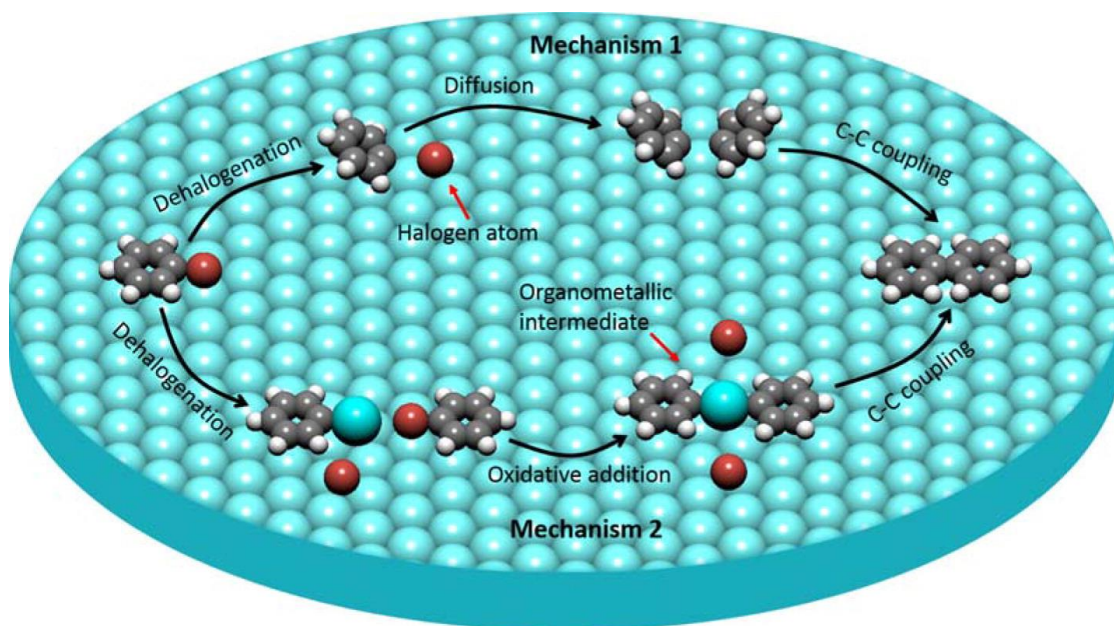


Figure 2.8: Simple picture of surface-assisted Ullmann coupling guided by two different mechanisms. Mechanism 1: dehalogenation followed by direct C–C covalent coupling. Mechanism 2: covalent coupling intermediated by organometallic C–C compound. Gray, white, red, and cyan spheres represent carbon, hydrogen, halogen, and metal atoms, respectively. Adapted from reference [87].

aryl halides groups before dehalogenation, a weak $\text{C-X} \cdots \text{M}$ coordination is previously formed. Then upon intermediary annealing, the metal atoms are incorporated into the C–X bonds promoting the dehalogenation and further organometallic C–M bond. Now, this new complex might diffuse to engage in more structured networks by C–M–C bonds. Finally, in a subsequent annealing step, the metal is released and the organometallic bond is converted into covalent C–C bond.

Figure 2.9 briefly illustrates the steps previously described. In this study performed by Eichhorn *et al.* [91], by the use of a hybrid functionalized molecule 1,3-bis-(*p*-bromophenyl)-5-(*p*-iodophenyl)benzene (BIB) (marked in red) on Au(111), a 2D porous covalent network was synthesized through hierarchical polymerization. This was possible because iodine was selectively split off immediately after RT deposition, whereas bromine remained stably bonded to the precursor so that the BIB molecules coupled together forming dimer self-assembly of 3,3'',5,5''-tetra(*p*-bromophenyl)-1,1':4',1'':4'',1''':4'''-quaterphenyl (TBQ) (marked in green). Finally after annealing that the recombination was activated after debromination resulting in the polymeric framework.

The hierarchical polymerization promoted by selective dehalogenation brings great motivation to more accurate techniques of atomic manipulation. Thus, several

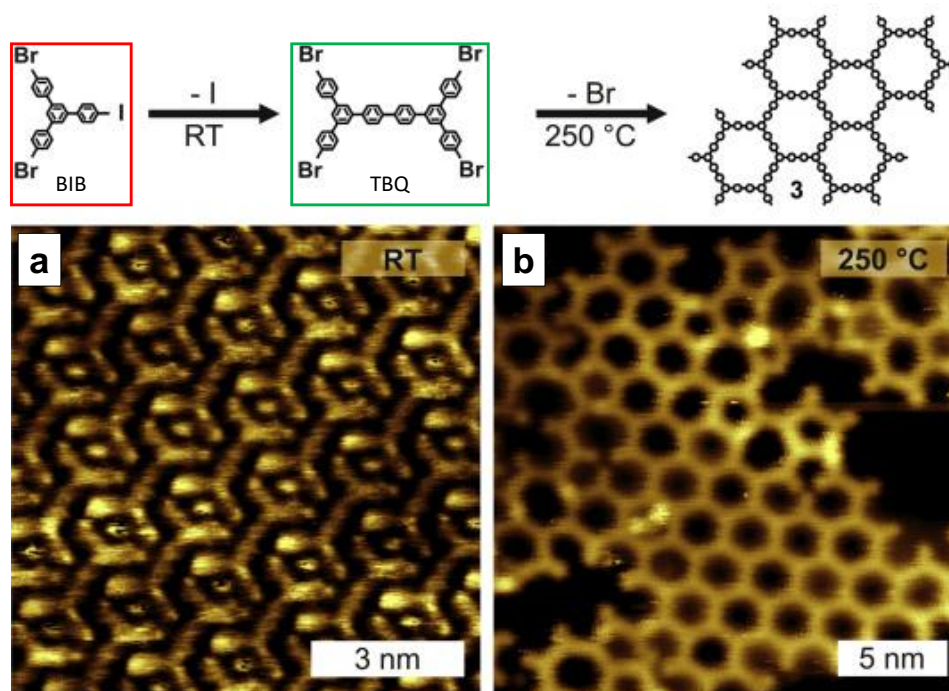


Figure 2.9: Hierarchical on-surface Ullmann coupling of BIB on Au(111). The reaction path to polymerization is illustrated at the top of the image. (a) After RT deposition, deiodination leads to dimmer self-assembly of TBQ. (b) Annealing to 250 Celsius activates the debromination and reorganization of a covalent organic framework. Adapted from reference [91] and [92].

theoretical simulation studies emerged to explain the reaction phenomenon in detail for different molecular precursors and substrates. In a very complete work, Bjork *et al.* [93] computationally study the reaction mechanism of dehalogenation, recombination and diffusion of small halogenated phenyl groups (Br and I) on Cu(111), Ag(111) and Au(111). It was found that the metal surfaces significantly reduces the dehalogenation activation energy, with the largest barrier for Au(111) and the smallest one for Cu(111). In addition, the dissociation barrier for I is smaller than Br, as shown in diagram of figure 2.10(b). Figure 2.10(a) summarize the process for bromobenzene on Au(111). Herein, the split-off activation barrier is relatively low, allowing the direct dehalogenation without organometallic intermediate states, suggesting that for this specific case, the C–C bond is steered by mechanism 1 (see Figure 2.8). Furthermore, the detached Br atom is physisorbed on surface being free to diffuse or desorb.

In principle, the informations above provide us an ideal infrastructure to successfully conduct the synthesis of functional covalent frameworks: from self-assembly and reversible organometallic intermediates to the final polymerization process. However, until now, the synthesis of large-range ordered networks remains a challenge for the

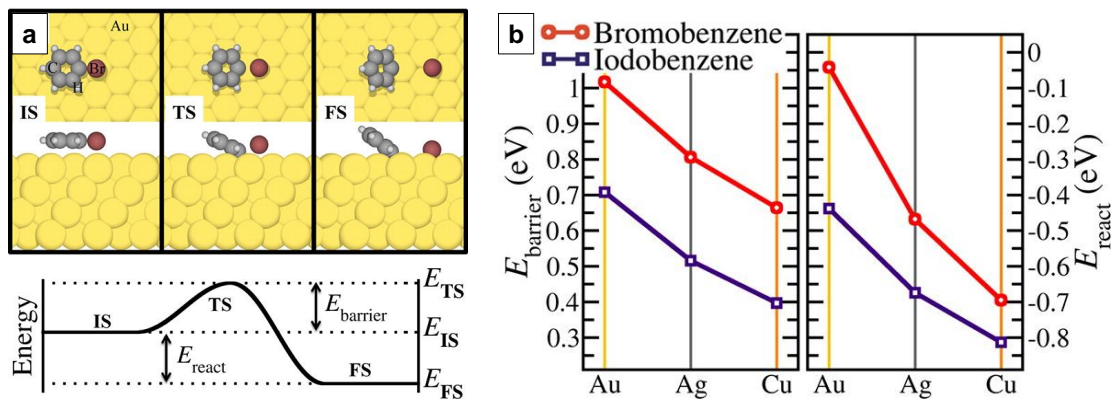


Figure 2.10: (a) Simple picture of a simulated dehalogenation process of bromobenzene on Au(111) and the respective definitions of the energy barrier (E_{barrier}) and reaction energy (E_{react}) of the process, including the initial state (IS), transition state (TS), and final state (FS). (b) E_{barrier} and E_{react} for the process described in (a) for bromobenzene and iodobenzene on different (111) metals. Adapted from reference [93].

experimentalists. Usually, most of the two-dimensional networks obtained are typically characterized by small branched domains and with structural heterogeneity [87]. In addition, halogenated atoms released during on-surface reactions may aggregate into islands, preventing surface diffusion and hinders a proper organization of the precursors.

In this context, several experimental conditions has been proposed to improve the long-range order of the reaction final product, including hierarchical control of reactions at different temperatures, promoting increased availability of adatoms on the surface either by thermal activation or by co-deposition during precursor sublimation, etc. Also, the lack of information on chlorine aryl halides as molecular precursors is an additional motivation to explore such elementary building blocks on different reactive substrates, breaking through new routes for on-surface polymerization to long-ranged frameworks.

Chapter 3

Objectives

This work, inspired by the activation of the Ullmann coupling reaction on different surfaces, proposes to study the products and by-products of free-base porphyrin molecules as building blocks on a bottom-up approach for on-surface synthesis of low-dimensional nanostructures. From two types of molecular precursors: the 5,10,15,20-(tetra-4-chlorophenyl)porphyrin (Cl_4TPP) and the 5,10,15,20-(tetra-4-cyanophenyl) porphyrin (2H-TCNPP), we will monitor the species adsorption configuration, their mobility across different surfaces, as well as chemical and structural changes as a function of temperature.

The well-defined substrate surfaces were chosen with different degrees of reactivity in order to offer different levels of interaction intensity with the molecular precursors ($\text{Cu}(111) > \text{Ag}(111) > \text{Gr}/\text{Ir}(111)$), thus influencing the activation barrier of all reactions, in addition to eventually modifying the adsorption geometry and mobility of the adsorbates. Not less important, it is from the availability of surface adatoms that the formation of organometallic intermediates in the Ullmann reaction is stimulated. Thus, we chose to promote an increase in the concentration of these elements on the surface from the thermal stimulus or by co-deposition by means of conventional evaporators.

The study, for the most part, combines experimental XPS and STM techniques, which are especially complementary and surface sensitive, in addition to DFT calculations and STM simulations that provided extremely important support and corroborated the research in many aspects.

Chapter 4

Experimental Methods

4.1 Scanning Tunneling Microscopy (STM)

Since its invention in the early 1980s, by Rohrer and Binnig [94], the scanning tunneling microscope (STM) has been playing a very important role in the field of nanoscience and nanotechnology. It is an instrument in which the invention was inspired by the quantum tunneling effect, and basically consists on the approximation of two electrodes (tip and sample) with a conveniently applied voltage in order to promote an electric current through the gap between them. By measuring the electron flux, the tip is able to scan the sample surface extracting the topographic and electronic information, i.e. the local density of states (LDOS) [95]. The remarkable resolution achieved by this technique is capable to generate atomic resolved real-space maps of a sample region [96].

In addition to the simple scan of the surface topography, the technique has evolved considerably over the past 30 years in the most diverse areas offering large possibilities on the spectroscopic investigations of elements [97], low-temperature STM for the local density of states characterization [98], vibrational [99], magnetic [100, 101], optical [102] properties, and even on the very precise molecular/atomic manipulation of objects for building nanoarchitecture [103].

4.1.1 Basic Principles of STM

The elementary concept of quantum tunneling can be understood in a simple way by the behavior of a free particle under the effect of a one-dimensional potential barrier $U(z)$ [95]. The solutions of the time-independent Schrödinger equation,

$$-\frac{\hbar^2}{2m} \frac{d^2\psi(z)}{dz^2} + U(z)\psi(z) = E\psi(z) \quad (4.1)$$

are given by wave-function representations $\psi(z)$, where $\hbar \equiv h/2\pi$ is the reduced Planck constant, m the mass of the particle and E its energy. Figure 4.1(a) illustrates the classical case of a square potential barrier; on the left the sample and on the right the tip. For a situation where $U > E$, the wave functions in each region, sample, barrier and tip are, respectively:

$$\psi^S = e^{ikz} + Ae^{-ikz} \quad (4.2)$$

$$\psi^B = Be^{-\gamma z} + Ce^{\gamma z} \quad (4.3)$$

$$\psi^T = De^{ikz} \quad (4.4)$$

where $k = \frac{\sqrt{2mE}}{\hbar}$ and $\gamma = \frac{\sqrt{2m(U-E)}}{\hbar}$.

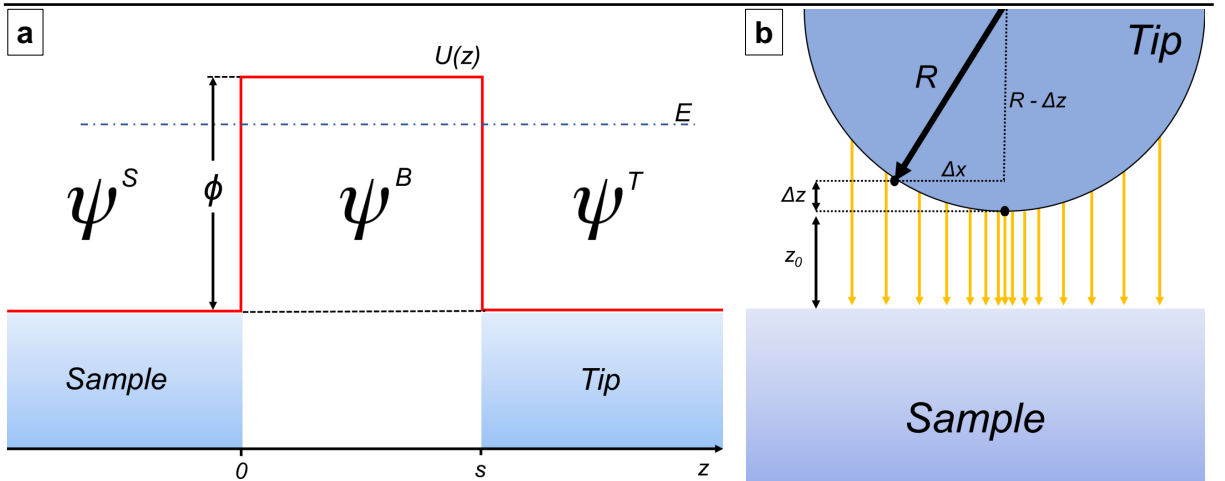


Figure 4.1: (a) A simple schematic picture representing the one-dimensional square potential well for tip-sample contact. See details in the text. (b) Estimation of the lateral resolution (Δx) considering the estimated dimensions of the tip radius of the microscope (R). The current flow is higher in the region close to the sample.

The coefficients A , B , C and D are obtained by the boundary conditions at the edges of the potential barrier. The probability current density given by

$$j = -\frac{\hbar}{2m} \left[\psi^* \frac{d\psi}{dz} + \psi \frac{d\psi^*}{dz} \right] \quad (4.5)$$

allowing us to define the transmission coefficient T between the transmitted ψ^T and the incident ψ^S wave,

$$T = \frac{j^T}{j^S} = |D|^2 = \frac{1}{1 + \frac{(k^2 + \gamma^2)}{4k^2 + \gamma^2} \sinh^2(\gamma s)} \quad (4.6)$$

which simplifies to the limit $\gamma s \gg 1$ (wide barrier, low energy) to

$$T \sim \frac{16\gamma^2 k^2}{(k^2 + \gamma^2)^2} e^{-2\gamma s} \quad (4.7)$$

Through this simple model, we can infer that the tunnel current is exponentially dependent on the tip-sample distance for a given voltage applied between the electrodes. The expression $\gamma = \frac{\sqrt{2m(U-E)}}{\hbar}$ is interpreted taking the definition $U - E \equiv \phi_S = \phi_T = \phi$ as the energy needed to raise the electron from the Fermi level (bulk) to the vacuum level, well-known as work function. For typical values of metals ($\phi \sim 5\text{eV}$), we have $\gamma \sim 1\text{\AA}^{-1}$. This means that the current decays by one order of magnitude per 1\AA .

Another important and significant feature on obtaining atomic resolution in an STM experiment is the very high lateral resolution. A simple example that helps us understand the phenomenon is illustrated in Figure 4.1(b), which indicates in a geometrically simple way the probe of the experimental apparatus. From it, we are able to estimate that the distance from the sample tip can vary by the relation

$$\Delta z \sim \frac{\Delta x^2}{2R} \quad (4.8)$$

Therefore, assuming each point on the tip surface the current density flows perpendicularly in the one-dimensional case, we have $T \sim I$, so the current distribution is

$$I(\Delta x) \sim e^{-2\gamma \frac{\Delta x^2}{2R}} \quad (4.9)$$

Taking typical values of $\gamma \sim 1\text{\AA}^{-1}$, $R \sim 10\text{\AA}$ and $\Delta x \sim 4.5\text{\AA}$ the tunnel current drops by a factor $\sim e^{-2}$, which corresponds to approximately 90%. Thus, the diameter

that effectively flows electrical current is estimated by $\sim 2\Delta x = 9\text{\AA}$, which is the lateral resolution [104].

Tip shape with nanometric dimensions like this necessarily needs to undergo proper treatment. In the literature, it is possible to find several discussions and methods for tip sharpening [104]. The most common approaches are sharpening by (1) mechanical cut, which is quite useful for soft materials such as Pt-Ir alloys. The quality of the tip is usually obtained by try-and-error and it has presented good results even in the very early reports [96]. The most preferred technique is the (2) electrochemical etching. The procedure consists of promoting chemical corrosion of the metal in an electrolyte solution [104]. Another possibility is (3) tip sputtering at UHV conditions. The bombardment of the tip with non-reactive atoms eventually produces multiple sharp minitips.

Despite the increasingly advanced techniques, the best tip-apex dimensions obtained are always around $\sim 1\text{nm}$, as mentioned before, which does not explain the atomic resolution immediately. In fact, atomic resolution usually occurs by repeated tunneling and scanning for unpredictable time durations in a way that the precise mold of the tip is achieved during measurements. It can happen during controlled crashes on soft surfaces so that the tip eventually captures atoms and molecules; or by the application of controlled electrical discharges in order to reshape the tip by annealing. Thus, with atomic tip-apex size, the atomic resolution is achievable. In addition, the chemical elements at the apex also affect the quality of the measurement, because the nature and shape of the electronic orbitals have a considerable influence on the tunnel current (see A for more details).

4.1.2 Organic Adsorbates on Metal Surfaces

Regarding investigation of organic compounds adsorbed on metallic surfaces by STM, we must be aware that the physical/chemical interaction between adsorbate-substrate will directly or indirectly influence the tunneling current of the system, and consequently promote significant changes in measured topography and contrast characteristics. In these cases, we might summarize the tunneling phenomena in two main processes: direct via tip-sample/sample-tip, i.e, through the vacuum itself; or tunneling via accessing channels by electronic states of molecular orbitals, i.e, tip-molecular orbital and then molecular orbital-sample sequence or vice-versa. Of course, there might be a hybrid contribution of both tunneling processes, such as chemisorbed CO on Pt(111) reported by Bocquet *et al.* [105]. In general, the vast LDOS complexity of an adsorbate-substrate system will depend on the intensity and type of interaction (chemical or physical) involved. According to Mizutani proposal [106], an adsorbed compound can be physically interpreted as an additional potential barrier to the tip-sample system, as illustrated in Figure 4.2(a). The central barrier of width w_2 can be estimated by the molecular thickness and is characterized by the electronic states of the molecular orbitals that eventually serves as a channel for the transmission of tunneling current. w_3 is the gap between molecule and substrate and w_1 the gap between molecule and tip. In general, the occupied electronic levels on the ground state of the molecular orbitals (as well as the unoccupied ones) are far below (highest occupied molecular orbital - HOMO) or higher (lowest unoccupied molecular orbital - LUMO) the sample Fermi level and are inaccessible through the small tunneling voltages used in STM experiments. Furthermore, there are additional channels that can be created by vibrational phenomena [99], by photostimulation [102] or spin-excitons [107] in such cases inelastic tunneling are dominant.

The situation illustrated here, when the tunneling current, modulated by a bias V is able to access LUMO or HOMO, the molecular orbitals can be visualized with great precision [108, 109]. This type of resonant tunneling was interestingly approached by Mizutani *et al.* [110]. The proposed model of a physisorbed molecule on a metallic substrate can be simplified by a square potential well diagram as shown in Figure 4.2(a). In the scheme, a positive voltage V applied to the tip induce a potential difference between the Fermi energies of the electrodes and intensifies the probability of tunneling through the LUMO channel, so that if the $V + \Delta$ is sufficient, there is a significative increase of current

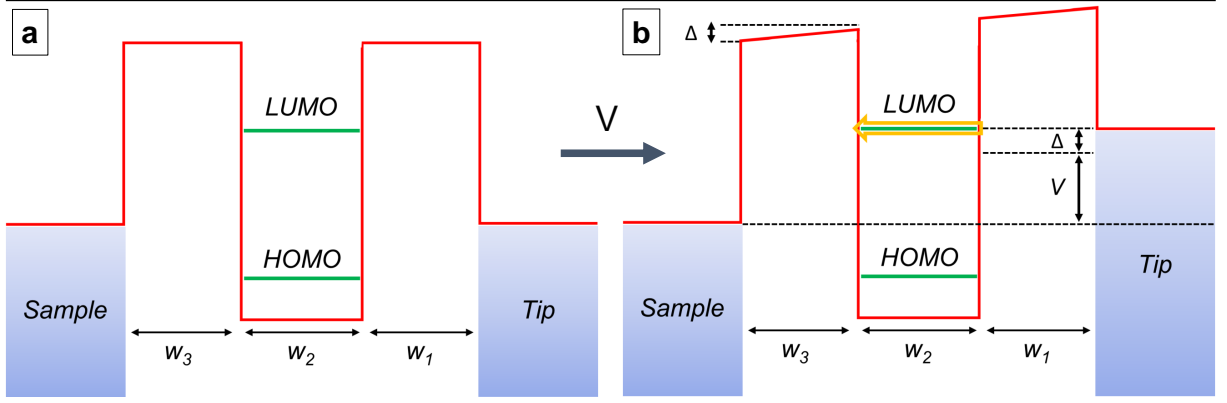


Figure 4.2: (a) One-dimensional square potential well diagram for an adsorbed molecule. w_1 and w_3 are the gap between molecule and tip and the gap between molecule and sample, respectively. w_2 is the central barrier characterized by the accessible electronic states of the molecular orbitals (HOMO-LUMO). (b) After bias V applied, the probability of tunneling increases. The yellow arrow shows the flowing tunneling current.

from the tip to the sample, as indicated by a yellow arrow in Figure 4.2(b). Obviously, through appropriate applied voltage, the tunneling can also be accessed through the HOMO channel.

In cases that resonant tunneling via molecular orbitals is negligible, i.e., when the bias voltage V is located between the HOMO-LUMO gap, we have a situation in which the microscopy is performing a simple scan of the electronic distribution of states induced by the adsorbate-substrate interaction. Spong *et al.* [111] proposed that, in general cases of chemisorption or physisorption, the contrast mechanism is related to the modulation of the local work function Φ of the substrate induced by the polarizability of the molecular adsorbates by the form

$$\Phi = \phi - e\mu/\epsilon_0 \quad (4.10)$$

ϕ is the work function of the clean surface, μ is the dipole moment density and ϵ_0 the permittivity of free space [112, 113]. In addition to the dipole moment, μ may depend on electric field effects induced by the distribution of modulating agents on the surface, or even on the field between tip and sample. So we can write $\mu = \mu_0 - f(\alpha, E)$, in which α is the polarizability of the adsorbate and μ_0 is the dipole moment density for the unperturbed case. Therefore, the conductance during scanning can eventually change dramatically since $G \sim e^{-\gamma}$ (see A.8) and $\gamma = \frac{\sqrt{2m\Phi}}{\hbar^2}$.

4.2 X-ray Photoelectron Spectroscopy (XPS)

Photoemission spectroscopy is established as one of the most important techniques in the study of the electronic structures of molecules, solids, and surfaces. The technique is based on the photoelectric effect, which was discovered by the physicist Heinrich Hertz when carrying out experiments with ultra violet radiation in 1887 [114]. The phenomenon was explained by Albert Einstein in his work on the quantum nature of light, in 1905 [115], and later verified experimentally by Robert Andrews Milikan in 1916 [116]. However, the necessary instrumentation to spectroscopic study for chemical analysis was only developed by Kai Siegbahn in Uppsala, Sweden, during the period 1955-1970, which earned him the 1981 Nobel Prize in Physics.

The technique, more than pure identification of the elements in a given sample, can precisely point out which reagents and products are responsible for the environment chemical modification. This distinguishable feature significantly changed the importance and approach of photoemission spectroscopy in practically all areas of the Physical, Chemical, and Biological sciences.

Great advances in electron spectroscopy techniques were also carried by the evolution of ultra-high vacuum (UHV) technologies, which allowed working in contamination-free environments; by the development of more sensitive electrostatic lens, monochromators and electron analyzers to better resolved spectral lines; new developments of photon sources, such as the new advanced synchrotron light sources and laser-based high-harmonic generators for a broad range of energy selectivity and resolution, time domain, space resolution, etc.

4.2.1 Basic Principles of XPS

The photoemission phenomenon is a photon-in/electron-out process that occurs when a monochromatic light of known energy $\hbar\omega$ excites a sample and extracts electrons from their state to the vacuum level. The kinetic energy K of these photoelectrons emerging from the sample is given by the expression:

$$K = \hbar\omega - E_B - \phi \quad (4.11)$$

where ϕ is the work function of the material and E_B is the binding energy of the electron attached to the nucleus of the corresponding atom [117].

Figure 4.3(a) illustrates the photoemission process for $\hbar\omega > E_B + \phi$, in which the kinetic energy distribution of the emitted electrons represents the density of occupied electronic states in the sample. These states are divided into valence and core levels. The levels that correspond to the valence band carry information about the orbitals involved in chemical bonds and are much less localized and potentially sensitive to environmental chemical changes. On the other hand, the core levels have well-located binding energies and are decisive in the specific chemical identification of the sample atoms and bonds.

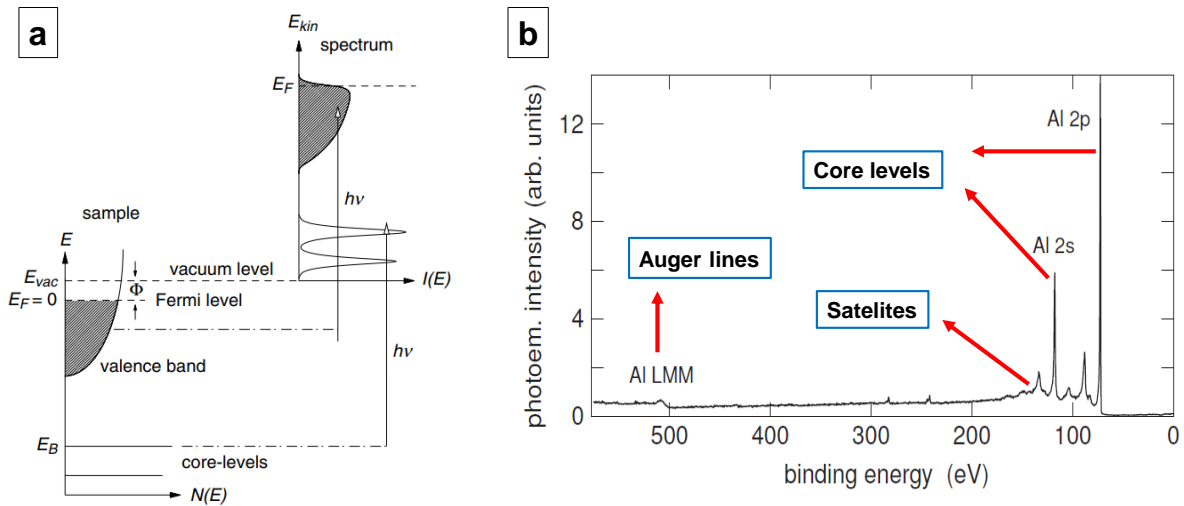


Figure 4.3: (a) Photoemission process in the single-particle picture. Electrons from the core-level with binding energy E_B can be excited with energy $\hbar\omega > E_B + \phi$ above the Fermi level and measured by the analyser with kinetic energy E_{kin} . Adapted from reference [117]. (b) XPS survey spectrum of an Al sample and its main features.

All photoelectrons ejected from its electronic shell are available to interact with other free electrons or phonons in the sample, triggering several scattering processes (elastic or inelastic), which can result in a complex spectrum in many cases. The illustrated example in Figure 4.3(b) shows the XPS survey spectrum of an aluminum sample and its main features. Core-level lines are processes originated by elastic scattering and are generally well-defined sharp peaks. When electrons are excited and emitted, they leave holes that will be filled by electrons from higher levels through a phenomenon of deexcitation, whereby the electron moving to the lower level loses an amount of energy equal to the difference in orbital energies and give rise to a characteristic x-ray spectrum. However, it is still possible that the energy stored in the deexcitation is transferred via Coulombic interaction to a second electron which is excited and expelled with specific Kinect energy giving rise to the so-called Auger peaks [118]. In Figure 4.3(b), the Auger LMM line represents the process in which a vacancy created in the L layer is filled by an electron of the M layer, exciting in sequence another electron in the same layer that will carry the equivalent kinetic energy of the process. Moreover, there are also core-level electrons that are inelastically scattered and promote collective excitations in the valence band, or even the presence of some screening mechanisms that are responsible to form a diversity of spectral features such as plasmons peaks, satellites of different nature (initial- or final-state, shake-up, shake-off and others) [118] as well as a characteristic inelastic background. They are represented in regions with lower kinetic energy located close to the sharp well-defined peaks.

4.2.2 Surface and chemical sensitivity

When we are working on probe low-dimensional materials on ultra-clean surfaces, we are looking to extract as much information as possible from the topmost layers of the sample. In an XPS experiment, the conventional or synchrotron X-ray source penetrates deeply into the bulk of the sample under analysis. However, due to the short inelastic mean free path (IMFP) of electrons in inorganic and organic materials, only information from the very first atomic layers of the surface reaches the electron analyzer. Thus, typical experiments in which the photoelectrons kinetic energies are between 10 and 1000 eV, the chemical information of approximately 10\AA in-depth is being probed (see Figure 4.4(a)). The surface sensitivity of the technique can also be increased by tuning

the electron kinetic energy with a synchrotron-based experimental setup or measuring in grazing emission angles θ (i.e. $\theta \geq 60^\circ$ from the surface normal) [119].

As previously mentioned, knowing the core-level binding energies we are able to identify the constituent elements of the sample. However, when investigating molecules and solids through this technique, we are not only interested in the element composition itself, but in the induced chemical shifts by the environment. In other words, screening or charge displacement promoted by electrons in the valence band or molecular orbitals will directly influence the binding energies of the electronic core-levels [118].

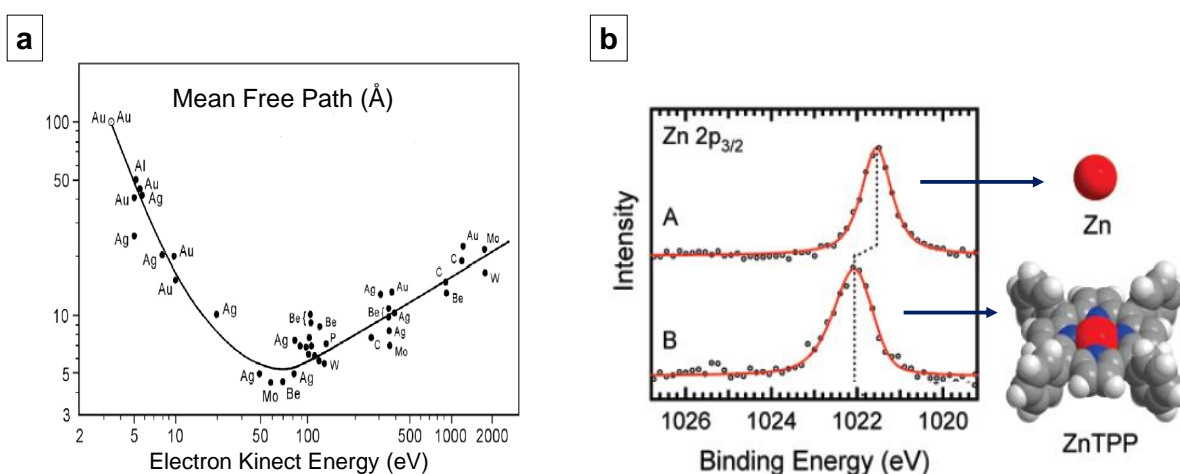


Figure 4.4: (a) "Universal curve" for the IMFP in function of the electron kinetic energy K . Each point represents individual measures for a different material. (b) XPS spectra for Zn 2p_{3/2} for atoms adsorbed on Ag(111) surface and functionalized on a ZnTPP molecule. Adapted from reference [120]

For example, for the analysis of metal surface-supported nanoarchitectures we can extract physicochemical information on the adsorbed state of the organic building blocks depending on the XPS peak positions of the metal center. Typically, in a sub-monolayer coverage regime, the core-level binding energy presents lower values relative to the multilayer regime because of the screening effect due to the presence of metal electrons [121]. Still, in the same context of functional molecular nanoarchitectures, we can follow the spectroscopic fingerprint for the Zn atom when adsorbed on Ag (111) crystal surface or functionalized in the macrocycle of a (meso-tetraphenylporphyrin)-Zinc(II) molecule (ZnTPP). As shown in Figure 4.4(b), there is a significant chemical shift in the Zn 2p_{3/2} XP spectra relative to each environment [120]. In summary, XPS becomes a very valuable tool in the chemical investigation of topmost atomic layers on surfaces and the influence

of organic adsorbates and reagents. So, it is especially crucial to master the technique if we are inspired by the bottom-up approach to synthesize low-dimensional materials and templates on metal surfaces.

4.3 Experimental setup

4.3.1 Background information

For a complete approach to the study of molecular adsorbates on crystallographic surfaces, there are some specific technical priorities that need to be attended. In particular, we seek to accurately determine the geometric, conformational, chemical, and electronic characteristics of molecular precursors, as well as the influence of catalysts elements or thermally activated reactions on the very sensitive interface environment. Both STM and XPS approaches effectively attend to these needs and arises as powerful tools for probing low-dimensional nanoarchitecture systems [12]. So that the complementarity between the techniques reaches the maximum of its capacities we must essentially operate our experimental apparatus under ultra-high vacuum conditions. An ultra-clean environment prevents surface contamination since as we know STM and XPS are both surface sensitive techniques.

From basic kinetic gas theory, we can quickly estimate the vacuum conditions for a reliable experiment. The numbers of molecules impinging on the surface is:

$$\frac{dN}{dt} = \frac{P}{\sqrt{2\pi M k_B T}} \quad (4.12)$$

where P is the pressure M is the molecular mass, T is the sample temperature, and K_B the Boltzmann constant. For a pressure of 10^{-6} mbar at room temperature, we would expect a rate of $\sim 10^{15}$ molecules per square centimeter impinging the surface. So if each rest-gas molecules stick to the surface, the latter only stays clean for a second or so [119]. Otherwise, UHV regime of about low 10^{-10} mbar, we have a few hours of clean surface conditions. In addition, the electrons emitted from a specimen should meet essentially no gas molecules in their way to the analyzer, otherwise, they might be scattered and lost in the process. In other words, the mean free path λ of the gas should be greater than the vacuum chamber dimensions d [122].

$$\lambda = \frac{k_B T}{\sqrt{2\pi M_D k_B T}} \quad (4.13)$$

M_D is the molecular diameter. When $\lambda \geq d$, we are working in the molecular flow limit, which is the case for typical UHV pressures. Additionally, analyzer, detectors,

and conventional X-ray tubes operate with high-voltage (HV) applied and the pressure inside the UHV chamber must be better than typically 10^{-8} mbar for a safe operation avoiding electrical discharge.

To achieve such an ultra-clean environment condition, we have at disposal a set of vacuum pumps specifically designed for this purpose. Without going into details, there are basically two main ways to get rid of the influence of gas molecules on the pressure inside a chamber: mechanically or by trapping. The roughing and turbomolecular pumps act together as high-frequency rotors that mechanically expel out the gases by collisions with fast-moving blades. On efficient pumping, the pre-vacuum stage is achieved by the roughing pump while the molecular regime is maintained by the turbomolecular pump, which operates in high frequency at the order of 800 Hz. Once low pressures have been established, it can also be maintained by ion or sublimation pumps. In the ion pumps, the rest gas is ionized by plasma discharge and accelerated to a reactive surface (typically Ti or Ti-alloys), in which stays trapped. In titanium sublimation pumps (TSP), the metal is sublimated in the chamber surfaces in order to increase the pumping effect, since it is also very reactive [119].

Another recurrent issue on UHV systems maintenance is the outgassing rate that adsorbed molecules on pipes, devices, and pumps leave the surface at room temperature. Usually, it depends on the experimental conditions that the system was previously submitted, or if it has been exposed to atmospheric pressure recently. In these cases, for example, water and carbon monoxide are very persistent and undesirable elements. So, to get rid of these compounds, we raise the temperature of the entire chamber up to 120-150 Celsius degrees for around 24h. By this method (called *baking*) we accelerate the outgassing process at first and, after cooling, it drops by several orders of magnitude so the pumps are then capable to stabilize the UHV desired conditions.

4.3.2 UHV system used in this thesis

Figure 4.5 shows the UHV system used in this Ph.D. project where the majority of experiments were performed. Located in the Department of Applied Physics of the Institute of Physics “Gleb Wataghin” (IFGW) at Campinas State University (UNICAMP), this Surface Science Group facility is equipped with two interconnected UHV chambers, one with an STM operating at mid 10^{-11} mbar pressure, and another with an XPS chamber at low 10^{-10} mbar base pressure (see Figure 4.5). This second chamber is also used for cleaning and sample preparation. It is essentially equipped with a conventional x-ray source and hemispherical electron analyzer, ion gun for sputtering, e-beam and Knudsen-cell evaporators for *in situ* deposition of atoms and molecules, a sample manipulator adapted with voltages supply for high-temperature annealing, and a Low Energy Electron Diffraction (LEED) optics for crystallographic surface characterization and cleanness verification.

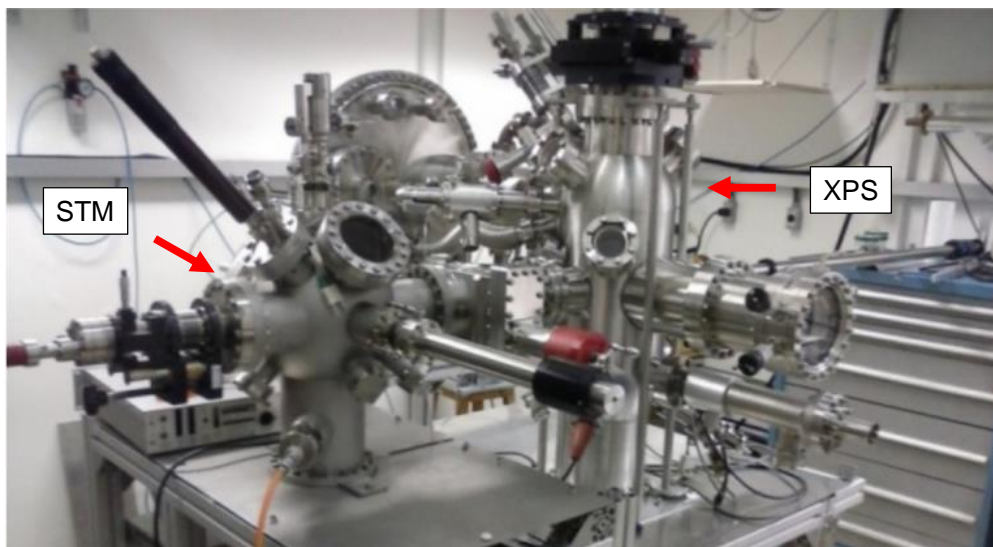


Figure 4.5: UHV system utilized in this project. GFS Group at IFGW-UNICAMP.

STM

The chamber for scanning probe microscopy is composed by an STM 150 SPECS Aarhus model (see Figure 4.6(a)) equipped with a SPECS 260 electronics and a variable temperature controller VTC 20. The model was designed for fast scanning capa-

bility and also allow a temperature-dependent approach, which is particularly interesting for molecular dynamics studies.

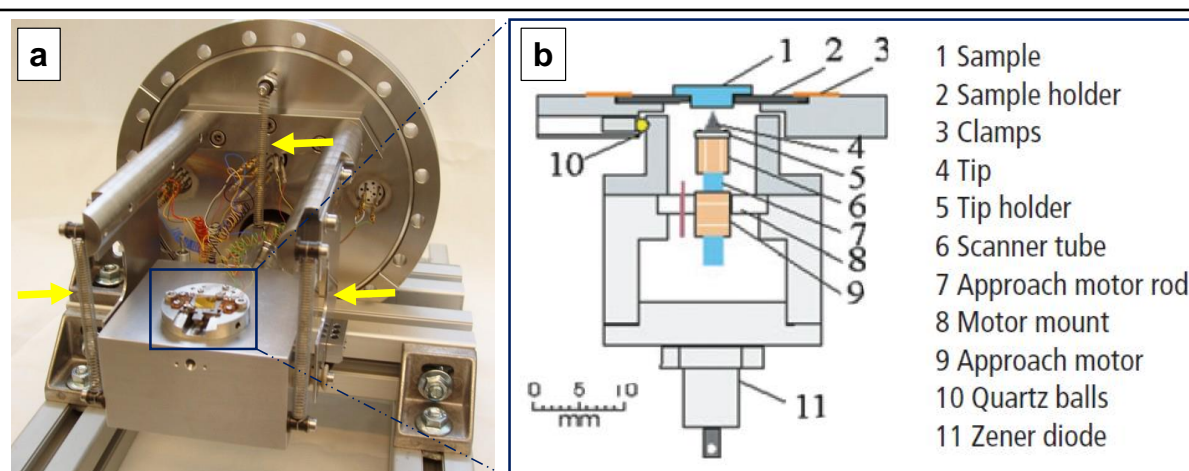


Figure 4.6: (a) STM 150 SPECS Aarhus model and (b) a vertical section profile graphic scheme with the relevant parts of the microscope. Details in text.

The microscope is attached to a conflat flange and hung by a set of springs, which are indicated by yellow arrows in the diagram. The massive metal block, called “cradle”, is also fixed by Viton rubber bands (not shown here) in order to achieve excellent damping stability. The sample holder (2) is located on top of the “cradle” so that the tungsten tip (4) is approached from the bottom up to perform the scanning. The graphic scheme in Figure 4.6(b) is a vertical section profile of the most relevant internal parts of the scanning unit. The control of these units is computationally performed by the electronics via the USB interface, which administrates all applying voltages to the scanner tube (6) and also reads in tunneling current and voltages. The scanner tube is composed of four identical piezoelectric ceramics segments so that when applying a high antisymmetric voltage, there is a contraction and expansion of the opposite tubes leading to a deformation with atomic precision in the x-y-directions. In the same way that when applying an internal voltage relative to all four piezo, the whole system moves in the z-direction, approaching or retracting the tip to the sample surface. This scanner tube is glued to a rod (7) and connected to the linear approach motor (9), also known as “inchworm”. The motor consists of a three-part segmented piezo tube with the upper and lower parts having the purpose of clamping and unclamping the rod, while the middle part contracts and expands by fast-moving steps in the z-direction, allowing retraction and approach

of the tip in a coarse way. All the experiments reported in this work were performed in constant current mode, i.e, the SPECS 260's feedback system prevents collisions while keeping constant the tunnel current in the system by varying the tip-surface distance according to sample topography.

The STM Aarhus 150 model was also designed to operate at $\sim (90 - 400)$ K temperature range. The VTC 20 controller is able to heat the sample holder, which is in direct thermal and electrical contact to the “cradle”, serving as a heat reservoir. If for any reason the piezo ceramics are subjected to high temperatures, it can depolarize or, in the worst case, do not respond to applied voltages anymore. That's why the STM and the plate that support samples are attached through three quartz balls (10) for thermal and electrical isolation. The “cradle” can be heated by passing a current through the Zener diode (11), which is especially interesting when performing low-temperature experiments. The samples get cooled by pumping liquid nitrogen (LN2) through the tubes of the pistons in the back of the STM (not shown here) while the “cradle” is not in the hanging position.

Finally, attached to the chamber and separated from the STM, there is an e-beam heating stage system with a thermocouple that touches the sample and that allows more complex and precise heat treatments before measurements. The temperature control, in this case, is carried out by electronics. The chamber is also equipped with a commercial Ar^+ ion gun for tip sputtering.

XPS

The energy spectra of the sample electrons are captured by the SPECS Phoibos 150 hemispherical analyzer. Figure 4.7 shows in a simplified way the interior of the vacuum housing and the main components of a hemispherical analyzer (HSA). The working principle of detection can be understood as follows: after the sample is excited by a conventional X-ray source (Mg and Al anodes in our case), the photoemitted electrons first pass through the electrostatic lens system until they reach the entrance slit S1. The input lens system has ten lens tubes that focus and retard the particles onto S1 defining the analysis area and the angular acceptance.

The experiments were performed operating in Fixed Analyzer Transmission (FAT) mode, which means that the voltage difference applied between the outer and inner hemispheres ($U_{OH} - U_{IH}$) is kept constant. Therefore, only particles that arrive at

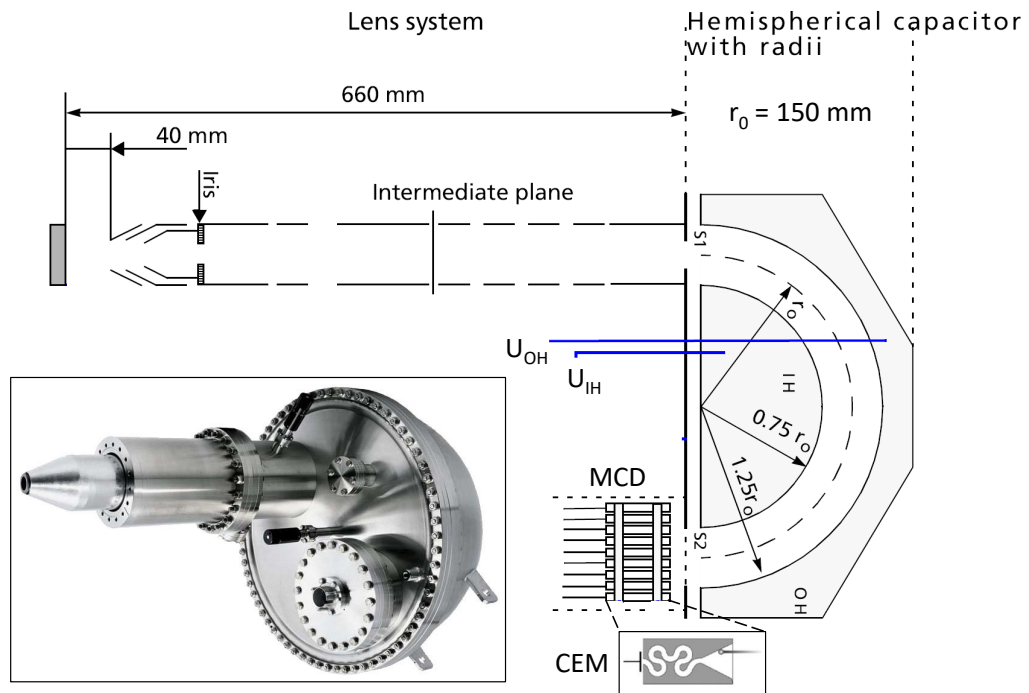


Figure 4.7: SPECS Phoibos 150 hemispherical analyzer. Figure shows the dimensions and the main components of the vacuum housing: Lens system, hemispherical capacitor and the Multichannel Detector (MCD) with 9 Channel Electron Multipliers (CEM).

S1 within certain pass energy are able to reach the exit plane S2 into the HSA. Finally, the electrons hit the Multichannel Detector (MCD) which is composed of an arrangement of 9 Channel Electron Multipliers (CEM) that amplify the signal to be transmitted to the computer software (see details in Figure 4.7).

4.3.3 Sample preparation

All sample preparations were predominantly carried out within a UHV environment so that the surfaces are ready to be analyzed with minimal contamination. Metal surfaces are generally very reactive and even after being inserted into the ultra-clean chamber, it is necessary to subject them to at least two basic cleaning procedures: sputtering and annealing. Sputtering cycles consist on accelerating ions directly towards the sample in order to physically promote the removal of some atoms or clusters of atoms from the surface. This process of erosion is performed in our facilities by an argon ion gun. Subsequently, heat treatment (annealing) is performed to desorb remaining impurities and reconstruct the surface that was eroded. Here, the back of the sample is e-bombarded by thermionic effect and elevated at the desired temperatures. Typically, a good surface reconstruction is obtained for annealing temperatures that are below 50 % of their surface melting point. Moreover, large terraces are obtained only when a slow ramp of heating and cooling is applied. This procedure is crucial to avoid surface faceting. In our system, a computer-controlled process was implemented for an automated annealing process. The typical annealing ramps used are heating at 1 K/s, maintaining to the set temperature for about 10 to 20 min and cooling at 0.5 K/s. After few cycles of sputtering and annealing the surface is clean and displays relative large terraces. The surface cleanness and the crystallographic quality is typically checked by LEED and XPS as well as by STM. After this procedure the surface can be used for molecules or atoms depositions [122].

Cu(111) substrate

The Cu(111) surface was cleaned by several cycles of sputtering (800 V) for 30 minutes keeping the chamber back filled with a low 10^{-6} mbar argon partial pressure followed by annealing under UHV at 850 K for approximately 15 minutes. All the temperature measurements were performed by a commercial infrared pyrometer. The conditions of cleanliness and quality of the surface were verified by STM, as shown in Figure 4.8.

Large and flat plateaus can be observed in several scanning areas, which indicates good representativeness of the sample surface. Figure 4.9(b) shows a region with high magnification and atomic resolution where is possible to determine the interatomic distances and the crystallographic directions of the surface. The Cu(111) single crystal has a cubic close-packed (ccp) structure with a 2.55 \AA surface lattice constant as veri-

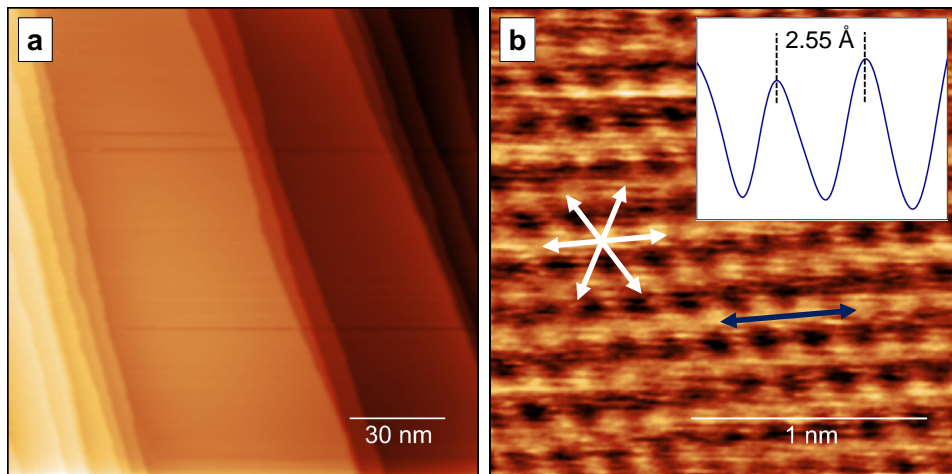


Figure 4.8: STM images for a clean Cu(111) sample. (a) Overview of a large representative region of the surface with area $A = (150 \times 150) \text{ nm}^2$. Tunneling parameters: $U = 1.44 \text{ V}$; $I = 0.3 \text{ nA}$. (b) High magnification image with atomic resolution. The white arrows indicate the $\langle 110 \rangle$ crystallographic directions and blue arrow is a short surface profile as shown in inset. Surface lattice constant $a = 2.55 \text{ Å}$. $A = (2 \times 2) \text{ nm}^2$; $U = -1.13 \text{ V}$; $I = 0.24 \text{ nA}$.

fied by the line profile at the top right corner of the image. The previous experimental determination of the $\langle 110 \rangle$ directions (white arrows in Figure 4.8(b)) is a fundamental geometric reference for studies regarding adsorption sites and conformation, self-assembly packing, activation energy barriers for molecular dynamics, etc.

Ag(111) substrate

For the Ag(111) single crystal, sputtering were performed with 600 V energetic argon ions at 2×10^{-6} mbar of argon partial pressure for 30 min followed by annealing at 790 K for 15 minutes. The crystal also presents a ccp structure with a 2.88 Å surface lattice constant, as corroborated by STM measurements shown in Figure 4.9.

Gr/Ir(111) substrate

The Ir(111) single crystal was prepared by several cycles of sputtering (1200 V @ 2×10^{-6} mbar @ 30 min) with subsequent annealing at 1600 K @ 10 min. The graphene growth was performed by the chemical vapor deposition (CVD) method keeping the crystal temperature at 1600 K with a propylene (99.9 %) back-filling the UHV chamber at 8×10^{-7} mbar for approximately 6 minutes. STM images of graphene on Ir(111) is characterized by a periodical hexagonal pattern forming a Moiré superstructure with a

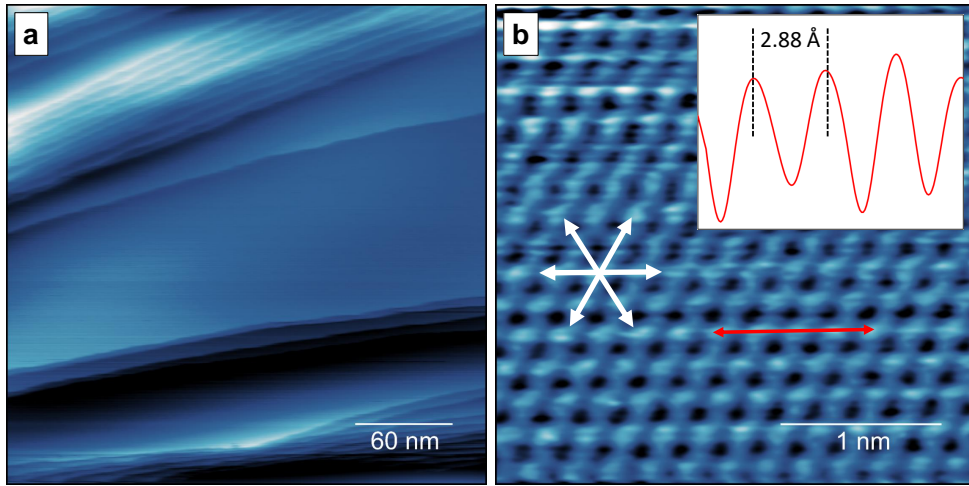


Figure 4.9: STM images for a clean Ag(111) sample. (a) Overview of a large representative region of the surface with $A = (300 \times 300) \text{ nm}^2$; $U = 1.44 \text{ V}$; $I = 0.19 \text{ nA}$. (b) High magnification image with atomic resolution. The white arrows indicate the $\langle 1\bar{1}0 \rangle$ crystallographic directions and red arrow is a short surface profile as shown in inset. Surface lattice constant $a = 2.88 \text{ Å}$. $A = (3 \times 3) \text{ nm}^2$; $U = 0.35 \text{ V}$; $I = 0.35 \text{ nA}$.

superlattice distance of $\sim 25 \text{ Å}$, resulted from the superposition of graphene layer on Ir(111). See Figure 4.10.

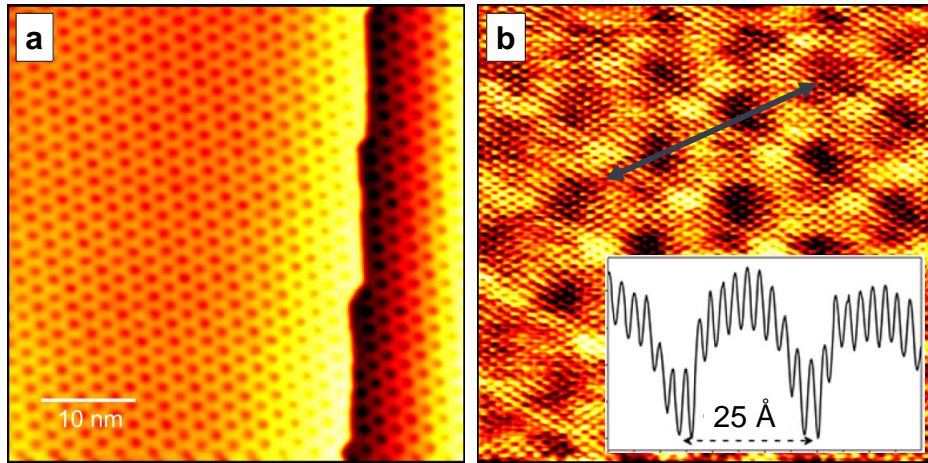


Figure 4.10: STM images for a clean Gr/Ir(111) sample. (a) Overview of a large representative region of the surface with $A = (50 \times 50) \text{ nm}^2$; $U = 1 \text{ V}$; $I = 0.11 \text{ nA}$. (b) High magnification image with atomic resolution of the Moiré pattern. The blue arrow is a short surface profile as shown in inset. Superlattice distance $a = 25 \text{ Å}$. $A = (7 \times 7) \text{ nm}^2$; $U = 0.52 \text{ V}$; $I = 1.32 \text{ nA}$.

Porphyrins and metals sublimation

The atoms were sublimated by conventional electron beam (e-beam) evaporators, model Scienta Omicron EFM3. Herein, the electrons released from a tungsten filament are accelerated to a target (1 mm metal rod 99.999%) heating it up to appropriate temperature so that the flux of evaporating atoms can be controlled and followed through electronic interface equipment. In fact we use a thin metal wire installed in front of the atom flux inside of the evaporator to measure a proportional electrical current (nA range) from the ionized atoms. Typical evaporation parameters for Fe, Co, and Pd are 1000 V at 6 mA filament emission maintaining an average flow rate at 10 nA, in order to evaporate equivalent to fractions of monolayers (ML) in an exposure period between 5 to 10 minutes. By measuring the covered area in the STM pictures the average surface coverage was determined in ML defined as one atom per adsorption site of the substrate. The Figure 4.11 exhibits a typical STM image of Cu(111) surface after deposition of ~ 0.3 ML of Pd at room temperature, where single atom thick islands are observed growing from the substrate step edges.

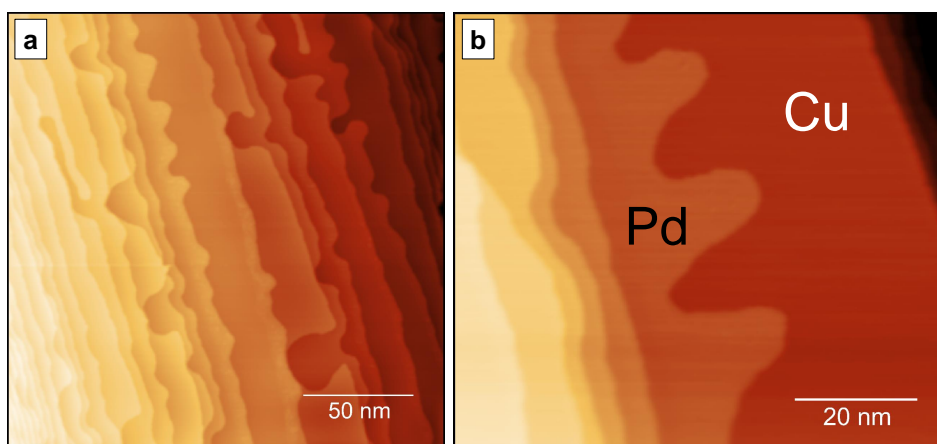


Figure 4.11: STM image of Pd on Cu(111) surface. (a) Representative image of Pd islands on Cu(111). $A = (200 \times 200) \text{ nm}^2$; $U = 1.4 \text{ V}$; $I = 0.13 \text{ nA}$. (b) High magnification inset of Pd growing on the Cu(111) step edges. $A = (80 \times 70) \text{ nm}^2$; $U = 1.4 \text{ V}$; $I = 0.12 \text{ nA}$.

In the case of organic molecules, the sublimation was performed by a home-made Knudsen-cell evaporator. Here, a tungsten filament is wrapped in a quartz crucible and heated by current control through a power supply. The temperature is followed by a thermocouple directly immersed inside the crucible and in contact with the porphyrin molecules. The free-base porphyrins TCNPP (5,10,15,20-(tetra-4-cyanophenyl)porphyrin)

and Cl₄TPP (5,10,15,20-(tetra-4-chlorophenyl)porphyrin) (see Figure 4.12) are commercially available and were supplied by Porphyrin Chemical Engineering. After preheating the evaporator along 30 minutes for degassing and thermal equilibrium, the temperature was kept constant at 553 K for Cl₄TPP and 623 K for TCNPP, so that in each individual case the coverage was determined by STM images following the ratio of adsorbates per unit area.

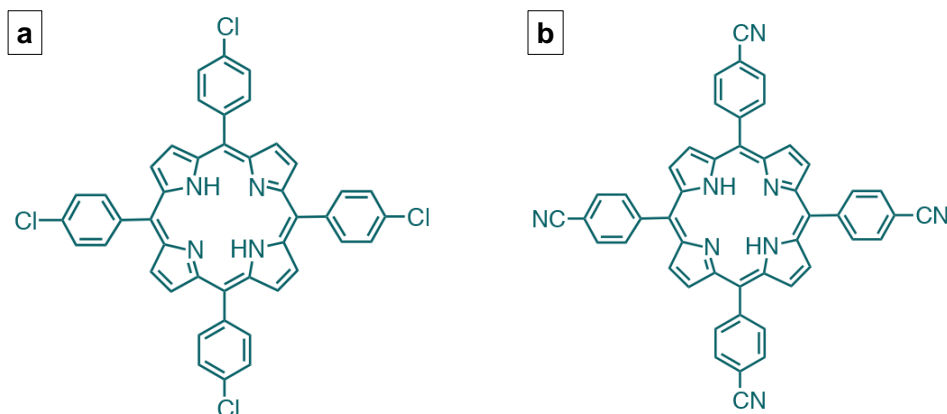


Figure 4.12: Free-base porphyrins utilized in this project (a) 5,10,15,20-(tetra-4-chlorophenyl)porphyrin (Cl₄TPP) and (b) 5,10,15,20-(tetra-4-cyanophenyl)porphyrin (TCNPP).

Chapter 5

Results

5.1 Introduction

Porphyrin-based molecules have a flat, highly rigid structure, high chemical coordination with metal complexes and are especially stable at relatively high temperatures above RT. They also present possibilities for attachment of several reactive branches, which can assist in coupling and forming more complex nanostructures. Halogenated compounds have, as we already discussed by the literature, low dissociation energies from the peripheries of the organic compounds, which justifies the choice of Cl₄TPP as an excellent precursor for polymerization via on-surface Ullmann reaction. Bromophenyl and Iodophenyl porphyrins have been observed in several systems in the literature on reactive surfaces and show, in general, dissociation energy at temperatures below RT (especially for Ag and Cu), which makes it difficult to carry out and control a more detailed study of the reactions and intermediate products. In addition, our experimental limitation hinders maintaining the temperature of the sample cooled during deposition. In this respect, chlorine presents itself as an interesting candidate as it can be manipulated at temperatures slightly above RT. Carbonitrile porphyrins are also highly reactive and lying flat on surfaces to form 2D organometallic complexes. In this sense, 2H-TCNPP is also a very interesting candidate to explore the formation of intermediate organometallic compounds to the Ullmann reaction.

The study, as mentioned in Chapter 3, combines experimental XPS and STM techniques, in addition to DFT calculations and STM simulations that provided extremely

important support and corroborated the research in many aspects. More details on DFT and the implemented functionals for the calculations in each system, see B

5.2 Cl₄TPP on Cu(111)

Herein we performed a combined STM, DFT and XPS study of 5,10,15,20-(tetra-4-chlorophenyl)porphyrin (Cl₄TPP) (Fig. 5.1), on Cu(111). This metal substrate usually presents a strong interaction with the precursors, which may favor the on-surface reactions to polymerization. Through this detailed study, we were able to image and unequivocally characterize the initial, intermediate and final species of the system, tracing the preferred chemical pathway for the on-surface reactions. The study was essential to extract important information into the Ullmann coupling contributing significantly in the technology field that seeks to develop atomically precise manipulation and synthesis technique of nanostructured 2D materials on metal surfaces.

RESULTS AND DISCUSSION

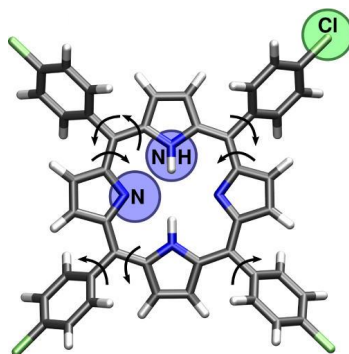


Figure 5.1: Top view of the optimized gas-phase structure for Cl₄TPP. C, H, N, and Cl atoms are marked in grey, white, blue, and green, respectively. Partial out-of-plane rotations of the chlorophenyl and pyrrole rings are denoted by arrows. The separations between Cl atoms are 1.34 and 1.35 nm, parallel and perpendicular to the N-H bonds, respectively.

The relaxed configuration of the Cl₄TPP in the gas-phase adopts a square nonplanar shape, with the pyrrole and chlorophenyl rings rotated around the C–C bonds, as indicated in Figure 5.1. This configuration is not expected when the molecule adsorbs on metal surface, which depends on the nature of molecule-substrate interaction. Immediately after evaporating a submonolayer coverage on Cu(111), the adsorbates are isolated and very mobile on the surface. We are considering here a deposition done a maximum of 6 hours before the measurements, defining it as a “freshly” sample. Mobility is characterized by blur regions on the STM images, in which molecules are difficult to resolve during scanning (yellow circles on Figure 5.2(a)); or partial-imaged molecules, the result of hop

between neighbor sites during the scan (yellow dotted circles). However, after sufficient time for the system to acquire the equilibrium, several molecules are interconnected in chains and with less mobility, trapped on the surface and on each other somehow (see Fig. 5.2(b)). It means that there is a time- and temperature-dependent reaction occurring on the surface. Moreover, by cooling the samples down to 233 K, we drastically reduce the mobility and are able to precisely resolve individual molecules. This also indicates that there is a high activation barrier for surface migration. To gain deep information on molecule-substrate interaction we performed the Arrhenius analysis.

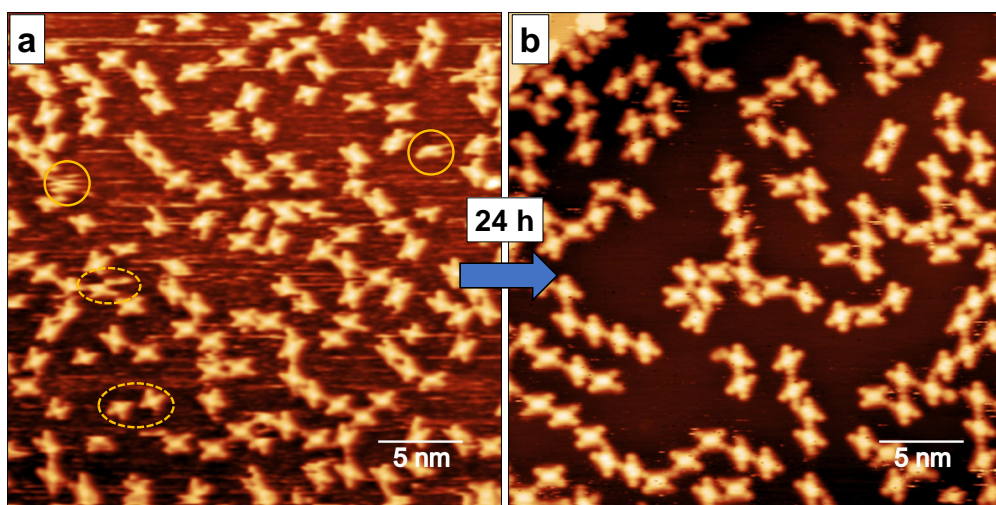


Figure 5.2: ($A = 30 \times 30 \text{ nm}^2$) STM image of a representative region of Cl_4TPP on $\text{Cu}(111)$ (a) immediately after submonolayer deposition ($U = -1400.5 \text{ mV}$; $I = 0.14 \text{ nA}$) and (b) after a 24 hours period ($U = -1444.1 \text{ mV}$; $I = 0.12 \text{ nA}$) Yellow circles identify mobile molecules.

The Arrhenius method is a standard approach to extract quantitative information from temperature-dependent on-surface reactive processes. Through it, it's possible to determine the energy barriers of diffusion, rotation, self-metalation, exchange, etc. The general Arrhenius equation is [123]:

$$r(T) = A \cdot e^{-\frac{E}{k_B T}} \quad (5.1)$$

an exponential expression, where E is the activation energy barrier of the reactive/diffusion process and A is the pre-exponential factor that has dimension of frequency.

The practical process for determining the migration energy barrier (E_m) of Cl_4TPP on $\text{Cu}(111)$, for example, consists of statistically calculating the mean square

displacement $\langle \Delta x^2 \rangle$ of the ensemble at a certain temperature T (K) in order to determine the molecular hopping rate [124, 125]

$$h(T) = \frac{\langle \Delta x^2 \rangle}{\langle \lambda \rangle^2 \cdot t} \quad (5.2)$$

The hopping rate is directly related to the transposition of the migration barrier when molecules jump between adjacent adsorption sites. In the case of Cl₄TPP on Cu(111), the molecules perform single jump steps, i.e. λ is the lattice constant of 2.55 Å along the $\langle 1\bar{1}0 \rangle$ directions. Figure 5.3(b) (see video) represents a superimposed sequence of 55 consecutive frames at 273 K for approximate 1969 seconds in which it is possible to follow the Cl₄TPP trajectory on the three symmetric directions for each individual molecule. Figure 5.3(a) is the very first frame of the sequence and each molecule is marked on its initial position. The individual path is indicated in colors to facilitate the visualization. Thus we can follow the path of each porphyrin by STM, extract the relative position frame-by-frame, and consequently, the mean square displacement $\langle \Delta x^2 \rangle$ for the corresponding time interval t . All data visualization, analysis of images, and sequencing of frames were performed by the softwares Gwyddion [126] and WSxM [127].

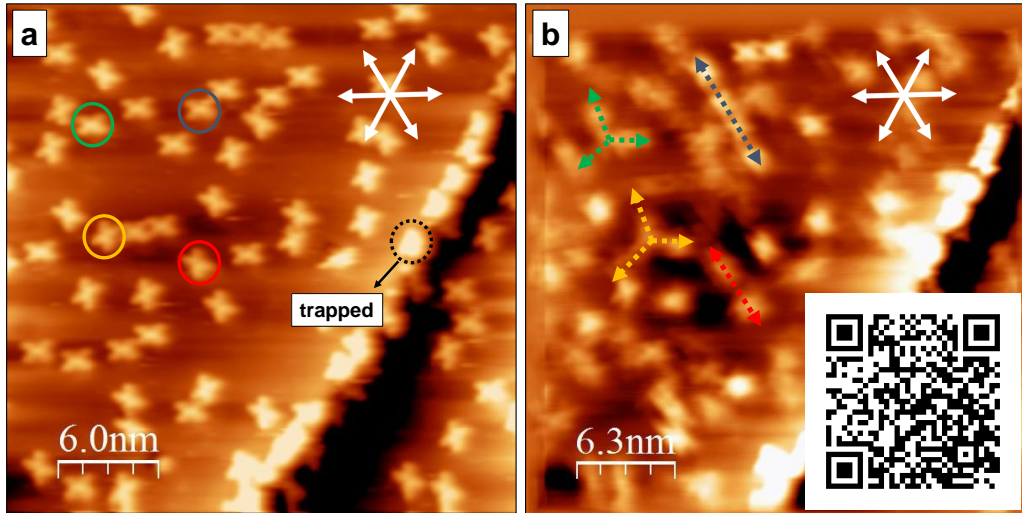


Figure 5.3: Arrhenius analysis for Cl₄TPP molecular diffusion on Cu(111). (a) STM image showing the initial frame of a 1969 seconds movie at 273 K. Molecules marked in red, green, yellow and blue will be followed. (b) Superimposed image of 55 consecutive frames. The colored arrows show the Cl₄TPP paths along the $\langle 1\bar{1}0 \rangle$ directions. $A = (30 \times 30) \text{ nm}^2$. Tunneling parameters: $U = -1.4 \text{ V}$, $I = 0.14 \text{ nA}$.

It is also necessary to ensure that no tip-induced effect interferes with the measurements. Several molecular diffusion studies on single-crystal metal substrates were

carried out with tunneling resistance in the range between 1-10 G Ω or above [128–130]. In this study, all STM measurements were performed roughly with $R \sim 10$ G Ω ($U \sim 1.5$ V and $I \sim 150$ pA). Furthermore, to avoid molecule-molecule interactions, low surface coverage must be addressed, just as trapped molecules at the surface must be ruled out of statistics. When the hopping rate determination for each temperature is completed, the data is plotted as $\ln(h)$ vs. $1/T$ and compared to the Arrhenius equation for surface diffusion so that: $h(T) = A_m \exp[-E_m/(k_B T)]$ [124]. Thus, the slope of the linear fit yields the diffusion migration barrier. The same procedure was done to the rotation energy barrier.

Figure 5.4 shows the analysis of the surface diffusion and rotation behavior of Cl₄TPP on Cu(111) via Arrhenius plot of the temperature-dependent rates. Similar to other tetraphenylporphyrins [130], Cl₄TPP moves only along the three main $\langle 1\bar{1}0 \rangle$ directions and exhibits discrete rotations of $\pm 60^\circ$. The data shows a linear dependence, consistent with the Arrhenius equation. From the slope, we obtain the migration barrier of $E_m = 0.77 \pm 0.09$ eV, and from the intercept an attempt frequency of $A_m = 10^{13 \pm 2}$ s⁻¹. These values are comparable to $E = 0.71 \pm 0.08$ eV and $A = 10^{10.9 \pm 1.4}$ s⁻¹ for TPP [130]. The slightly higher migration barriers suggests a stronger molecule-substrate interaction for Cl₄TPP compared to TPP. Similarly, from the linear fit to the surface rotation data, we determine the rotation barrier $E_r = 0.93 \pm 0.28$ eV and the corresponding attempt frequency $A_r = 10^{15 \pm 5}$ s⁻¹. The higher barrier for rotation compared to migration is again suggestive of a covalent interaction between molecule and substrate.

Our STM measurements of Cl₄TPP on Cu(111) show individual molecules with a rectangular symmetry characterized by four bright protrusions at the corners of the molecules and two bright central ovals (Figure 5.5(a)). To precisely measure individual molecules, we have performed statistical analysis of several STM images, determining the dimensions: $a = 1.47 \pm 0.05$ nm and $b = 1.11 \pm 0.05$ nm, with a separation between the two bright central ovals of $d = 0.46 \pm 0.05$ nm. This indicates that surface adsorption on Cu(111) elongates the porphyrin, reducing the symmetry from square to rectangular. Since STM measurements only provide geometrical information indirectly via the local electronic density of states, often their interpretation is not straightforward. To obtain deeper insight into the molecular conformation, we have performed DFT calculations

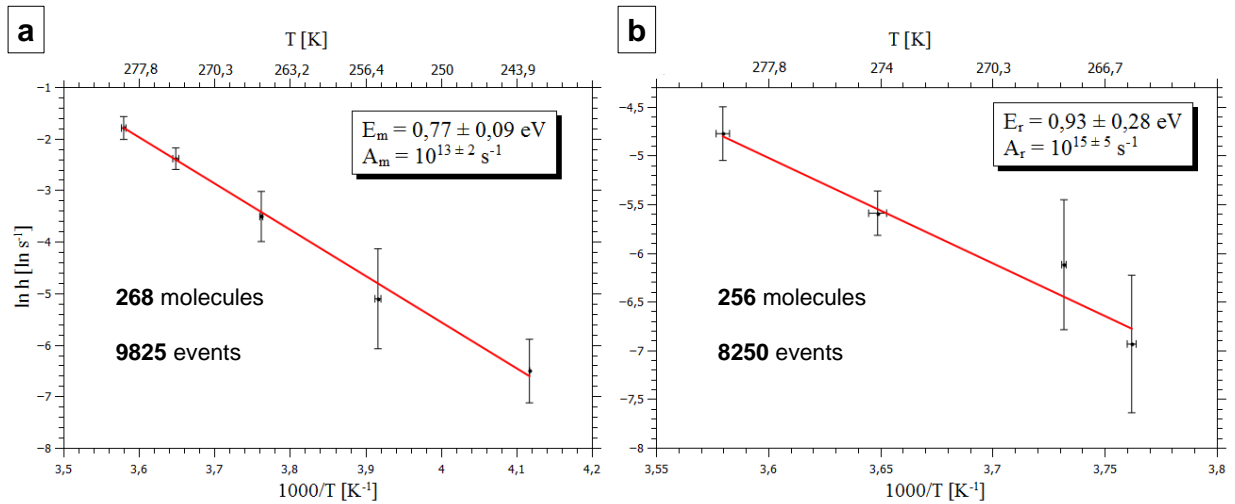


Figure 5.4: Arrhenius plot for (a) the surface migration and (b) rotation of Cl_4TPP on $\text{Cu}(111)$ with activation barriers E of 0.77 ± 0.09 and $0.93 \pm 0.28 \text{ eV}$ and attempt frequencies A of $10^{13 \pm 2}$ and $10^{15 \pm 5} \text{ s}^{-1}$, respectively. Graphs also indicates the number of molecules and events analysed in each case.

with structural relaxations of individual Cl_4TPP molecule on $\text{Cu}(111)$ for the two main conformations of surface-adsorbed porphyrins [43, 47, 80].

Figure 5.5 shows our relaxed DFT structure (wire-frame model) and the resulting STM simulation. The overall structure is almost parallel to the surface, except for the two opposing pyrrole rings (NC_4). These rings undergo a drastic rotation of $\sim 100^\circ$ with respect to the surface plane, with their iminic ($=\text{N}-$) atoms pointing toward the $\text{Cu}(111)$ surface. The simulated STM image (Figure 5.5(b)) clearly reproduce the mains features observed by STM. Also, the calculated separations between the external Cl atoms: $a_c = 1.56 \text{ nm}$, $b_c = 1.07 \text{ nm}$ and between the rotated pyrrole groups $d_c = 0.52 \pm 0.05 \text{ nm}$, show a very good agreement between theory and experiment. In this distorted configuration, the distance between the two pyrrole rings is too large to have significant face-to-face $\pi - \pi$ interactions [131–133]. Therefore, this drastic pyrrole rings rotation must be stabilized mainly by the interaction between the two iminic ($=\text{N}-$) atoms and the $\text{Cu}(111)$ surface. Indeed, our DFT relaxed structures show that covalent ($\text{N}-\text{Cu}$) bonds are formed in a bridge position with a lenght of about 2.3 \AA . This is consistent with our high measured activation barrier for surface migration and rotation arising from chemisorption rather than physisorption. Moreover, the separation between the rotated pyrrole rings ($d = 0.52 \pm 0.05 \text{ nm}$) is commensurate with $\text{Cu}(111)$, i.e., the neighbor separation of $2 \times 0.255 \text{ nm}$ along the $\langle 1\bar{1}0 \rangle$ directions (see Fig. 5.6(b)). This differs from

other metals, where the separation of 0.58 nm would require further rotation leading to steric hindrance between the rotated pyrrole rings.

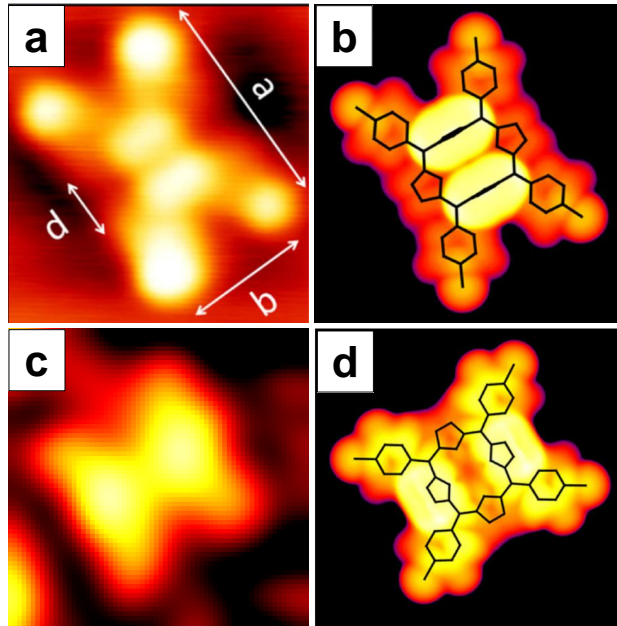


Figure 5.5: STM images of individual species of Cl_4TPP as deposited on $\text{Cu}(111)$. (a) high-resolution measurement of an inverted ($T = 233 \text{ K}$, $A = 2 \times 1.5 \text{ nm}^2$, $U = -1.5 \text{ V}$, $I = 0.13 \text{ nA}$) and (b) its DFT and STM simulation. (c) Rare observed saddle porphyrin ($T = 300 \text{ K}$, $A = 2.2 \times 2.1 \text{ nm}^2$, $U = -1.5 \text{ V}$, $I = 0.13 \text{ nA}$) and (d) its DFT and STM simulations.

Lepper *et al.* [43, 47] reported this extremely distorted configuration for CN and H terminated porphyrins, naming it “inverted” structure, as seen previously by Albrecht *et al.* [134]. This inverted adsorption structure for free-base TPP’s on $\text{Cu}(111)$ was recently validated by Ryan *et al.* [44]. In previous works, the most commonly reported conformation of surface-adsorbed porphyrins was the so-called “saddle” structure [10, 135, 136]. To check this possibility, in Figure 5.5(d), we show our relaxed DFT structure (wired-frame model) and the resulting STM simulation for Cl_4TPP adsorbed on $\text{Cu}(111)$ in the saddle conformation. Comparing Figure 5.5(a)-(d), we find that the STM simulation for the inverted conformation is in better agreement with the measurement than for the saddle conformation. In particular, Figure 5.5(a) does not feature the central gap, two opposing “banana” structures, and more squarish shape of Figure 5.5(d), which are, however, in excellent agreement with the “saddle” configuration rarely observed here but frequently reported for similar molecules. Moreover, our DFT calculations show that Cl_4TPP is physisorbed on $\text{Cu}(111)$ when in the saddle conformation, with a $\text{N} \cdots \text{Cu}$ sep-

aration of 3.0 Å. This physisorption is inconsistent with the high activation barriers we observe for surface migration and rotation (Figure 5.4).

Finally, careful observation of Figure 5.5(a) finds a brighter STM contrast in the diagonally opposite Cl atoms. To explain this observation, we have performed DFT calculations for the adsorbates on Cu(111) with Cu adatoms underneath the Cl atoms which exhibit a brighter contrast. The resulting STM simulation is shown in Figure 5.6(a), with top and side views of the structure shown in Figure 5.6(b) and (c), respectively. Thus, the presence of the two anchoring Cu adatoms explains why this particular molecule was stationary during 20 consecutive STM measurements. However, most of our STM data exhibited a uniform contrast between the Cl terminating groups, resembling Figure 5.5(b).

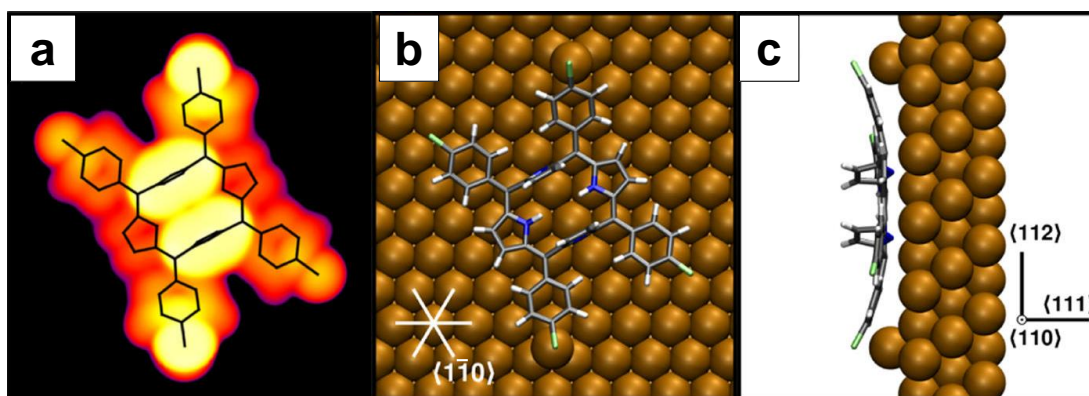


Figure 5.6: (a) STM simulation and schematic (b) top and (c) side views of Cl₄TPP on Cu(111) with Cu adatoms underneath diagonally opposite Cl atoms. C, H, N, Cl and Cu atoms marked in gray, white, blue, green and brown, respectively. Arrows in (b) and (c) indicate the $\langle 1\bar{1}0 \rangle$, $\langle 111 \rangle$ and $\langle 112 \rangle$ crystallographic directions of Cu(111).

Overviews of the samples show that Cl₄TPP molecules are oriented in three equivalent crystallographic directions with their long axis oriented along the $\langle 1\bar{1}0 \rangle$ main directions of the substrate (Figure 5.7(a)). To obtain a deeper insight into the molecule-molecule interactions, we have analysed the main bond motifs observed between neighboring molecules. On one hand, some molecules are bonded via single side-on interactions, as shown in Figure 5.7(b). In this configuration, the Cl atoms of neighboring molecules are placed beside each other. This configuration is consistent with a non-covalent type I vdW halogen...halogen interaction, where the C–Cl...Cl angles are approximately equal ($\theta_1 = \theta_2$), as depicted in Figure 5.7(c) [137, 138]. For our relaxed DFT structure, we obtain $\theta_1 = 97^\circ \approx \theta_2 = 107^\circ$ and an intermolecular Cl...Cl distance of 3.54 Å, consistent with the sum of two Cl vdW radii of 3.50 Å.

Moreover, we performed a DFT analysis in a way that two Cl₄TPP molecules were placed on a Cu(111) surface where they were brought together to form the desired bond and then allowed to relax. The result is in excellent agreement with our STM measurements (dashed rectangle of Figure 5.7(a), both in the dimensions and in the overall appearance. On the other hand, some molecules are bonded via single head-on interactions (dotted and dashed ovals). In these configurations, the “arms” of neighboring molecules are co-linear, that is, directly facing each other. From the STM measurements, two different kinds of single head-on interactions can be clearly distinguished, with one (dotted oval) 0.54 nm longer than the other (dashed oval). The longer single head-on interaction (dotted oval) is consistent with a noncovalent type I vdW Cl···Cl interaction ($\theta_1 \approx \theta_2 \approx 180^\circ$), whereas the shorter single head-on interaction is covalent in nature. This results suggest that after deposition at room temperature some molecules undergo cleavage of the C–Cl bonds as part of the on-surface Ullmann coupling reaction.

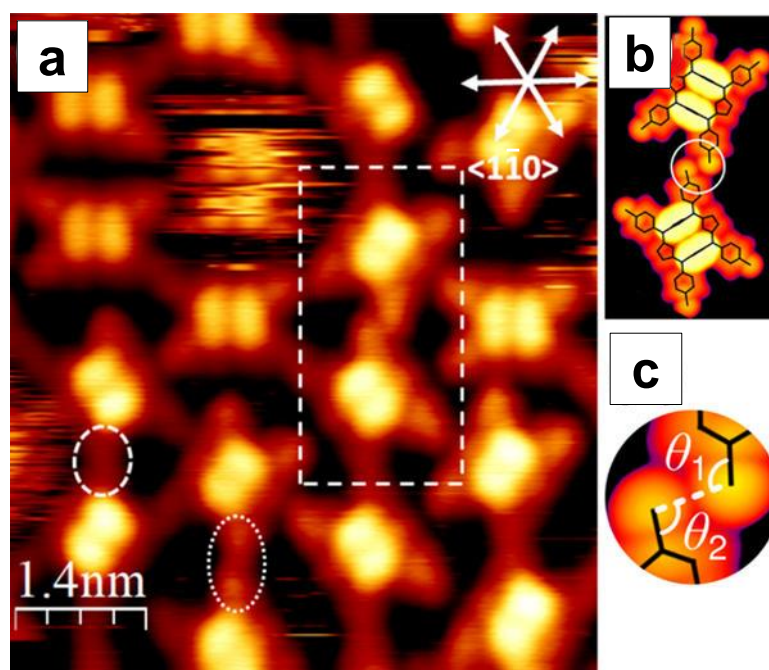


Figure 5.7: (a) STM measurement after deposition of Cl₄TPP on Cu(111) ($T = 300$ K, $A = 7.0 \times 7.0$ nm², $U = -1.5$ V, $I = 0.13$ nA). van der Waals (vdW) (dotted oval) and covalent (dashed oval) and single “head-on” interactions and a single “side-on” (dashed rectangle) interactions are marked. (b) STM simulation of the latter (dashed rectangle in (a)), a type I van der Waals interaction ($\theta_1 \approx \theta_2$), as shown in (c). The white arrows shown in (a) indicate the $\langle 1\bar{1}0 \rangle$ crystallographic directions of Cu(111).

However, the relative ratio between head-on and side-on interactions is time- and temperature-dependent. As mentioned and depicted in Figure 5.2, a “freshly” de-

posited sample typically has many isolated molecules. However, after 24 hours at room temperature, the isolated molecules are extremely rare and almost all ($\sim 99\%$) of molecules are involved in head-on/side-on interactions. Taking into account that the growth of molecular structures on surfaces is intrinsically a non-equilibrium process governed by a competition between kinetics and thermodynamics [139], our results clearly suggest that some molecules do not react after deposition due to the kinetics, i.e., the activation barrier that they need to overcome or a limiting reagent for the process (e.g., Cu adatoms). To gain additional insight into the chemical environment as function of the annealing temperature, we performed XPS and STM measurements. In Figure 5.8(a)-(c), is shown a summary of the dependence on annealing temperatures of the XPS data for Cl atoms and Figure 5.8(d)-(f), the respective STM overview of the sample at the respective temperatures.

XPS measurements of a “freshly” deposited sample of Cl₄TPP on Cu(111) show a main set of two peaks in the Cl region, which represent $\sim 61\%$ of the total integrated area (blue fitting, Cl(1)). These peaks have a binding energy of 200.2 and 201.9 eV for the Cl 2p_{3/2} and 2p_{1/2}, respectively, in excellent agreement with the reference values for Cl atoms in chlorobenzene (C₆H₅Cl) [140]. This allows us to assign the Cl(1) peaks to Cl atoms bonded to the molecules. As we increase the annealing temperature of the samples, the Cl(1) peaks start to decrease, whereas the Cl(2) peaks (orange peaks in Figure 5.8) increase in magnitude. The binding energies of the Cl(2) peaks are 198.2 and 199.7 eV for the 2p_{3/2} and 2p_{1/2} components, respectively, in quantitative agreement with the reference values for CuCl₂ [140]. Based on this, we can attribute the Cl(2) peaks to Cl atoms that are cleaved from the molecule and are strongly interacting with the Cu substrate. XPS shows that, as the samples are annealed, Cl atoms are gradually cleaved from the molecules, suggesting that the rate-limit step for cleavage is a limiting reactant (e.g., Cu adatoms) rather than a kinetic activation barrier. The presence of Cl(2) peaks at RT confirms the cleavage of Cl atoms observed by STM in Figure 5.7.

Additionally, at 400K, few dechlorinated molecules indicate self-metallation, as shown in white dashed circles in Figure 5.9(b). The phenomenon is reflected chemically in the orange photoemission peak at 398.3 eV in the Figure 5.9(a). It means that the molecule macrocycles are now functionalized with Cu adatoms from the surface. During annealing, the iminic nitrogen (=N–), represented by the green peak at 399.8 eV and the pyrrolic

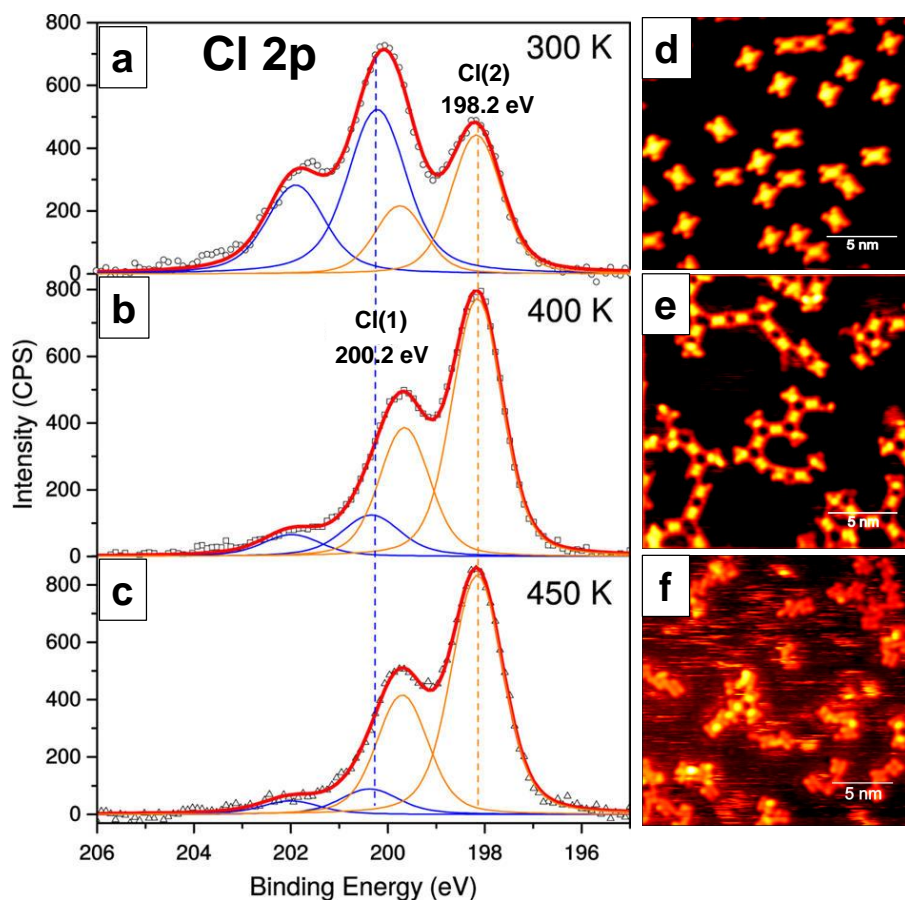


Figure 5.8: Cl 2p XPS spectra and STM images after deposition of Cl₄TPP on Cu(111) (a), (d) as grown at $T = 300$ K, and after performing post-deposition annealing at (b), (e) $T = 400$ K and (c), (f) $T = 450$ K for $t = 30$ min. Experimental fits (red lines), individual components from Cl attached to porphyrins (blue lines) and as adatoms (orange lines) on Cu(111), with the fitted Cl 2p_{3/2} binding energies (dashed lines) at 200.2 and 198.2 eV, respectively, are shown. The area ratios of Cl in porphyrin to Cl adatoms obtained from the deconvolutions are (a) 61:39, (b) 17:83, and (c) 11:89. (d) $U = -1.7$ V, $I = 0.23$ nA. (e) $U = -1.5$ V, $I = 0.22$ nA. (f) $U = -1.5$ V, $I = 0.19$ nA. ($A = 20 \times 20$ nm²).

nitrogen ($-\text{NH}-$) (blue peak) at 398.1 eV vanish. Finally, we have complete dechlorination and self-metalation at 450 K for 30 minutes annealing. In STM measurements, this is reflected in the molecular contrast, so that the precursors have now a smaller and compact format compared to the inverted structure. Moreover, the molecules grouped in blocks are very mobile, which is characteristic of metallated species [80]. This feature is observable when the scanned images show regions with blurriness or noises, that is, molecules that were not properly resolved during the microscope scan (see white dashed square in Figure 5.9(c)).

To determine if after the Cl cleavage the molecules are stabilized by C–C covalent bonds or by C–Cu–C organometallic bonds, we performed DFT simulations of

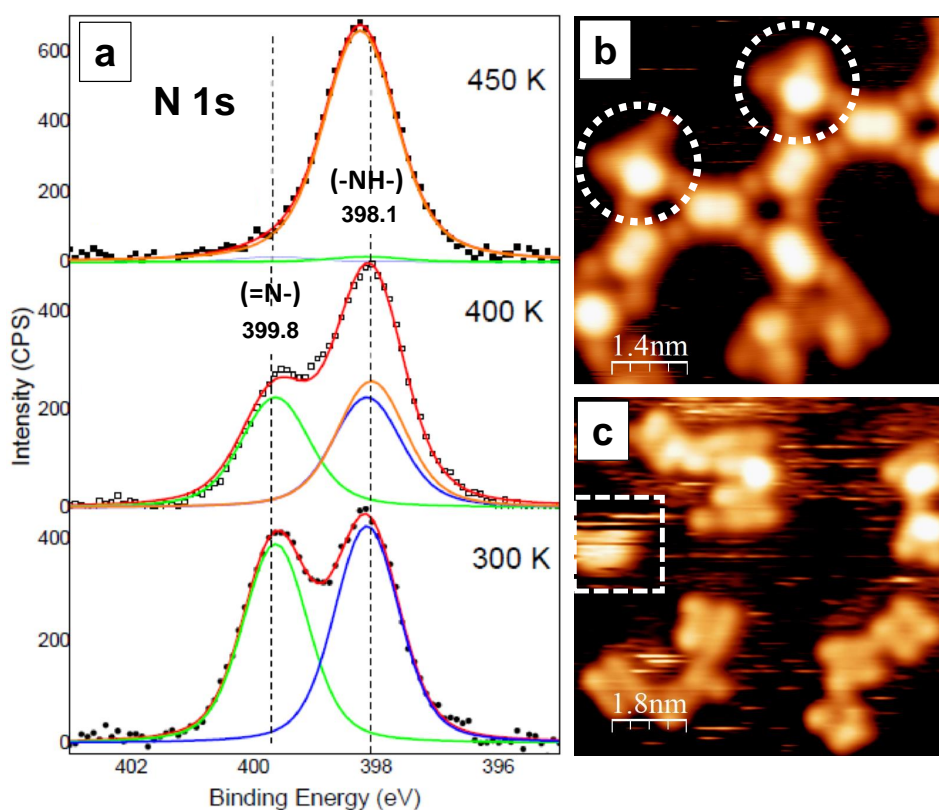


Figure 5.9: (a) N 1s XPS spectra and STM images of Cl₄TPP on Cu(111) in function of temperature. Green components represent the iminic nitrogens (=N-) at 399.8 eV. Blue components the pyrrolic nitrogens (-NH-) at 398.1 eV. And orange component are the metalated species at 398.3 eV. (b) STM image of molecular chains after annealing at 400 K for 30 minutes. In white dashed circles, the contrast indicate self-metalated species. ($A = 7 \times 7 \text{ nm}^2$) ($U = -1.5 \text{ V}$, $I = 0.22 \text{ nA}$) and (c) after annealing at 450 K for 30 minutes. White dashed square indicates mobile species. ($A = 7.2 \times 7.2 \text{ nm}^2$) ($U = -1.5 \text{ V}$, $I = 0.19 \text{ nA}$).

these structures. Figure 5.10(a),(b) shows the DFT relaxed structure (wire-frame model) for C-Cu-C organometallic bonds and C-C covalent bonds, respectively. Although the STM simulation of C-Cu-C organometallic bonds shows a bright protrusion in the bond between the molecules and a distance between the two pyrrole rings of neighbor molecules of $L = 1.54 \text{ nm}$ (Figure 5.10(a)), the STM simulation of C-C covalent bonds is characterized by a uniform STM contrast in the bond with a distance between the two neighboring pyrrole rings of $L = 1.32 \text{ nm}$ (Figure 5.10(b)). The better agreement between Figure 5.10(a) and (c), with one experimental distance of $L = 1.59 \pm 0.05 \text{ nm}$, allows us to assign the covalent single head-on interaction to a C-Cu-C organometallic bond.

In a final effort to shed light on the kinetics and thermodynamics of the processes, we performed DFT calculations for the relevant chemical species following two different reaction pathways: direct dechlorination (red lines) and Cu adatom-mediated

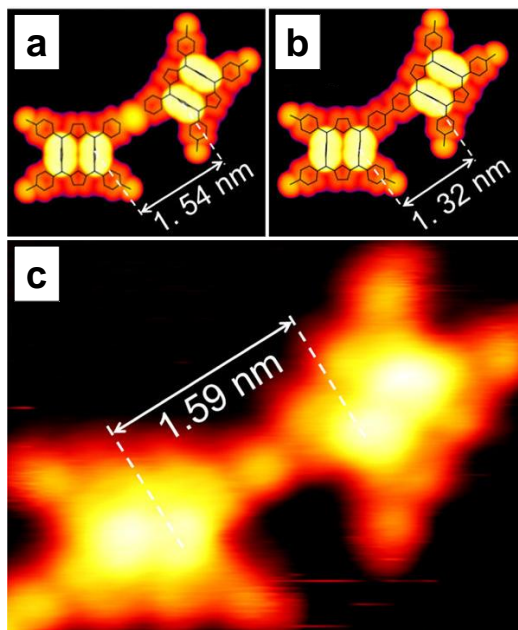


Figure 5.10: STM simulations and images of a covalent single head-on interaction for Cl₄TPP deposited on Cu(111). (a) C–Cu–C organometallic interaction and (b) C–C covalent bond between two Cl₃TPP molecules. (c) Experimental ($T = 400$ K for $t = 30$ minutes).

Ullmann coupling (blue lines), as shown in Figure 5.11. Here, we reference all energies to that of Cl₄TPP adsorbed on Cu(111) in the “inverted” conformation. The relative stability of “saddle” versus “inverted” conformations (Figure 5.11(i),(ii)) is highly sensitive to the choice of exchange and correlation (XC) functional. When vdW interactions are neglected (PBE solid lines in Figure 5.11), “inverted” and “saddle” conformations are isoenergetic, whereas, if vdW interactions are included at the Grimme’s D3 level (PBE-D3 dashed lines in Figure 5.11), the “inverted” conformation is 0.6 eV more stable than the “saddle” conformation, as expected. If instead, vdW interactions are included at the self-consistent level (vdW-DF2 dotted lines of Figure 5.11), we find opposite behavior. This suggests that PBE-D3 is the more robust XC functional for describing free-base TPP’s on metal surfaces. From here on, we shall refer specifically to PBE-D3 energy values.

To form a stable C–C covalent bond between molecules via the direct dechlorination path (Figure 5.11(a)), two isolated molecules (2Cl₄TPP) first find a slightly more stable configuration interacting via a single side-on Cl \cdots Cl interaction (Cl₄TPP)₂ (Figure 5.11(a),iii). Then, after overcoming an energy barrier of 0.9 eV, a Cl atom is cleaved from one molecule to form the complex Cl₄TPP \cdots Cl₃TPP (Figure 5.11(a),iv). Finally, after overcoming a similar barrier, the second Cl atom is also cleaved from the other molecule

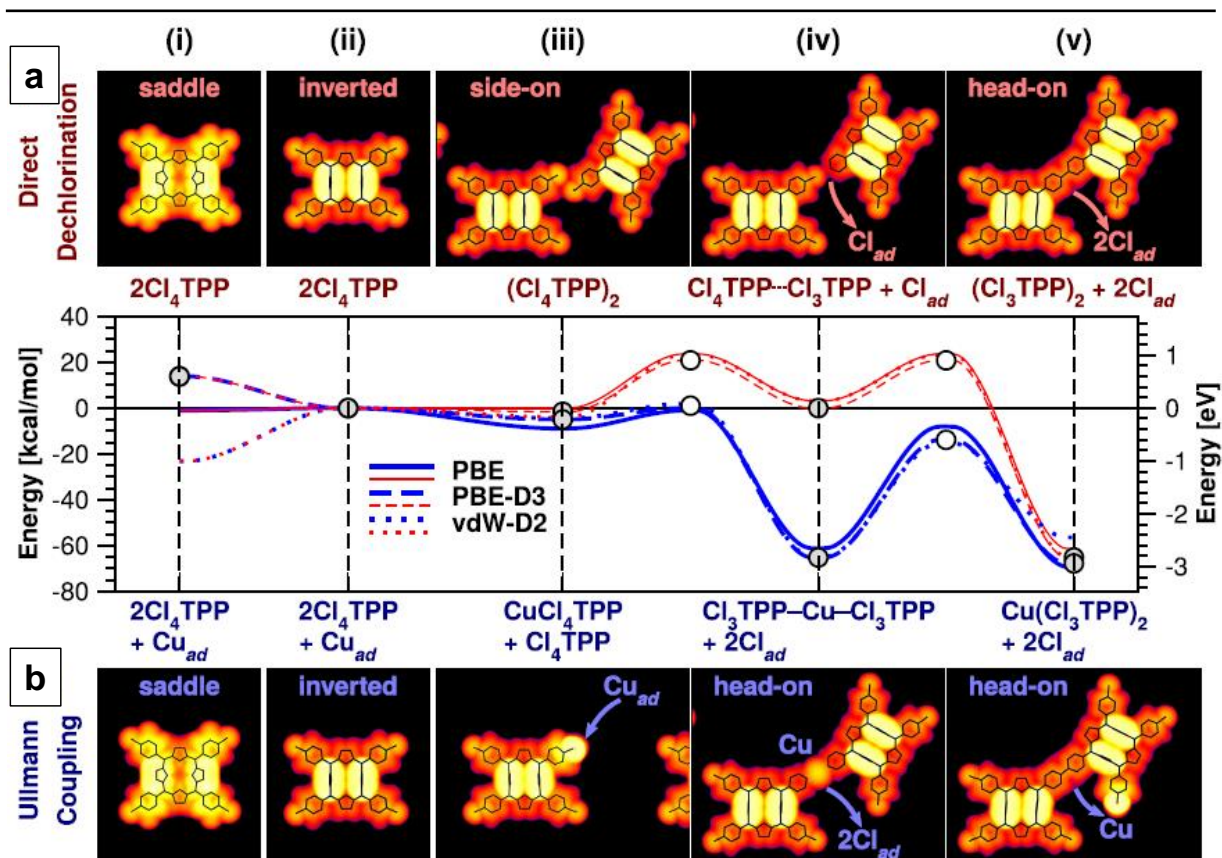


Figure 5.11: STM simulations and DFT reaction profile for the (a) direct dechlorination reaction (red lines) and (b) Cu adatom-mediated Ullmann coupling reaction (blue lines). For each process we plot the energy of the (i, ii) precursors, (iii, iv) intermediates, (v) and final species (gray circles) and two transition states (white circles) using Perdew-Burke-Ernzerhof (PBE)[141] (solid lines), PBE-D3 [142] (dashed lines), and vdW-DF2 (dotted lines) exchange and correlation (XC) functionals.

and the final C–C covalent bond is formed between molecules $(\text{Cl}_3\text{TPP})_2$ with a binding energy of 2.8 eV (Figure 5.11(a),v). This C–C covalent bond is the energetically most favorable structure in a direct dechlorination process. In contrast, the reaction pathway to form a stable C–C covalent bond via a Cu adatom mediated Ullmann coupling reaction is facile with no overall barrier (Figure 5.11(b)). In this case, one of the two isolated molecules first interacts with a Cu adatom (Figure 5.11(b), iii), spontaneously forming a dimer complex with a partially dissociated C–Cl bond ($\text{CuCl}_4\text{TPP} + \text{Cl}_4\text{TPP}$) and a binding energy of 0.2 eV. Both molecules are then dechlorinated with no overall activation barrier due to the stabilization brought about by the Cu adatom underneath the dissociating C–Cl bond. This results in the formation of a C–Cu–C organometallic bond with a binding energy of 2.9 eV ($\text{Cl}_3\text{TPP}-\text{Cu}-\text{Cl}_3\text{TPP}$) (Figure 5.11(b), iv).

These theoretical reaction pathways allow us to explain why some Cl₄TPP molecules on Cu(111) at RT show cleavage of Cl atoms, whereas after annealing at 400 K other molecules are still intact. In fact, even though the C–Cu–C organometallic bond is thermodynamically more stable than the adsorbed precursor molecules and the Ullmann reaction is barrierless, not all molecules reach this equilibrium state due to the limited availability of Cu adatoms on the surface, i.e., Cu adatoms act as a limiting reagent. In a direct dechlorination process, the most stable species is by far the C–C covalently bonded (Cl₃TPP)₂, whereas in a Cu adatom mediated Ullmann coupling reaction the C–Cu–C organometallic bond is isoenergetic with the C–C covalent bond between molecules. To understand why the organometallic species is strongly preferred over the final C–C product, under our experimental conditions, we must consider the heat dissipation to the Cu(111) surface, which is an excellent thermal conductor. The C–Cu–C intermediate features strong coupling to the Cu surface via its C–Cu_{ad} and N–Cu bonds. In this way, before the organometallic intermediates can be demetallated, a heat transfer to the substrate occurs that is sufficient to kinetically trap the organometallic species [143]. And then, when heating the sample over 450 K in order to overcome the barrier and achieve the C–C bond, we end up promoting the self-metalation and degradation of molecular species.

Finally, it is important to highlight that the behavior of Cl₄TPP on Cu(111) is a quite rich process that cannot be fully understood without considering the two reaction pathways described herein. Since the Cu mediated Ullmann coupling reaction is a facile and thermodynamically more stable process, the direct dechlorination process will only take place when no Cu adatoms are available. However, heating the Cu(111) surface naturally produces more adatoms, so that the Cu adatom mediated Ullmann process remains facile even under conditions where the barrier for direct dechlorination could be overcome. For this reason, we do not expect the direct dechlorination pathway to play a major role under ordinary conditions.

REMARKS

We have studied the surface, migration, conformation, and Ullmann coupling reaction profile for Cl_4TPP deposited on $\text{Cu}(111)$. We obtain significant surface migration and rotation barriers of 0.77 ± 0.09 and 0.93 ± 0.28 eV, respectively, indicative of covalent binding to the surface. Surprisingly, we find that all adsorbates exclusively ($\sim 100\%$) adopt a highly distorted molecular configuration where the pyrrole rings of the molecules are rotated $\sim 100^\circ$, the so-called “inverted” structure. Moreover, based on this conformation, we are able to unequivocally identify the bonding motifs: vdW single head-on and side-on $\text{Cl} \cdots \text{Cl}$ interactions, and $\text{Cu}-\text{Cl}$ species; and the product: the organometallic $\text{C}-\text{Cu}-\text{C}$ species, by our combined STM-DFT study. Finally, by simulating two different chemical reaction pathways, we have shown that a Cu adatom-mediated Ullmann coupling reaction is essentially barrierless, and the organometallic $\text{C}-\text{Cu}-\text{C}$ species is the final product of the reaction under mild conditions when heat dissipation to the $\text{Cu}(111)$ surface is taken into account. To summarize, we report (1) the first system to have chlorinated TPP molecules as building blocks for on-surface synthesis; (2) the first system to adsorb almost 100% in the inverted structure conformation; (3) the first system to remain exclusively in the “inverted” conformation throughout the Ullmann reaction pathway, (4) the first elucidation of the Ullmann coupling reaction profile for inverted porphyrins, and (5) the first measurements of surface mobility of an “inverted” porphyrin. Altogether, these results blaze the trail toward the production of precisely tailored 2D molecular assemblies via the controlled application of Cu adatoms to the molecular precursors.

5.3 Cl₄TPP on Ag(111)

In the next step of the study, and still using the same molecular precursor, we will test the on-surface behavior of Cl₄TPP on a crystal of the same symmetry, Ag (111). With a combined scanning tunneling microscopy (STM), density functional theory (DFT) and x-ray photoelectron spectroscopy (XPS) investigation, we study the adsorption behavior, supramolecular ordering, chemical and physical changes upon annealing of a 5,10,15,20-(tetra-4-chlorophenyl)porphyrin (Cl₄TPP) on the Ag(111) surface. The use of a less reactive substrate could prove essential for polymerization due to their higher diffusion and rotation mobility. In this way one may increase the proximity of precursors during dehalogenation, thereby increasing the probability of forming periodic frameworks, whether by organometallic intermediates or direct covalent C–C bonds. Previous studies of free-base porphyrins have considered adsorption on various substrates, especially on noble metals. Indeed, it is noteworthy that on Ag and Au crystallographic surfaces, free-base tetraphenylporphyrins present the well-known “saddle-shape” conformation. This is a characteristic of weak or intermediate substrate-molecule interactions [42, 47, 48, 144–146]. At RT, well ordered 2D assemblies grow preferentially along the $\langle 1\bar{1}0 \rangle$ directions, revealing the coexistence of two distinguishable *porous* and *zigzag* structures and lattice parameters. Our DFT calculations show Cl₄TPP adsorbs in the typical “saddle-shape” conformation on Ag(111), as shown in Figure 5.12, and that the co-existence of these two overlays is due to translations between nearly isoenergetic adsorption sites. Furthermore, to self polymerize the organic mesh via an on surface Ullmann-type coupling reaction, we performed an STM and XPS study of the system upon annealing, following the chemical and structural modifications above RT. Under these conditions, we obtain a highly compact 2D framework composed of dechlorinated molecules.

RESULTS AND DISCUSSION

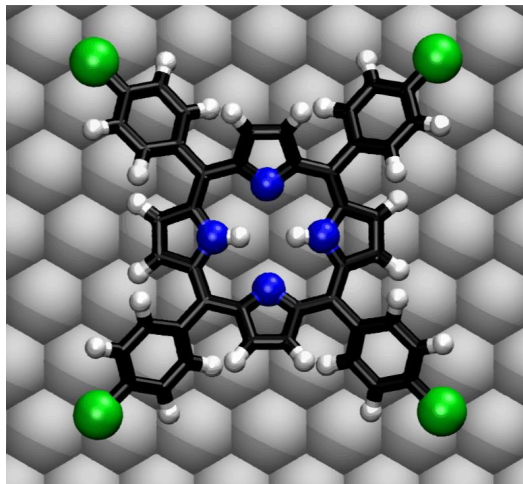


Figure 5.12: Top view of optimized Cl₄TPP adsorption in a “saddle-shape” configuration on Ag(111). Ag, C, H, N and Cl atoms are marked in silver, black, white, blue and green, respectively.

Figure 5.13(a) and (b) shows a STM image for Cl₄TPP on Ag(111) after deposition at RT for low and high surface coverage, respectively. It is worth noting that we consider herein both coverages, and in those cases, the results presented here were similar and are representative of the system. The lower molecule-substrate interaction gives the precursors high diffusion and rotation mobility so that they group together in energetically favorable sites like the step edges of the crystal surface. The 1 ML coverage shows extensive flat islands of 2D assemblies on the step plateaus. From this representative image, we can identify three distinct islands, marked as (1), (2) and (3), growing in different preferential directions. A careful analysis of several surface areas shows us that, in general, the islands extend preferentially in one of these three directions on the entire plateau (e.g. region (3)). Intersections between domains, such as (1) and (2), can be seen as “defects” which represent a small fraction of the surface area.

These well organized supramolecular assemblies, when analyzed at higher magnification, reveal the coexistence of two distinguishable overlayers with lattice parameters $\{a_1, a_2, \alpha\}$ and $\{b_1, b_2, \beta\}$, which we denote as *porous* and *zigzag*, respectively (see Figure 5.14(a), (b)). These two islands that grow in different preferential directions are shown in Figure 5.14(c) and (d) at high molecular resolution. The STM measurements provide us significant details of the molecular assembly. All molecules have their main axis passing through the pyrrole groups (see yellow dashed lines) parallel to one of the $\langle 1\bar{1}0 \rangle$ surface

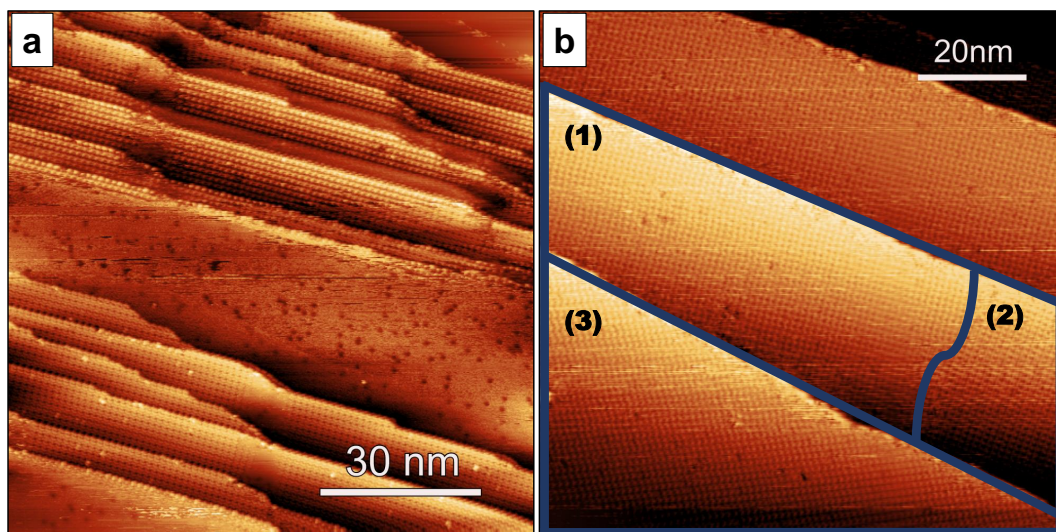


Figure 5.13: STM images of Cl₄TPP supramolecular assemblies on Ag(111) showing (a) low coverage at RT ($A = 100 \times 100 \text{ nm}^2$, $U = -1.06 \text{ V}$, $I = 0.12 \text{ nA}$) and (b) ML coverage showing large step plateau regions with areas (1), (2) and (3) having growth in three preferential directions ($A = 100 \times 100 \text{ nm}^2$, $U = 0.83 \text{ V}$, $I = 0.2 \text{ nA}$)

crystallographic directions. This suggests that the substrate is also playing a role in the formation of the supramolecular network, although the molecule-substrate interaction on Ag(111) is expected to be relatively weak when compared, for example, with Cu(111) [147]. The reactivity of the iminic nitrogens ($=\text{N}-$) with the Ag surface induces a minor rotation of the two correspondent pyrroles, resulting in the “saddle-shape” conformation (Figure 5.12), a well-known characteristic of porphyrin-based molecules physisorbed on Ag(111) [148]. The consequence of this “saddle-shape” conformation is clearly visible in the image contrast for the STM measurements of Figure 5.14(c) and (d) as compared with the STM simulation for isolated Cl₄TPP (see regions marked by red dotted lines).

The weak interaction of Cl₄TPP with the metallic substrate provides high mobility and consequently promotes dense self-assembled regions where intermolecular interactions dominate. The balance between molecule-molecule and molecule-substrate interactions basically determines the dimension of the overlayer lattice unit cells. To avoid extra-labeling in the figures, our notation is partially following the conventions in literature [149]. In this case, we have identified two sets of lattice parameters coexisting on the surface, $\{a_1 = 1.49 \pm 0.04 \text{ nm}, a_2 = 1.57 \pm 0.04 \text{ nm}, \alpha = 93 \pm 3^\circ\}$ and $\{b_1 = 1.49 \pm 0.04 \text{ nm}, b_2 = 1.55 \pm 0.05 \text{ nm}, \beta = 87 \pm 3^\circ\}$. These results are based on 281 sets of lattice parameters obtained from 27 different scanned regions. From our analysis, we find two lattices in

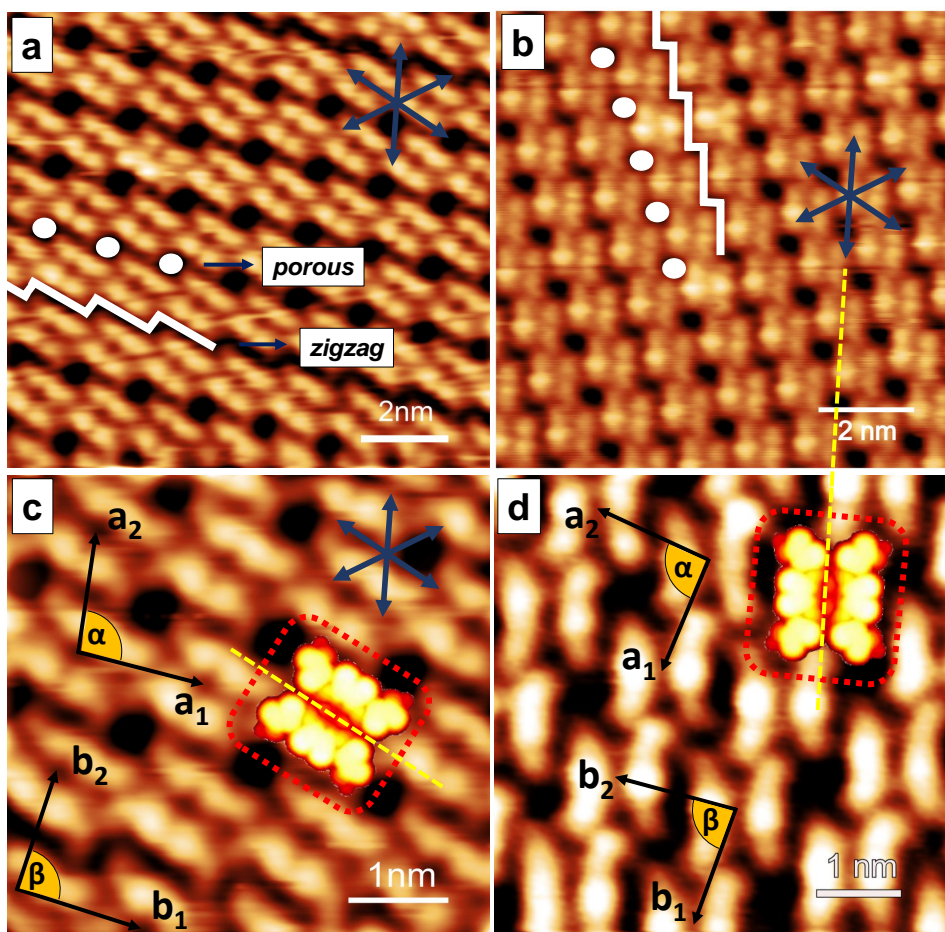


Figure 5.14: STM images of Cl_4TPP supramolecular assemblies on $\text{Ag}(111)$ showing regions with high magnification in which is possible to identify two super-lattice *porous* and *zigzag* overlayers ($A = 10 \times 10 \text{ nm}^2$, $U = 1.9 \text{ V}$, $I = 0.08 \text{ nA}$) for (a) and ($U = 1.3 \text{ V}$, $I = 0.1 \text{ nA}$) for (b). Lattice parameters for (c,d) *porous* ($a_1 = 1.49 \pm 0.04 \text{ nm}$, $a_2 = 1.57 \pm 0.04 \text{ nm}$, $\alpha = 93 \pm 3^\circ$) and *zigzag* ($b_1 = 1.49 \pm 0.04 \text{ nm}$, $b_2 = 1.55 \pm 0.05 \text{ nm}$, $\beta = 87 \pm 3^\circ$) overlayers ($A = 5 \times 5 \text{ nm}^2$, $U = 1.30 \text{ V}$, $I = 0.1 \text{ nA}$), with orientations parallel to pyrrolic nitrogens ($=\text{NH}-$) shown as yellow dashed lines in STM simulations for Cl_4TPP physisorbed on $\text{Ag}(111)$ (marked by red dotted lines). The blue arrows indicate the $\langle 1\bar{1}0 \rangle$ crystallographic directions of $\text{Ag}(111)$.

which eventually one row of molecules is slightly displaced from their adjacent adsorption sites. This results in the chlorophenyl groups either facing the center of their iminic pyrrole ($=\text{N}-$) (*porous*), or facing the correspondent chlorophenyl groups (*zigzag*) of their neighboring molecule. The co-existence of these two lattice networks suggests there are at least two adsorption sites that are nearly isoenergetic, so that they can be interchanged as function of time even at RT (see video in Figure 5.15(a)). The two minute video clearly shows a one-dimensional displacement of two molecular columns, so that all molecules simultaneously hop between neighboring adsorption sites. The ratio between *porous* and *zigzag* overlayers is 57:43.

At this point we can suggest some factors that may favor the coexistence of these two overlays. In addition to weak molecule-molecule and molecule-substrate interactions, potential factors include the dynamics of vacancies, adatoms on the terraces, steps and kinks acting as nucleation spots, and especially the coupling and decoupling dynamics of molecular precursors in the edge-regions of the island. At RT, the high frequency of these phenomena may favor the energetic translations of the supramolecular assembly, promoting the interchange between *porous* and *zigzag* configurations.

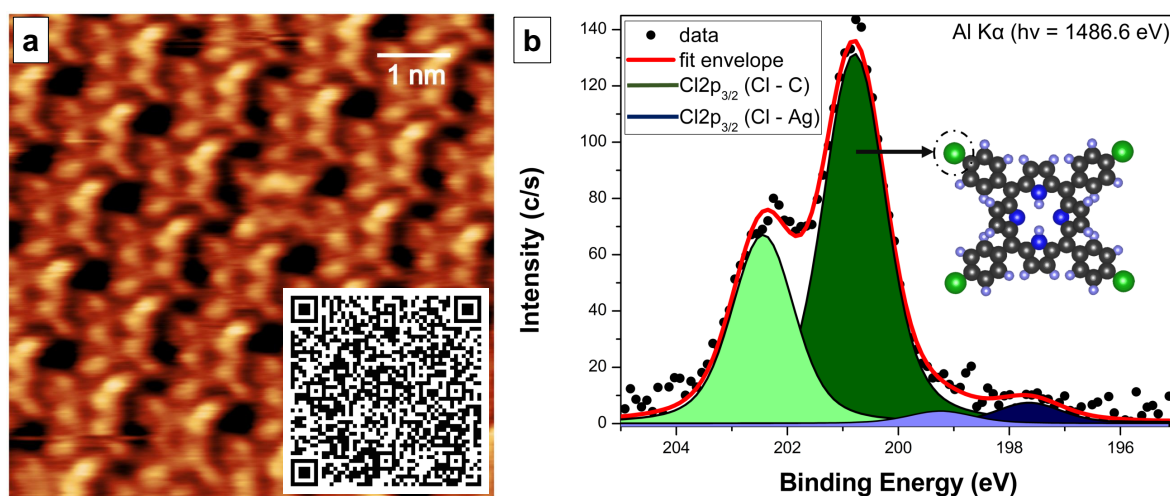


Figure 5.15: (a) High molecular resolution of a short video of the supramolecular lattice after deposition at RT. ($A = 7 \times 7 \text{ nm}^2$, $U = -1.10 \text{ V}$, $I = 0.13 \text{ nA}$). (b) Cl 2p XPS spectrum for a ML of Cl₄TPP deposited on Ag(111) at RT, decomposed into the doublet of the halogenated compound Cl 2p_{3/2} = 200.6 eV (dark green) and Cl 2p_{1/2} = 202.2 eV (light green) and the Cl–Ag doublet Cl 2p_{3/2} = 197.6 eV (dark blue) and Cl 2p_{1/2} = 199.2 eV (light blue).

Figure 5.15(b) shows the Cl 2p core-level spectrum for the sample as grown at RT. The XPS spectrum shows two components (green and blue). The dark green component of Cl 2p_{3/2} at 200.6 eV binding energy is consistent with C–Cl [147, 150]. A small shoulder in the spectroscopic signal at 197.6 eV (dark blue peak) indicates a minor amount of Cl–Ag [151]. Considering the integrated area of the Cl 2p peaks, we obtain a 6:94 ratio between inorganic and organic compounds, implying about 94% of the surface is covered by intact Cl₄TPP at RT. A very different behavior was found for the same molecule adsorbed on Cu(111) at RT, as shown in the previous section of this chapter, where about 40% of the precursors were dechlorinated at RT [147].

In order to better understand the molecule’s adsorption configuration on the surface, we have performed DFT calculations in the low coverage limit for intact Cl₄TPP on Ag(111). In agreement with our experiments, DFT predicts the most stable adsorption

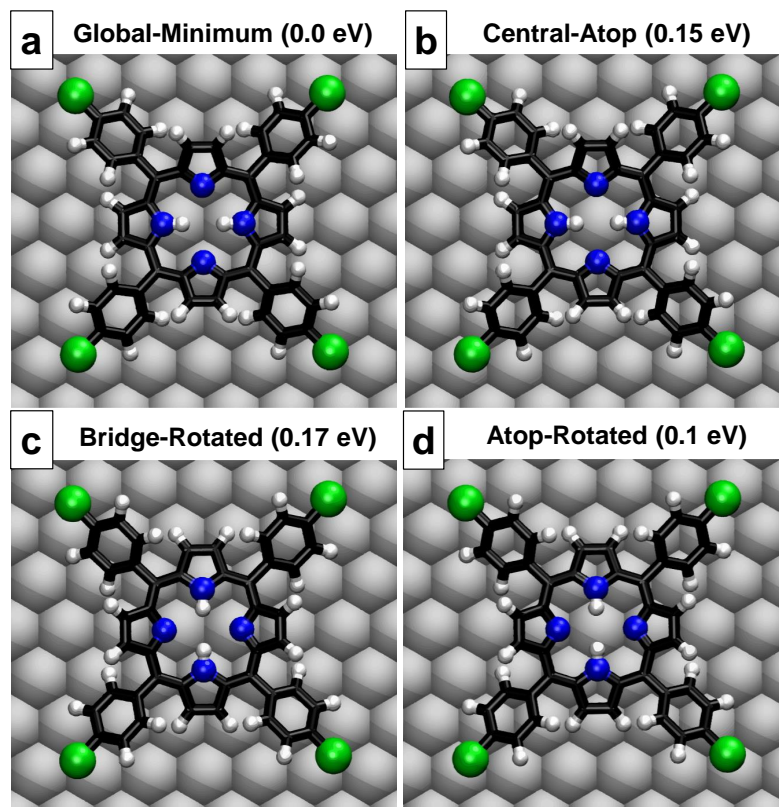


Figure 5.16: Schematics of CTPP optimal adsorption sites on Ag(111) and DFT calculated relative energies in eV for (a) Global-Minimum, (b) Central-Atop, (c) Bridge-Rotated and (d) Atop-rotated.

site has the two pyrrole ($-\text{NH}-$) groups aligned with the principal axis, and the two iminic ($=\text{N}-$) groups aligned with the perpendicular “long bridge” direction, as shown in Figure 5.16(a). We have named this most stable structure “Global-Minimum”. Calculations of individual porphyrins show that the four Cl terminations are found on bridge positions and the adsorbed molecule adopts a nearly square shape. More precisely, adsorbed Cl_4TPP is 0.36 \AA shorter along the principal direction ($d_{\text{Cl} \dots \text{Cl}} = 13.26 \text{ \AA}$) than the perpendicular direction ($d_{\text{Cl} \dots \text{Cl}} = 13.62 \text{ \AA}$). The mean height of the adsorbate above the Ag slab is 3.67 \AA , with the closest atoms to the top Ag layer being the 12 hydrogen atoms pointing downwards. Mean separations between the tilted pyrrole rings are 10.04 \AA between hydrogen atoms and 8.37 \AA between carbon atoms. The CP2K PBE-D3 adsorption binding energy for isolated Cl_4TPP on Ag(111) in the Global-Minimum is 3.53 eV , whereas neglecting vdW corrections the PBE interaction becomes repulsive by 0.58 eV . This demonstrates the fundamental role played by vdW interactions in determining the adsorption properties of physisorbed species.

We have also considered three other adsorption configurations: Bridge-Rotated, Central-Atop and Atop-Rotated, as shown in Figure 5.16(b), (c), and (d), respectively. The relative energies of these configurations compared to Global-Minimum are shown in Figure 5.16(a)-(d). Our GPAW PBE-D3 relative energies of 0.0, 0.32, 0.24, and 0.15 eV for Global-Minimum, Bridge-Rotated, Central-Atop, and Atop-Rotated, respectively, are consistent with our CP2K PBE-D3 values. The 0.1 eV energy difference between Global-Minimum and Atop-Rotated suggests, in principle, both conformations could coexist on the surface. Figure 5.17(a) is an overview of a particular region showing two rows with rotated molecules highlighted in white rectangles, alongside Figure 5.17(b), a detailed sequence in high STM molecular resolution. So, in contrast to our calculations, these regions appear in extremely rare situations and they are adsorbed on Bridge-Rotated or Atop-Rotated sites according to our definitions.

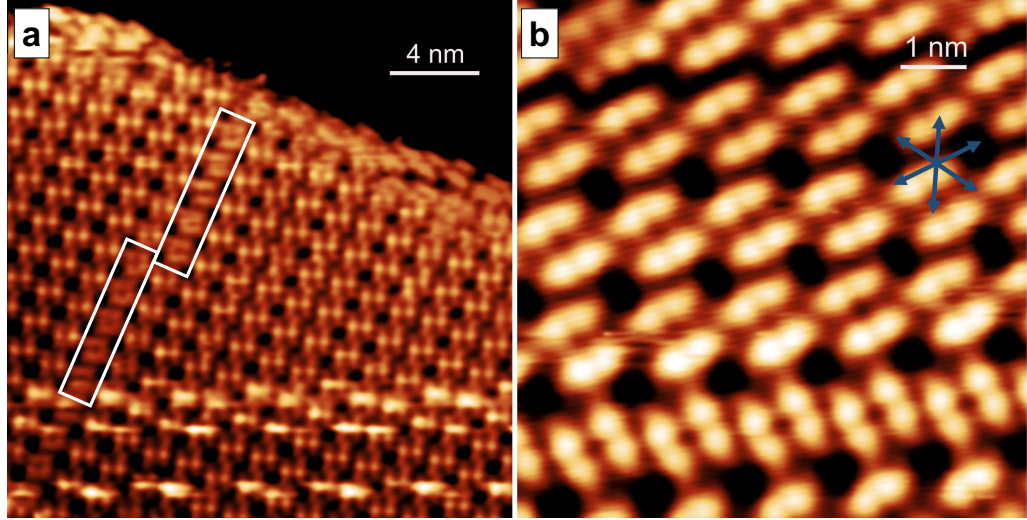


Figure 5.17: STM measurements for high coverage at RT with (a) sequences of rotated molecules marked by white rectangles ($A = 20 \times 20 \text{ nm}^2$, $U = -1.24 \text{ V}$, $I = 0.1 \text{ nA}$) and (b) a region containing a row of several rotated molecules on Bridge/Atop-Rotated adsorption sites ($A = 7 \times 7 \text{ nm}^2$, $U = -1.28 \text{ V}$, $I = 0.08 \text{ nA}$).

Using the Global-Minimum conformation as a starting point, we are able to build a periodic model for the intact overlayer with the unit cell vectors $\mathbf{a}_1^s = 5\mathbf{e}_1 + \mathbf{e}_2$ and $\mathbf{a}_2^s = -2\mathbf{e}_1 + 3\mathbf{e}_2$, where \mathbf{e}_1 is the nearest neighbor separation along the principal axis ($e_1 = 2.89 \text{ \AA}$), and \mathbf{e}_2 is the perpendicular nearest neighbor separation ($e_2 = 5.01 \text{ \AA}$) for the Ag(111) surface. The resulting overlayer unit cell lengths are $a_1^s = 1.53 \text{ nm}$ and $a_2^s = 1.61 \text{ nm}$, which are within the experimental error of our *porous* overlayer measurements of $a_1^e = 1.49 \pm 0.04 \text{ nm}$ and $a_2^e = 1.57 \pm 0.04 \text{ nm}$, respectively. The resulting angle of $\alpha^s = 92^\circ$ agrees with our measured value of $\alpha^s = 93 \pm 3^\circ$, and the computed angle between

\mathbf{a}_1^e and the principal axis of 19.1° agrees quantitatively with our measured value of $20 \pm 2^\circ$. A top view of the relaxed structure from our DFT calculations of the overlayer and its corresponding simulated STM image are given in Figure 5.18(a) and (b), respectively.

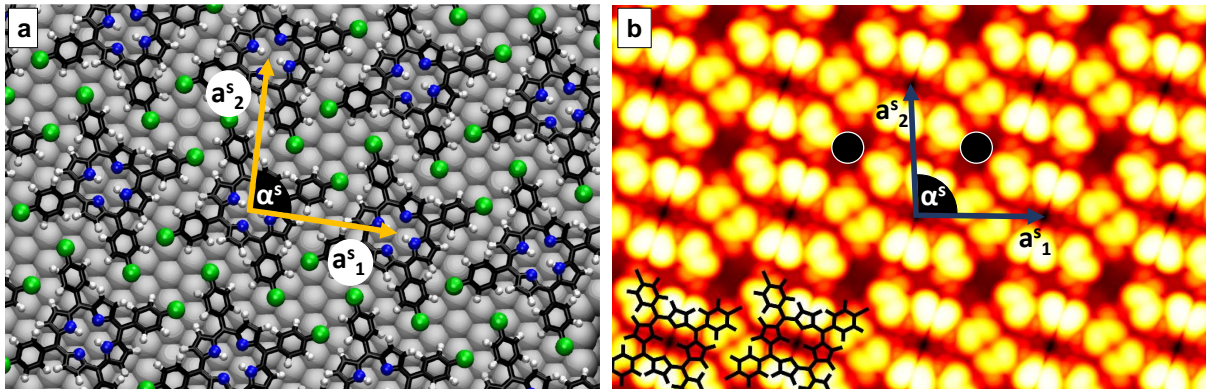


Figure 5.18: (a) *porous* network periodic model with calculated unit vectors $\{a_1^s = 1.53 \text{ nm}, a_2^s = 1.61 \text{ nm}, \alpha^s = 92^\circ\}$ and (b) STM simulation.

Taking into account these four configurations, Global-Minimum and Central-Atop are the most likely candidate adsorption sites for the formation of the *porous* and *zigzag* networks. Figure 5.19 shows the distances and angles on the respective adsorption sites that are closest to those obtained experimentally from our STM measurements. This model for the *zigzag* overlayer yields lattice parameters of $b_1^s = 1.53 \text{ nm}$, $b_2^s = 1.56 \text{ nm}$, and $\beta^s = 88^\circ$, in quantitative agreement with our measured parameters of $b_1^e = 1.49 \pm 0.04 \text{ nm}$, $b_2^e = 1.55 \pm 0.05 \text{ nm}$, and $\beta = 87 \pm 3^\circ$, respectively. Based on our theoretical models and experimental results, we find that the molecules are most probably adsorbed and shifting between Global-Minimum and Central-Atop sites which are coexisting on the surface (see video in Figure 5.15(a) for a dynamic overview).

The simultaneous hopping of a molecular column occurs preferentially along the $\langle 1\bar{1}0 \rangle$ crystallographic directions, parallel to the pyrrole groups of each porphyrin. A potential explanation is that the porous overlayer forms preferentially at low temperatures and at RT thermal fluctuations cause hopping from Global-Minimum to the nearest Central-Atop adsorption site leading to the *zigzag* structure. The reason why we do not observe Atop-Rotated despite its lower energy compared to Central-Atop is because the former needs a hop plus an additional 90° rotation step whereas the latter forms immediately after the hop. The Global-Minimum + Atop-Rotated overlayer is rarely observed (see Figure 5.17), as it is kinetically unfavored. The fact that all Cl_4TPP molecules jump

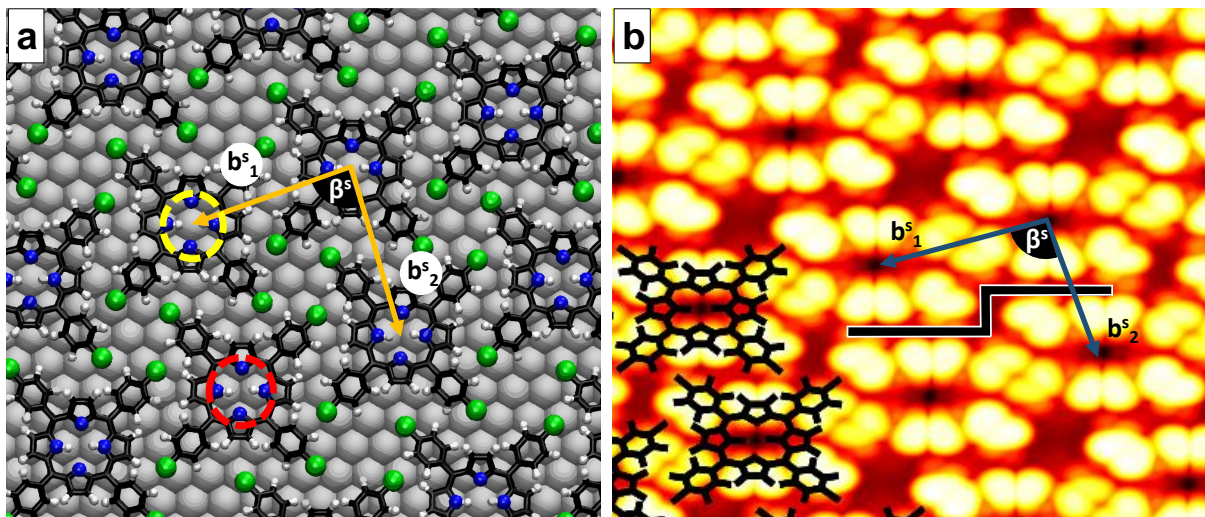


Figure 5.19: (a) Schematics of the *zigzag* $\{b_1^s = 1.53 \text{ nm}, b_2^s = 1.56 \text{ nm}, \beta^s = 88^\circ\}$ overlayers with DFT calculated adsorption sites most closely matching the experimental values. The quasi-isoeenergetic adsorption sites “Global-Minimum” and “Central-Atop” are indicated by the red and yellow dashed circles, respectively. (b) STM simulation with black bars indicating the characteristic *zigzag* pattern.

simultaneously leads us to assume that in the main axis direction, the intermolecular interaction is stronger than the lateral interaction (perpendicular to the main axis). We can also consider the supramolecular assembly as a rearrangement of 1-D chains packed and located at the Global-Minimum and Central-Atop sites and that the hopping rate probably follows an Arrhenius-like temperature dependence. For quantitative information, a detailed study in function of temperature would be necessary, however, due the lack of an appropriate experimental setup, i.e. cooled sample during deposition, this investigation was not possible during this thesis.

Another fundamental objective following layer deposition is to promote the covalent bonding between molecules in order to restructure the supramolecular assembly into a strongly bounded, compact and periodic 2D network. To achieve this, the cleavage of the molecular peripheral halogens is necessary and may be performed as suggested by Björk and co-workers [93]. Increasing the temperature promotes the formation of metallic adatoms on the surface and, consequently, increases the probability of catalytic reactions to promote chlorine cleavage. This drives the Ullmann coupling reaction, which results in strong carbon-carbon bonds. In this manner we have studied the structural and chemical behavior of the supramolecular assembly at temperatures above RT.

After annealing the sample to 350 K, there is no significant structural modification identified in STM. The assembly remains unchanged even after 90 minutes of

annealing. The Figure 5.20 shows terraces and steps with high coverage and the Cl_4TPP are virtually intact. In other words, both sets of lattice parameters **a** and **b** are still present over the entire covered surface, reproducing the *porous* and *zigzag* configurations, as shown in upper right in Figure 5.20(b). XPS also shows no evidence of chemical changes, suggesting there is no formation of a new structured 2D covalent network, as the Cl 2p peaks of the halogenated compound remains unchanged and dominant.

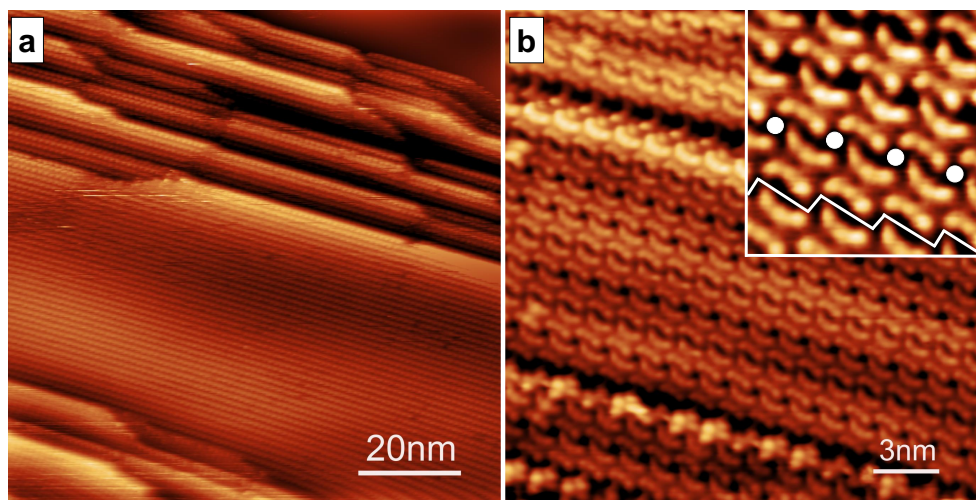


Figure 5.20: STM measurements after thermal heating at 350 K for 30 minutes. (a) ($A = 100 \times 100 \text{ nm}^2$, $U = 1.16 \text{ V}$, $I = 0.14 \text{ nA}$) and (b) steps and terraces covered by Cl_4TPP molecules ($A = 20 \times 20 \text{ nm}^2$, $U = -1.06 \text{ V}$, $I = 0.12 \text{ nA}$) with inset showing *zigzag* and *porous* regions ($A = 5 \times 5 \text{ nm}^2$)

At 400 K, we see a gradual molecular dechlorination with the annealing time. Homolytic cleavage is shown by the reduction of the halogenated compound signal at 200.6 eV binding energy followed by a concomitant increase of a new Cl–Ag $2p_{3/2}$ component at 197.6 eV, as shown in Figure 5.21(a). Based on this, we may conclude that these two chemical compounds coexist after 20 minutes of sample heating. At this time, the relative percentage of chlorine organic species is 27%, showing there is a high dechlorination rate at this temperature. Moreover, we note that after a long annealing time ($t \approx 150$ minutes), Cl 2p photoemission peak is completely suppressed. The evolution of each chemical species is shown in Figure 5.21(b) for the first 40 minutes of heating. For the halogenated compound, the integrated area of the Cl $2p_{3/2}$ doublet as a function of heating time indicates complete molecular dechlorination occurs after approximately 40 minutes at 400 K (see green curve in Figure 5.21(b)). During the same period, we are also able to follow the Cl migration from the molecule to the metallic surface during the first 20

minutes and complete suppression during the following 20 minutes, so that the sample is almost free of chlorine atoms (see blue curve in Figure 5.21(b)).

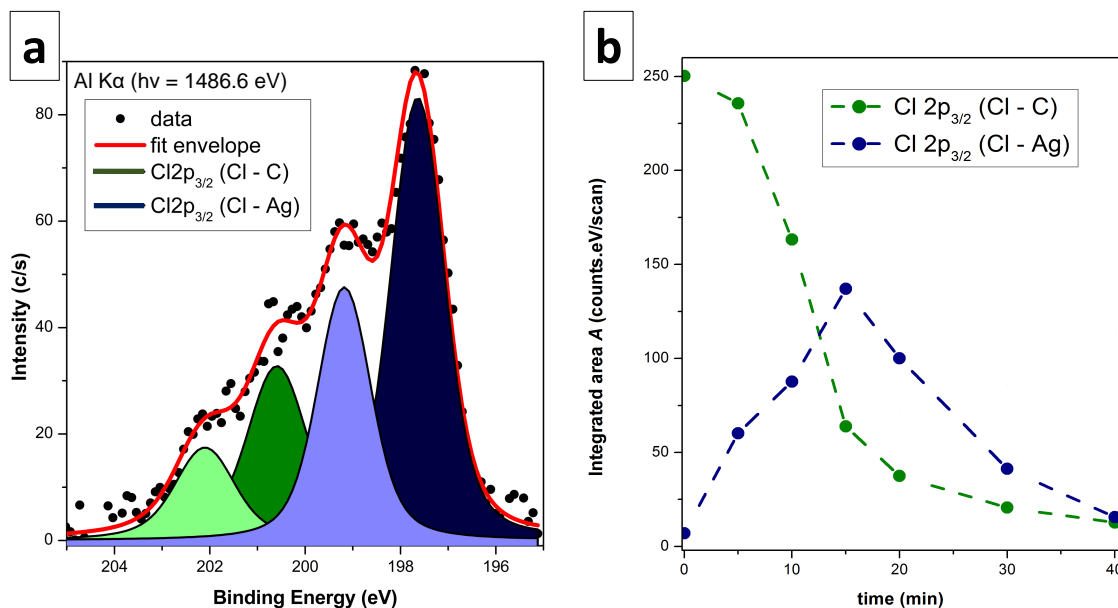


Figure 5.21: (a) Cl 2p XPS measurements ($t = 20$ min, $T = 400$ K) decomposed into the halogenated doublet (green) and Cl–Ag component (blue), (b) evolution of integrated areas for the Cl 2p_{3/2} components with time at $T = 400$ K of halogenated compounds (green curve) and Cl–Ag species (blue curve).

We can also state that, based on our STM images, Cl 2p, and C 1s XPS binding energies (see upper right inset in Figure 5.22(a)), species remain intact on the surface. In fact, the photoemission peak for C 1s shows no change in energy or integrated area at the end of this thermal treatment. STM reveals extensive covered areas with highly packed structures. The compact pattern is shown in Figure 5.22(b) with high magnification and the extracted lattice parameters are $c_1 = 1.24 \pm 0.06$ nm, $c_2 = 1.33 \pm 0.04$ nm and $\gamma = 89 \pm 3^\circ$, which we identify as a new molecular framework composed exclusively of dechlorinated precursors.

At this point we might want to consider different scenarios regarding the new molecular framework formed as well as the suppression of Cl from the photoemission signal after the long annealing procedure. The cleavage of Cl is the first step for the formation of covalent C–C bonds thought Ullmann coupling reaction. However, the typical 2D porous network with interconnections between the dechlorinated phenyls would typically produce a larger pore [8, 10], which is not the case here. There are other possible explanations to be explored. One of the first possibilities is indeed possible that no covalent coupling

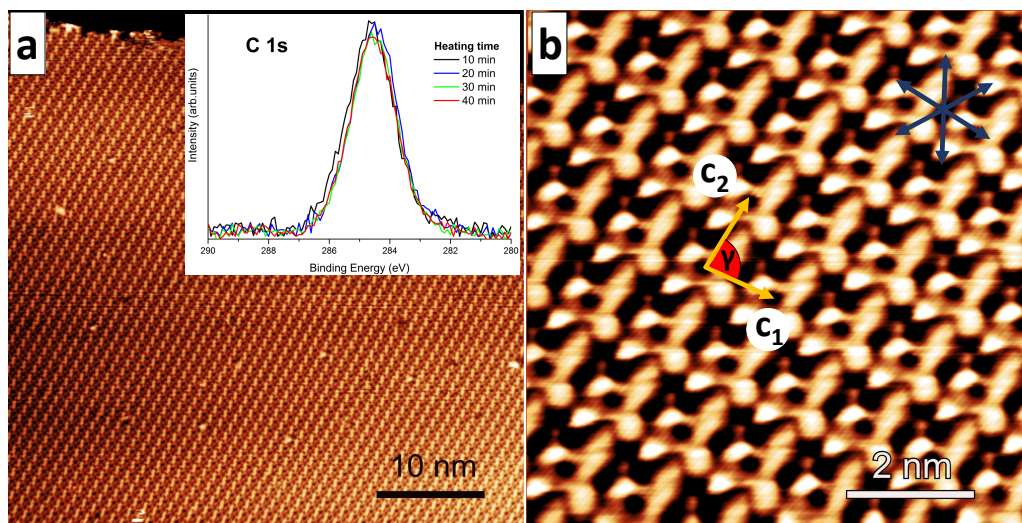


Figure 5.22: Thermally treated Cl_4TPP adsorbed on $\text{Ag}(111)$ (a) STM measurement ($t = 150$ min, $A = 50 \times 50 \text{ nm}^2$, $U = -1.13 \text{ V}$, $I = 0.15 \text{ nA}$), and the inset C 1s XPS spectrum showing the evolution at 400 K ($\text{BE} = 284.5 \text{ eV}$). (b) STM of the supramolecular assembly and lattice parameters $c_1 = 1.24 \pm 0.06 \text{ nm}$, $c_2 = 1.33 \pm 0.04 \text{ nm}$, $\gamma = 89 \pm 3^\circ$, ($A = 7 \times 7 \text{ nm}^2$, $U = -1.06 \text{ V}$, $I = 0.12 \text{ nA}$), with blue arrows indicating the $\langle 1\bar{1}0 \rangle$ crystallographic directions of $\text{Ag}(111)$.

happens and the dehalogenated molecules bind to the $\text{Ag}(111)$ substrate by bending the phenyl units towards the surface. A preliminary fully relaxed DFT calculation reveals a “dome-like” structure that does not resemble the observed STM images (see Figure 5.23). Another possibility could be dehydrogenation in the phenyl or pyrrole group closer to the dechlorinated phenyl unit, promoting a covalent bonding [152, 153]. Finally, during the long annealing procedure, hydrogen might have stabilized the dechlorinated precursor possibly forming a supramolecular ordering of 2H-TPP molecules as described previously in literature [48, 152]. Regarding Cl suppression in the XPS signal, Bowker and Waugh [154] used thermal desorption spectroscopy (TDS) to demonstrate that Cl does not desorb as Cl atoms from $\text{Ag}(111)$ but as AgCl , and complete desorption requires temperatures above 800 K. Thus in our case we have not reached such a high temperature to desorb AgCl . There is the simple possibility that Cl disappears from the surface region by diffusion into the bulk also described by Bowker and Waugh [154], making Cl not detectable by XPS. Finally we shall not exclude that simultaneous dehydrogenation occurs, which makes desorption of HCl possible during the long annealing time. Nevertheless, a definitive description of such possibilities would need further theoretical and experimental investigations.

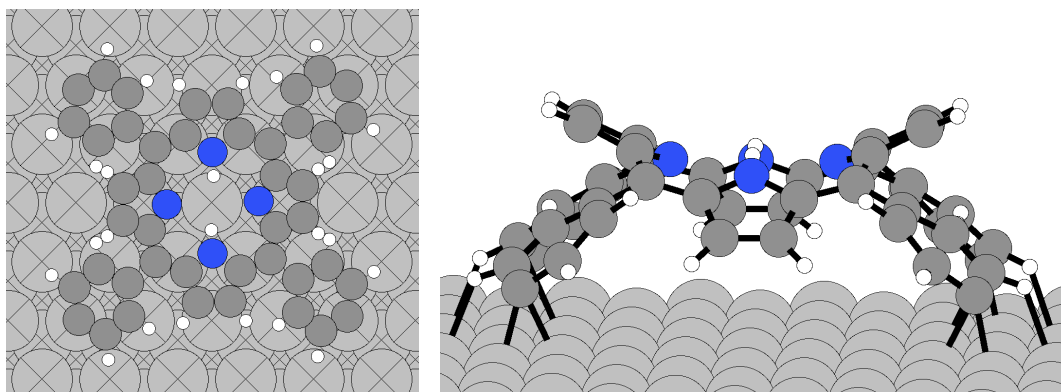


Figure 5.23: Top and side view of the DFT calculation of the relaxed “dome-like” structure considering a fully dechlorinated molecule on Ag(111).

REMARKS

DFT combined with STM also helped to identify transitions between adjacent molecular adsorption sites that lead to *porous* (Global-Minimum to Global-Minimum or Central-Atop to Central-Atop) or *zigzag* (Global-Minimum to Central-Atop) configurations. This provides a reliable model to understand the structure and growth mechanism of the 2D assemblies.

In an attempt to promote the formation of covalent bonds by a surface-assisted Ullmann-type coupling reaction, at temperatures above RT ($T \approx 400$ K) we obtain a new highly compact motif composed of completely dechlorinated molecules. However, it is still uncertain whether the constitute overlayer is covalently interconnected. Although we were unable to establish a reliable theoretical model for the 2D mesh, our results clearly indicate that Cl₄TPP on Ag(111) is a promising candidate system for building atomically precise functional porphyrinic frameworks.

5.4 Cl₄TPP on Gr/Ir(111)

The quasi-free-standing graphene on Ir(111) is an interesting template candidate for the sublimation of molecular precursors. The very weak molecule-substrate expected for this system will eventually favor the compact intermolecular assembly, possibly stabilized by side-on or head-on type I vdW interactions, as observed in section 4.2. Therefore it is an interesting template on self-assembly for porous network of free-base porphyrins. In this first part of the study, we performed an XPS and STM analysis for structural and chemical determination of the porous network obtained as function of temperature.

The graphene growth on metal surfaces by the CVD method is a well-known and widely applied technique. Through it, it is possible to synthesize MLs with few structural defects and a single azimuthal orientation over the entire extension of the surface. Moreover, graphene synthesized on certain metal surfaces has poor chemical interaction and the freestanding characteristics are almost ideal, which means that the astonishing chemical-physical properties of the 2D material are preserved (e.g. the Dirac cone). The sublimation of Cl₄TPP on graphene can be interesting both for the geometric aspect of self-assembly on the surface and for the possibilities of tuning the electronic properties of Gr. The rearrangement of molecules forming relatively large nanopore networks can also be an interesting guide allowing a periodical adsorption of other reactive elements, for instance, and consequently induce the bandgap opening of the graphene's Dirac cone [155–159]. In particular, hydrogen has also been shown to strongly modify the electronic properties of the material, inducing metal-insulating transitions [160].

So, inspired by the study of Balog et. al [156], we evaporate hydrogen atoms over a nanoporous network of Cl₄TPP on Gr/Ir(111) in order to use the molecular network as a mask for periodic deposition and thus control the length of the gap opening. The pore dimensions, according to our predicted model (see Figure 5.24), are wide enough to allow the patterned hydrogen deposition. The measurement of the electronic band structure was performed before and after adsorption using angle-resolved photoemission spectroscopy (ARPES). The work was carried out on the PGM beamline of the Brazilian National Synchrotron Light Laboratory (LNLS).

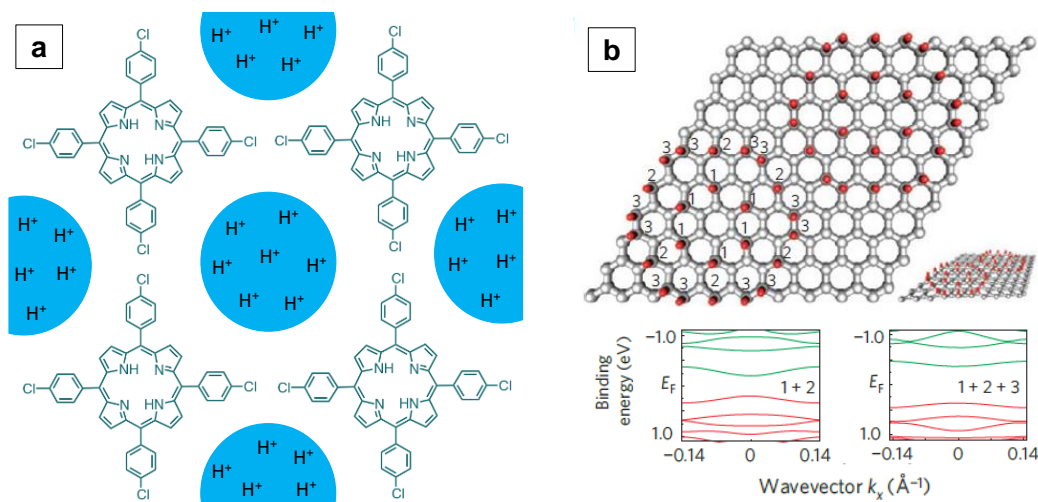


Figure 5.24: (a) Proposed model for supramolecular Cl₄TPP network used as an atomic hydrogen deposition mask. (b) Calculation for band structures and bandgap opening as a function of hydrogen adsorbates concentration. Adapted from the reference [156].

RESULTS AND DISCUSSION

The growth of Gr/Ir(111) by the CVD method was performed according to the procedure described in section 3.3.3 and the surface quality and Moiré pattern of the superstructure were checked using LEED and STM. Figure 5.25(a) shows that, by means of STM, it is possible to identify a hexagonal pattern with network parameters ~ 25 Å, highlighted in yellow dashed lines. The pattern is a result of the incommensurability of the Gr and Ir(111) networks, so that the chemical interaction is variable across the entire surface, resulting in a slight corrugation of approximately 0.3 Å of amplitude. These corrugations are clearly visible in the profile of Figure 4.10(b). Previous studies show that on the extension of the Gr/Ir(111) Moiré lattice, the interaction between network and substrate presents three basic adsorption structures (or sites): fcc, hcp and atop [161–163]. Figure 5.25(a) indicates a representative region of the sample, in which we identified a uniform Moiré pattern over the entire surface extension, including the interface regions of the Ir(111) steps, which strongly suggests that our sample has single oriented graphene layers. The LEED in Figure 5.25(b) shows the hexagonal diffraction pattern characteristic of Ir(111) (see white point indicated) in the same way that a series of satellite spots arranged with a small hexagonal symmetry (marked in yellow), characteristic of the Gr superstructure, can also be observed. The crystallographic directions of the Ir(111) surface are indicated in white in Figure 5.25(a), while the directions of the Moiré network

are indicated in blue. We can observe the parallel orientation between $\langle 1\bar{1}0 \rangle$ and $\langle 11\bar{2}0 \rangle$, which is well-known as a Gr network called $R0^\circ$ [164–166].

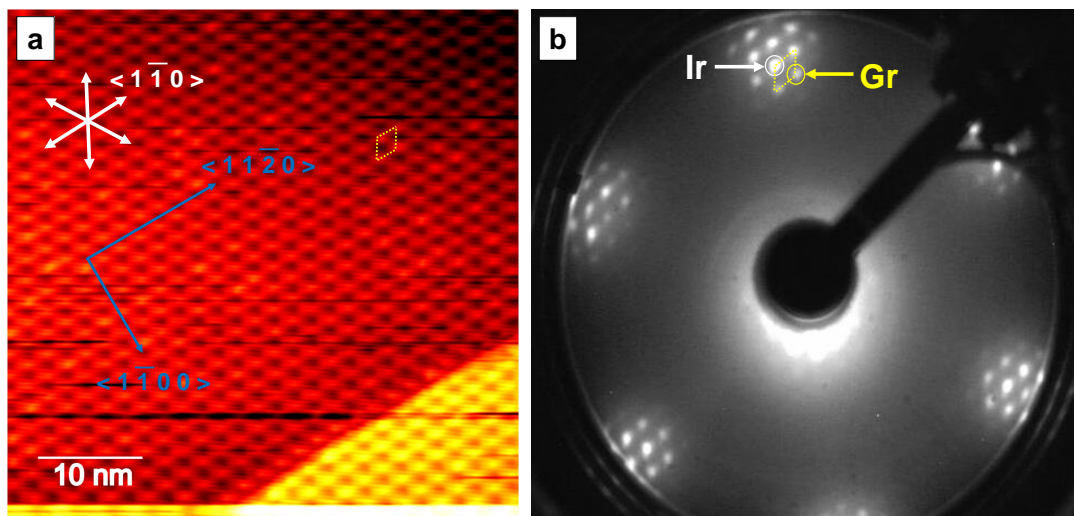


Figure 5.25: $R0^\circ$ Graphene on Ir(111) (a) STM image of Gr/Ir(111) exhibiting an Moiré pattern. The Ir(111) crystallographic directions is indicated by white arrows and the main directions of the graphene Moiré pattern is indicated by blue arrows. $A = (50 \times 50) \text{ nm}^2$. Tunneling parameters: $U = 1.03 \text{ V}$, $I = 0.12 \text{ nA}$. (b) LEED diffraction pattern ($E = 70 \text{ eV}$).

Now with a perfectly ordered template, we have the ideal conditions for the self-assembly of the nanoporous network. After sublimation of Cl_4TPP at RT, the molecules could be imaged by STM even for submonolayer coverage (see Figure 5.26(a)). The binding capacity between adjacent Cl_4TPP reveals a relatively strong intermolecular stability and this result suggest that the chlorophenyl rings promote the stabilization of the molecular layer, most likely by side-on interactions. In this model, the interactions are non-covalent type I vdW, as previously reported in the Cl_4TPP on Cu(111) section.

Figure 5.26(b) shows a complete covered area (ML) which it is possible to identify the square pattern of the molecular network; the unit cell is indicated in dashed white square and the parameters were determined $a_1 = a_2 = 1.56 \pm 0.05 \text{ nm}$ and angle $\theta = 90 \pm 1^\circ$. When compared with the dimensions of the molecules in its gas phase ($a = 1.34 \text{ nm}$ and $b = 1.55 \text{ nm}$) we can infer that the obtained network has a compact arrangement with only one molecule per unit cell. The carpet-like supramolecular network extends uniformly throughout the region, establishing continuity even on step edges. The supramolecular network, contrary to what was observed for some phthalocyanine molecules, does not follow a specific direction of the Moiré network.

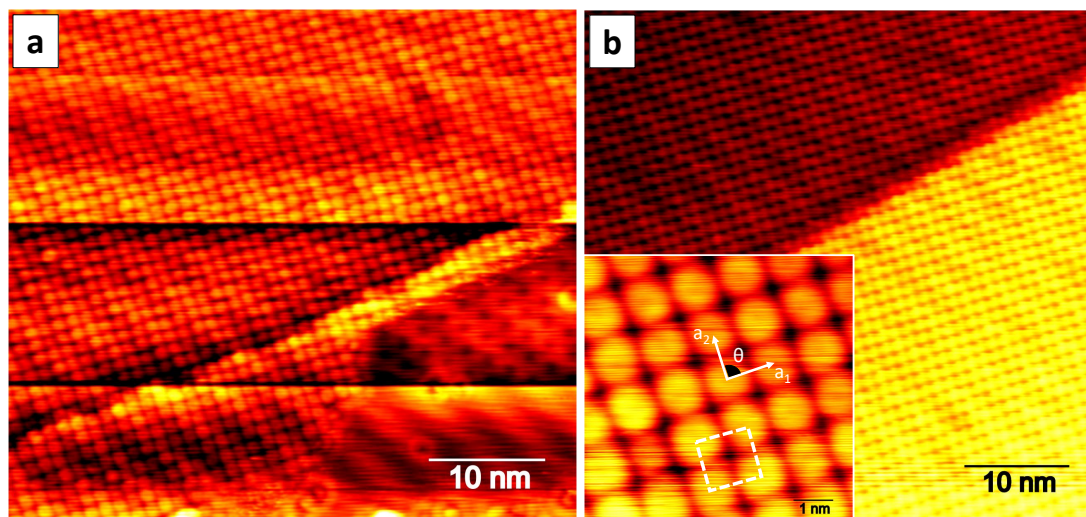


Figure 5.26: STM image of Cl_4TPP on Gr/Ir(111) (a) Submonolayer coverage after Cl_4TPP sublimation at RT. $A = (50 \times 50) \text{ nm}^2$. (b) ML coverage with an inset at higher magnification of the supramolecular network. Unit vector parameters: $a_1 = a_2 = (1.56 \pm 0.05) \text{ nm}$ and $\theta = (90 \pm 1)^\circ$. Squared symmetry marked by white dashed lines. $A = (50 \times 50) \text{ nm}^2$. Tunneling parameters: $U = -2.98 \text{ V}$, $I = 0.13 \text{ nA}$.

To extract chemical information from the surface environment, we performed high-resolution XPS measurements (HR-XPS) at the PGM Beamline in the Brazilian Synchrotron Light Laboratory (LNLS). Figure 5.27 indicates the photoemission peaks relevant to the study. Due to the high resolution of the beamline, the Ir 4f peaks present bulk and surface states, as shown in Figure 5.27(a). The data have been fitted using Doniach-Sunjić peaks of widths $\Gamma = 0.2$ and asymmetry parameter $\alpha = 0.12$. For Ir 4f_{7/2}, the bulk peak (blue) is centered at 60.9 eV and the surface state (dashed blue) at 60.3 eV, values in great agreement with the literature [158, 163, 167, 168]. Resembling graphene, the supramolecular network Cl_4TPP does not interfere in the bulk or surface state binding energy of Ir. This indicates that both Gr and the molecules are electronically decoupled from the surface, that is, the chemical interaction Gr + Cl_4TPP on Ir(111) is basically negligible.

Figure 5.27(b) shows the Cl 2p spectrum regarding the chlorine atoms attached to the molecules at 200.5 and 202.2 eV ($\Delta = 1.6 \text{ eV}$) for the spin-orbit components Cl 2p_{3/2} and Cl 2p_{1/2}, respectively. These values are also in excellent agreement with the literature for chlorobenzene [140, 147, 169]. The data were fitted using two Doniach-Sunjić functions with width $\Gamma = 0.3$ and asymmetric parameter $\alpha = 0.04$ after linear background removal. It is important to highlight the fact that the spontaneous dechlorination of chlorinated TPP species deposited at RT has been reported previously [147, 169], due to

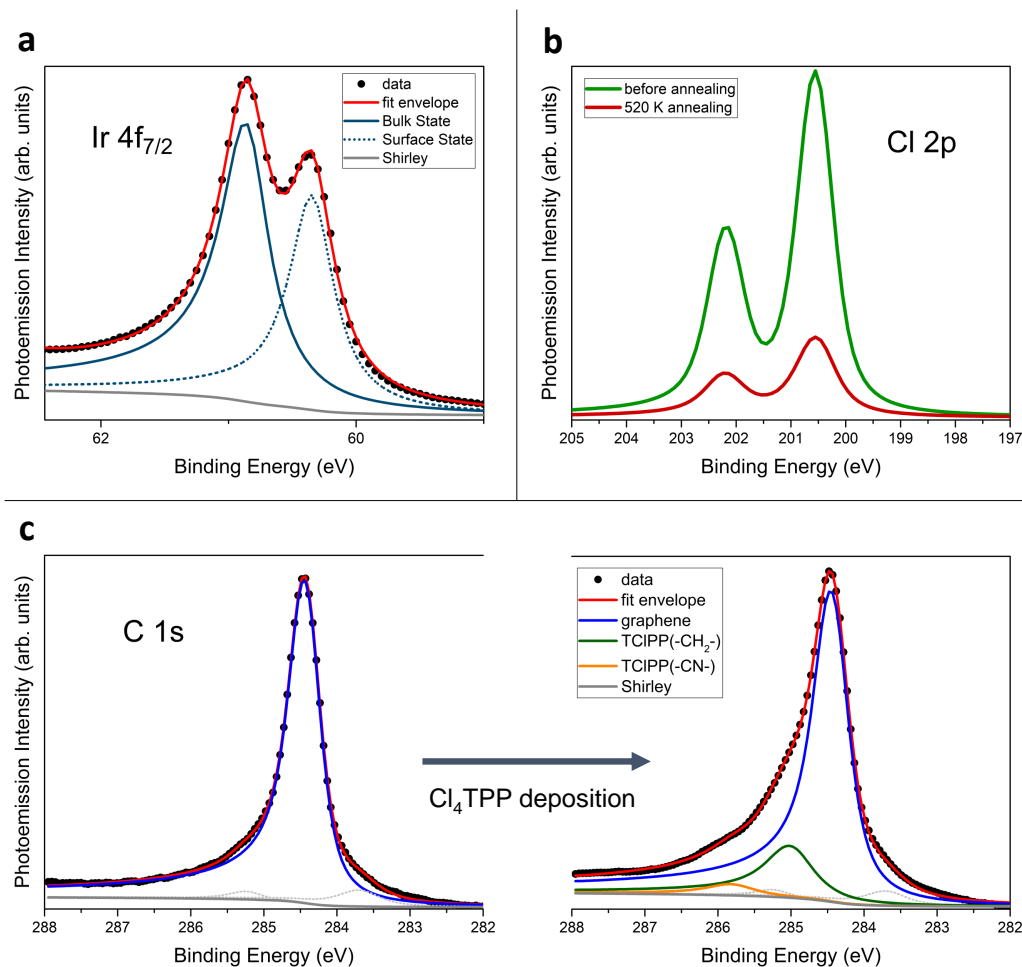


Figure 5.27: HR-XPS spectra for a Cl₄TPP ML on Gr/Ir(111). (a) Ir 4f_{7/2} spectrum featuring the bulk and surface state peaks at 60.9 and 60.3 eV, respectively. (b) Cl 2p spectrum showing the spin-orbit components before and after 520 K sample annealing. (c) C 1s spectrum before and after Cl₄TPP deposition. Graphene peak at 284.4 eV (blue component); 284.7 eV (green component); and 285.2 eV (yellow component). Beamline excitation energy for all photoemission spectra: $h\nu = 400$ eV. See fitting details in text.

the reactivity of the molecules with the substrates. However, in our case, we can assert that the graphene sheet is an excellent protector that prevents the chlorine cleavage in contact with the reactive surface. In the same Figure, we see two photoemission peaks, green for immediately after the molecules evaporation and red after 520 K sample annealing. The intensity decay of the peak after the heat treatment is a strong indication that there was desorption of molecules during the procedure. In addition, the constant value of binding energy during the whole process shows that the chlorine atoms remained attached to the molecule until the moment of complete surface desorption at ~ 600 K, in another words, we do not see the formation of IrCl compounds.

A careful analysis of the C 1s region was performed as well. The left part of Figure 5.27(c) indicates the C 1s photoemission signal for the Gr/Ir(111) clean surface at 284.4 eV, characteristic binding energy in accordance with values reported in the literature [163]. The spectra were fitted by a Doniach-Sunjić function with width $\Gamma = 0.15$ eV and asymmetry constant $\alpha = 0.12$. After deposition of Cl₄TPP, two new small shoulders arise at 284.7 and 285.2 eV; the green and yellow peaks on the right part of Figure 5.27(c). These small signals represent the carbon atoms attached with the Cl₄TPP molecules forming the supramolecular network. It's a small signal compared to the graphene peak, but duly proportional since we have approximately 0.18 carbon/Å² in the molecular mesh versus ~ 0.95 carbon/Å² in the graphene sheet. In fact, experimentally, we have an integrated peak area ratio of $\sim 0.2 A_{Cmol}/A_{Cgr}$. The evolution of the C1s spectrum upon annealing is not shown here but is characterized by the vanish of the small shoulder until the complete molecular desorption at ~ 600 K.

Figure 5.28 shows a region of the surface after mild annealing at approximately 590 K. In this case, the inaccurate determination of the annealing temperature was determined by a thermal pyrometer that does not have great precision. The annealing process has regrouped the molecular network into several domains orientations. It is plausible to assert that the heating was relevant to the breakdown of the previously highly ordered and uniform network and that there is really no preferential growth direction for the molecular mesh. Cl₄TPP species, therefore, have high surface mobility and intermolecular interactions are predominant in the system, reaffirming the hypothesis of molecular stabilization via non-covalent type I vdW bond.

In the next step of the study, with the intention of using the nanoporous network as a template for the evaporation of reactive elements, we used a commercial hydrogen cracker to subject the sample to an atomic flow of H for up to 600 s. After the procedure, the electronic properties of graphene were monitored by ARPES and XPS. At this stage, it is important to highlight that considerable modifications in Gr electronic properties are expected when “bare” graphene (without protection) is exposed to atomic hydrogen. Previous ARPES studies show that a bandgap opening of ~ 450 meV and XPS photoemission C 1s peaks show a shift and considerable changes in the overall shape [155–159, 170]. Figure 5.29 shows the ARPES spectrum of a Gr/Ir (111) sample covered by one ML of Cl₄TPP before and after exposure to atomic hydrogen for 600 seconds.

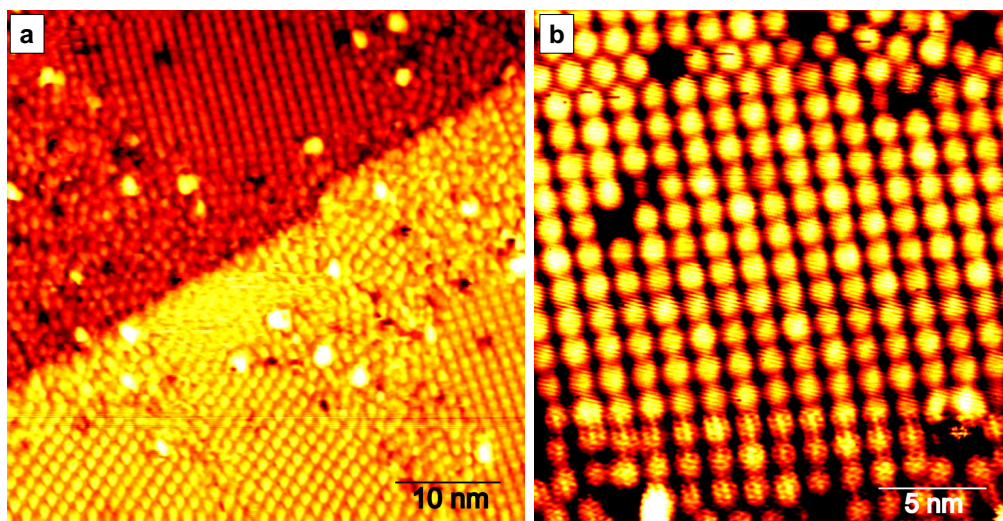


Figure 5.28: STM image of Cl₄TPP on Gr/Ir(111) after mild annealing at 590 K. (a) Several domains after the supramolecular regrouping and (b) a high magnification STM image showing the network squarish pattern.

By comparing the ARPES measurements, none modification in the linear dispersion of the π and π^* bands, as well as a bandgap opening is observed in the vicinity of the Dirac point. In particular, a careful observation ~ 1.25 eV below E_f unveils a minigap which is characterized by a decrease in the photoemission intensity and a slight shift in the graphene π band. This kind of minigap has been attributed to the Moiré pattern of Gr/Ir(111) [161]. Moreover, comparing the Cl1s XPS spectra before and after the hydrogen exposure, neither a shift nor spectral shape modifications of the spectrum is observed. Additional measurements of the Cl 2p component suggest the molecules remain intact (no dechlorination is observed). These observations are indicative of an unaffected graphene layer neither by plausible hydrogen intercalation nor by doping due to the molecular layer or contamination with unwanted chlorine atoms dissociated from the molecules. These results show that a film of Cl₄TPP does not affect the pristine properties of Gr/Ir(111) and helps to protect it against modifications by atomic hydrogen.

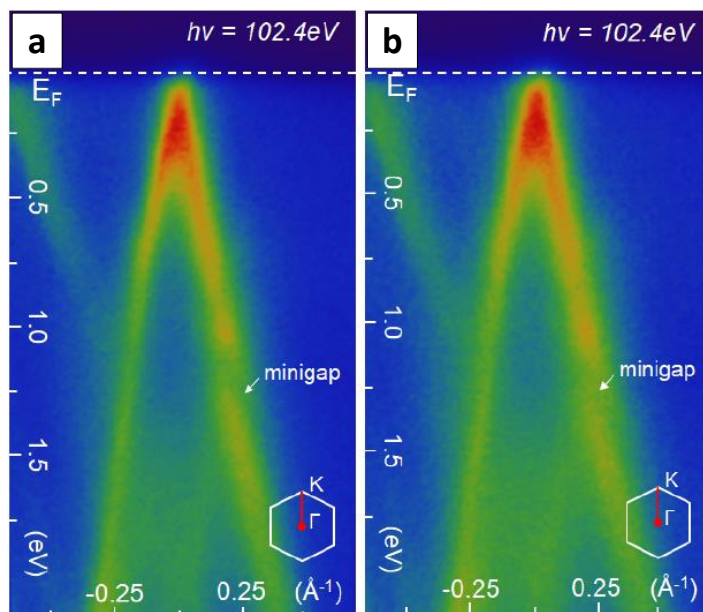


Figure 5.29: Angle resolved photoemission spectra of graphene on Ir(111) covered with a ML of Cl₄TPP molecules acquired with photon energy of 102.4 eV and a sample temperature of 60 K. (a) Cl₄TPP on Gr/Ir(111) before and (b) after 600 seconds of exposition to atomic hydrogen (H⁺).

REMARKS

In summary, our results show that the molecular self-assembly in a compact square network keeping continuity over the step-edges of the substrate. The network stability is maintained by type I vdW bonds and the molecular layer was shown to not affect the pristine properties of Gr/Ir(111). In particular, doping from the molecular layer has not been observed. Remarkably, a ML film of Cl₄TPP effectively protects graphene against unwanted modifications by atomic hydrogen.

5.5 2H-TCNPP on Cu(111) with co-adsorbed metal atoms

Cyano-functionalized porphyrins are frequently used in molecular self-assembly since the charge distribution of the cyano ligands induces the formation of an intrinsic dipole, which promotes intermolecular coupling, e.g. via hydrogen bonding or robust metal-ligand interactions. As demonstrated recently, [43, 47] the relative strong interaction of the iminic nitrogens (in the center of the macrocycle) of 2H-TCNPP to specific sites on the Cu(111) surface leads to a “inverted structure” conformation [43, 47, 80, 147]. Thus, the high reactivity between complex and surface is an important and promising factor for the formation of intermediate organometallic structures similar to the Ullmann coupling reaction. Starting with this motivation, we studied the specific influence of temperature and coadsorbed reactive atoms on the behavior of 2H-tetrakis(*p*-cyano)phenylporphyrin (2H-TCNPP) on Cu(111) using scanning tunneling microscopy.

Upon co-deposition of Fe and Co, the molecules form 1D-linear chains after mild annealing on Cu(111) driven by the interaction of its cyano groups with metal adatoms forming organometallic CN:M:CN (M=Cu, Fe, or Co) bonds which are stable even up to 400 K. Moreover, motivated by the high chemical affinity between Pd and H, we also co-deposited the metal on the system, which leads to a drastic modification promoting a transition to 1D molecular chains to 2D nanoporous upon annealing. More importantly, Pd atoms also promoted the formation of a new specie (new motif) with new shape and new chemical structure that was catalytic produced on surface with the assistance of Pd. In this regard, the present strategy shows a new mechanism to form MOFs on surface that involves a catalytic agent plus precursors with reactive functional groups (CN).

RESULTS AND DISCUSSION

After preparation of the Cu(111) substrate the surface quality was verified by STM and XPS. Figure 5.30(a) depicts an STM image of 2H-TCNPP evaporated on Cu(111) at room temperature (RT). As previously reported, [43, 47] 2H-TCNPP molecules are imaged by STM as four bright protrusions at the periphery, associated with the phenyl groups which are oriented almost parallel to the surface. The two bright protrusions at the center of the molecules are ascribed to the pyrrole rings with their iminic nitrogen atoms pointing down to the surface, effectively establishing an angle of about 99° with surface plane in the inverted structure configuration. STM images of larger surface areas corroborate that 2H-TCNPP adopts exclusively this conformation oriented along the three main crystallographic directions $\langle 1\bar{1}0 \rangle$ of Cu(111) surface. After mild annealing at 350K, the 2H-TCNPP are organized into organometallic wires intermediated by Cu adatoms, as shown in Figure 5.30(b). In the upper right corner of the image, it is shown the distance between molecules in the CN:Cu:CN bond of $19.5 \pm 0.5 \text{ \AA}$ which is in very good agreement with previous results in the literature [47].

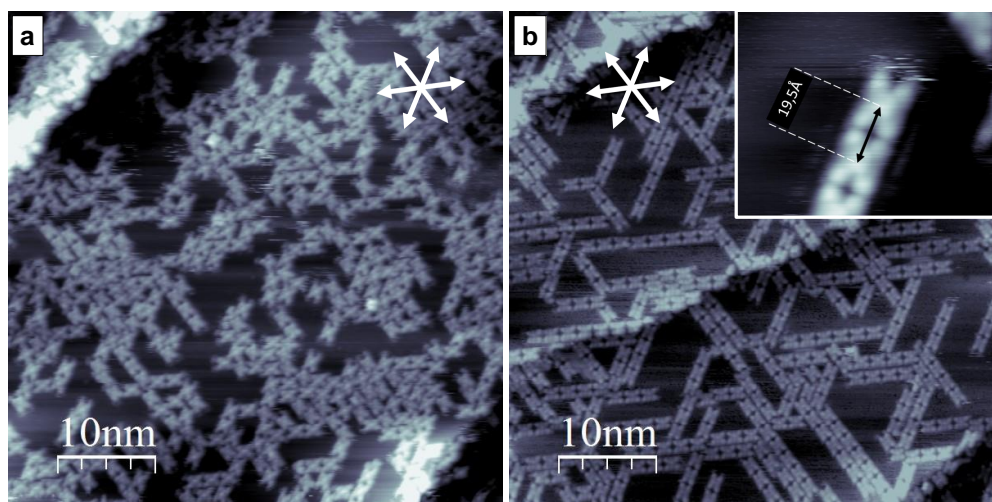


Figure 5.30: STM images of 2H-TCNPP deposited on Cu(111) as grown and after mild annealing. (a) Representative image of the system immediately after 2H-TCNPP sublimation at RT ($50 \times 50 \text{ nm}^2$, $U = -1.4 \text{ V}$, $I = 0.23 \text{ nA}$). (b) After 350 K annealing: molecular chains growing in the $\langle 1\bar{1}0 \rangle$ surface directions ($A = 50 \times 50 \text{ nm}^2$, $U = -1.4 \text{ V}$, $I = 0.11 \text{ nA}$).

Fe/Co + 2H-TCNPP on Cu(111)

In this section, we will deal with both cases of Fe and Co co-deposition since we observed identical results for these metals. Then, starting from a new fresh sample, we evaporate a submonolayer coverage at RT. After a post-deposition of Fe atoms (< 0.01 ML), some molecules are imaged with brighter appearance (see white rectangles in Figure 5.31(a)). As previously reported in Cl₄TPP on Cu(111), these molecules showing a this particular different motif (“saddle-shape”) can be associated to metalated species, i.e. Fe-TCNPP. Such a type of metalation have been also reported for other porphyrins [48, 130, 171]. The number of metalated species are approximately proportional to the amount of Fe deposited as demonstrated by subsequent Fe-depositions and can be easily distinguished from the non-metalated ones by their distinct appearance in STM (see inset of Figure 5.31(a)) with molecular resolution. 2H-TCNPP on Cu(111) exhibits a rectangular shape due the inverted structure conformation with the two central bright protrusions separated by 4.2 ± 0.4 Å. Contrary, the metalated species appear almost with a square shape with the two central bright protrusions separated by 7.4 ± 0.3 Å. They always adsorb in a configuration that is perpendicular to the non-metalated ones, in excellent agreement with the saddle shape model described previously [43]. At this stage, it is important to mention that when the deposition of Fe atoms was realized before the porphyrin deposition a similar behaviour is found, but the metalated species are only rarely observed. For higher iron coverages (~ 0.2 ML), Fe islands grow in a 3D mode which hinders the measurements of 2H-TCNPP adsorbed onto the islands. Upon annealing, the molecules form 1D chains by metal CN-coordination as already obtained on clean Cu(111) [47] and showed in Figure 5.30(b). Last but not least, in Figure 5.31(b) it is possible to observe few Fe clusters in high resolution. Remarkably, we can observe the Fe or Cu adatoms in between the peripheral cyano groups establishing the CN-coordination between the porphyrins. In the case where Fe was deposited, some of the protrusions linking the molecules look brighter and more clear when compared with the clean Cu(111) experiments [47]. Thus we believe the brighter links highlighted in Figure 5.31(b) could be Fe atoms. Notwithstanding, only with the present data and without a spectroscopic study, it is not possible to undoubtedly distinguished Fe from Cu as CN-coordination link.

Similar experiments were performed using Co and qualitatively the same behaviour was observed. These particular experiments involving Co on 2H-TCNPP/Cu(111)

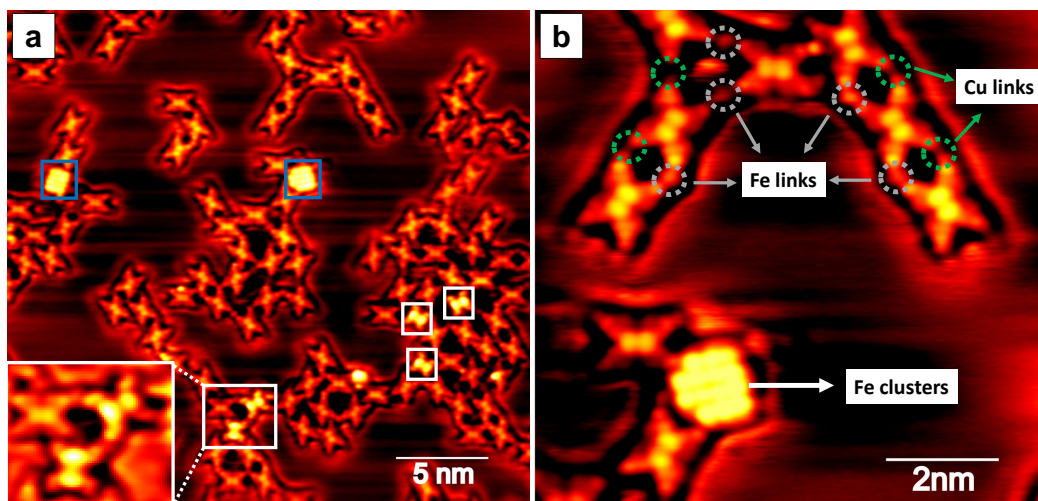


Figure 5.31: (a) Representative $(25 \times 25) \text{ nm}^2$ STM image of 2H-TCNPP on Cu(111) at RT and after post-deposition of Fe adatoms showing the Fe nanocluster (blue rectangle) and few metalated species (white rectangles) and inset at bottom left ($U = -1.44 \text{ V}$ and $I = 0.17 \text{ nA}$). (b) High-resolution image showing metal-coordinated 2H-TCNPP. In the down left side, a clear Fe nanocluster is displayed. We speculate the brighter protrusions are Fe links while the almost non-visible protrusions could be Cu links ($A = 11 \times 11 \text{ nm}^2$, $U = -1.44 \text{ V}$, $I = 0.18 \text{ nA}$).

were done in Erlangen in the group of Dr. Hubertus Marbach, associated to the Physical-Chemistry Chair leaded by Prof. Hans-Peter Steinrück, in the framework of the PRO-BRAL (CAPES-DAAD) collaboration. Thus, in contrast to others systems reported in literature [172, 173] neither Fe or Co have been able to change the adsorption behaviour or the molecular coordination on Cu(111), despite the fact that both individual adatoms are highly mobile on Cu(111). This behavior indicates that, while the availability of reactive adatoms is mandatory for the CN-coordination of the 2H-TCNPP, metal-ligand coordination is also governed by the molecular mobility. As the latter is very low at RT, only upon annealing to around 350 K the molecules have enough energy to efficiently overcome the diffusion barriers (translational and rotational) to form 1D chains. The length of 1D chains mainly depends on 2H-TCNPP coverage and annealing time. Annealing for long times at temperatures above 400 K leads to the rupture of the 1D chains and porphyrin Cu-metalation is induced to a certain extent [80].

Pd + 2H-TCNPP on Cu(111)

As mentioned before, Pd is a promising candidate to affect and change the adsorption behaviour of 2H-TCNPP on Cu(111). In our approach, two experiments were performed; (I): adsorption of 2H-TCNPP on Pd islands on Cu(111), and (II) adsorption of 2H-TCNPP on Cu(111) followed by Pd deposition. In both cases, the systems were studied at RT and upon moderate heating. After the deposition of ~ 0.3 ML of Pd at RT, single atom thick Pd islands are observed growing from the substrate step edges. The procedure is described in section 3.3.3 and the STM image that illustrates the Pd/Cu(111) systems is shown in Figure 4.11. After sublimation, the molecules adsorbed on the pristine Pd-free Cu(111) regions are aligned with the main crystallographic directions as described previously [47] (see inset on Figure 5.32(a)) and are adopting the inverted structure configuration. Figure 5.32(b) depicts a zoom in on adsorbed porphyrins on a Pd island. Strikingly onto the Pd islands the porphyrins do not exhibit any apparent order. At RT, most of the molecules on the islands also exhibit the typical appearance for the inverted structure as indicated with the white rectangle. However, some molecules show an appearance that is typically associated with the saddle shape (white dashed circle), which might be attributed to porphyrin metalation. This conformation is more frequently observed in the type II experiment where Pd is evaporated onto the pre-adsorbed 2H-TCNPP molecules on Cu(111). As we know, the metalated molecules are very mobile on the surface unless they are trapped on the surface, by other inverted molecules, or linked by adatoms, very similar to the Fe/Co + 2H-TCNPP case described in the previous section as depicted in Figure 5.31(a). At RT and only on top of the Pd islands, one rarely observes molecules which exhibit a very peculiar appearance; see blue dashed circle in Figure 5.32(b). We have named this particular motif as “clover shape”, characterized by four bright oval protrusions at the corners of the molecule.

After annealing to 350 K further differences between the molecules on the Pd-free Cu(111) regions and on the Pd islands are observed. On one hand, the molecules on Cu(111) are modified in such a way that they are mostly arranged in molecular chains as shown in Figure 5.33(a), related to the metal-coordination (CN:Cu:CN) described before [47]. On the other hand, the molecules on top of Pd islands remain randomly distributed, but more “clover shape” motifs are evident in the STM images (see Figure 5.33(b)). Remarkably, this “clover shape” is not observed for the molecules on the pristine Cu(111).

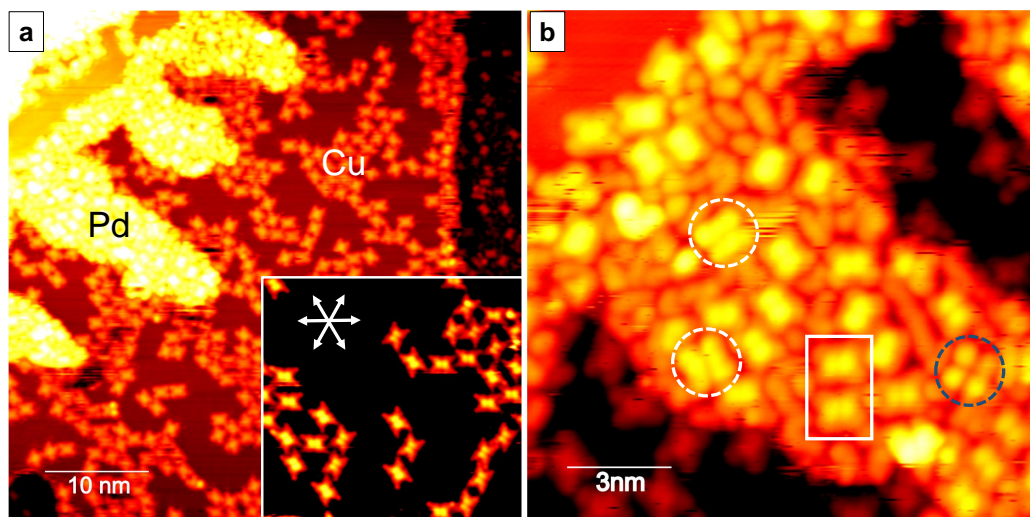


Figure 5.32: (a) Representative STM image (50×50) nm² of 2H-TCNPP on Cu(111) terraces and Pd islands. Inset with a high-resolution image (10×10) nm² showing that the molecules on Cu(111) always adopt the inverted structure conformations. (b) Zoomed in image (15×15) nm² of a Pd island displaying three different molecular motifs (inverted structure: white rectangles; saddle shape structure: white dashed circles; clover shape structure: blue dashed circles). Tunneling parameters: $U = 1.44$ V, $I = 0.12$ nA.

It is very important to note that most of the “clover shape” motifs on Pd islands show four bright protrusions, although examining carefully, it is also possible to find motifs with one, two and three protrusions, as highlighted by blue circles in Figure 5.33(b). This finding is an important evidence that “clover shape” conformation is related to an activation process that might be related to: (1) a chemical/structural change occurring at the periphery of the molecules basically affecting the phenyl+CN group without drastic changes in the inner part of the molecule; (2) chemical changes to the macrocycle, as for example, dehydrogenation with a strong conformational change; (3) Pd-metalation of the free-base porphyrin. These possibilities will be addressed in more detail below.

As the next step, the sample was carefully investigated as a function of the annealing time at 400 K. Figure 5.34 depicts the situation after 10 min at 400 K. Interestingly, almost all molecules on the Pd islands are in the “clover shape” conformation. On the Pd-free Cu(111) regions, the molecular chains formed by inverted structure molecules are still observed, but a significant number of molecules now also display the “clover shape” conformation. These molecules are, apparently, in transition process from Pd islands to Cu surface. The inset of the Figure 5.34(c), the white circle highlights a molecule still connected to the 1D chain in a conformation somewhat in between the inverted structure and

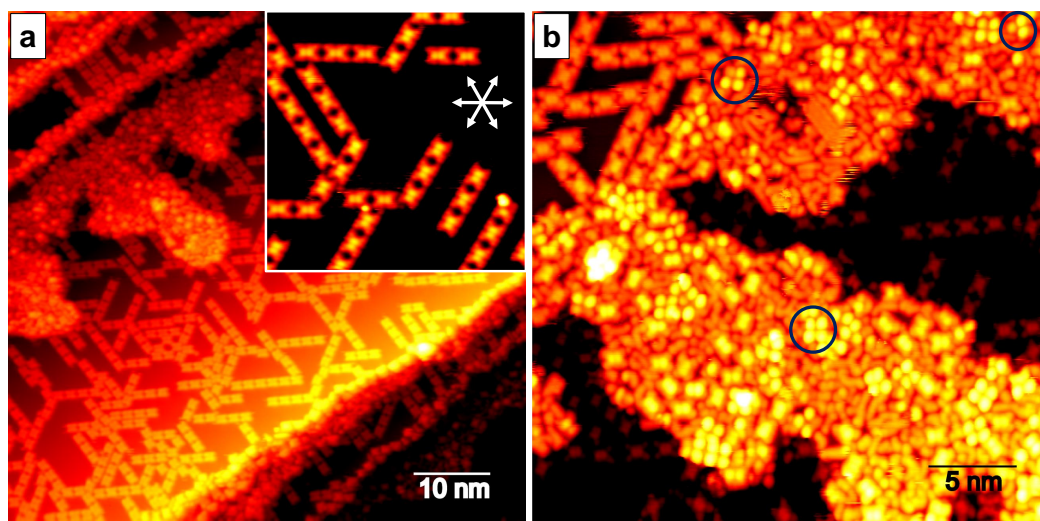


Figure 5.33: (a) Representative STM image (60×60) nm² of 2H-TCNPP on Pd/Cu(111) after annealing to 350 K for 10 minutes. Inset shows molecular chains exclusively on Cu(111) surface. (b) Pd islands (30×30) nm² in detail showing adsorbed “clover shape” structures with different motifs. $U = -1.44$ V and $I = 0.12$ nA.

the clover shape, suggesting the existence of intermediate states. Actually, these results and comparison with previous works strongly indicate that the observed modification in the molecular appearance is different from a porphyrin Cu- or Pd-metalation process. Lepper *et al.* [80] demonstrated that the porphyrin metalation process for 2H-TCNPP on Cu(111) rarely occurs even at 400 K, due the presence of the four cyano groups. Also, it was demonstrated that Cu-metalated species are very mobile, that is, too mobile to be imaged as individual molecules at RT. In contrast, in the presence of Pd, the clover shape motifs have a much lower mobility and thus can be imaged individually. Clover shape motifs are not arranged in molecular chains, which indicates that the lone pair in the CN group is probably coordinated, for instance, with Cu in the substrate or even Pd adatoms. Remarkably, in few regions, 2D supramolecular structures are observed exclusively formed by the clover shape motifs indicated by the blue circles in Figure 5.34(a)-(c); these 2D frameworks were never observed for equivalent experiments on clean Cu(111) [80]. Evidencing Pd plays an important role for the molecular self-assembly.

A longer annealing time (30 min) at 400 K increases the number of clover shape molecules. Several regions with larger 2D supramolecular ordered structures are observed over the whole sample, as displayed in Figure 5.35(a) and (b). After 60 min at 400 K, basically all molecules are converted to the clover shape motif on Cu(111) and,

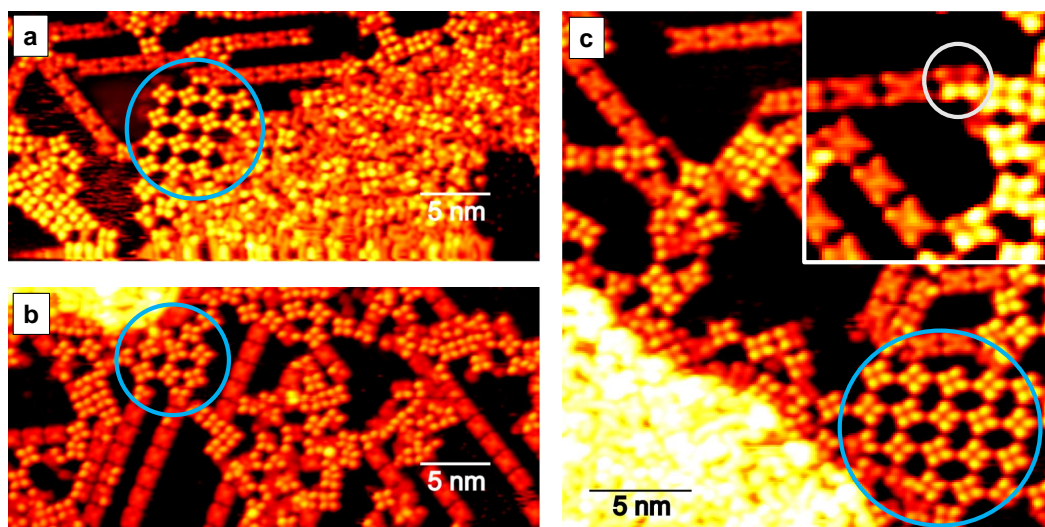


Figure 5.34: Representative STM images of 2H-TCNPP on Pd/Cu(111) after annealing at 400 K for 10 minutes. 2D mesh formed by “clover shape” molecules in the periphery of Pd islands (marked by blue circles). Inset in (c) shows a detail of molecules in an intermediate state. Tunneling parameters: $U = -1.44$ V and $I = 0.13$ nA.

consequently, almost all 1D chains are broken (Figure 5.35(c)), but the 2D arrangements remains intact. Such results demonstrate that co-adsorbed Pd plays an important role in the transition from inverted structure to clover shape motifs, probably due its catalytic properties. A detailed study on the ratio of clover shape motif relative to inverted one as a function of temperature is depicted in Figure 5.35(d).

The quantitative analysis shows the evolution of clover shape molecules as a function of the annealing time at 400 K on the Cu(111) terraces and the Pd islands. After 60 min of annealing at 350 K, there are no clover shape species on Cu(111), while approximately 45% of the molecules on the Pd islands have already clover shape. This configuration is denoted as $t = 0$ min in the graph of Figure 5.35(d). Basically, all the molecules on Pd islands are converted into the clover shape after 10 min of annealing at 400 K. Sixty minutes at 400 K leads to the conversion of the majority of the molecules to the clover shape in both regions. Therefore, subsurface co-adsorbed (or alloyed) Pd atoms controls the change from inverted structure to clover shape. From the present study, it is not possible to conclude if some of the clover shape molecules diffuse from the Pd islands or if they were also produced in the “Pd-free” regions of the Cu(111). Since the clover shape does not appear (for temperatures below 400 K) in the clean Cu(111) surface [47, 80], the most reasonable explanation is they have been either formed in the Pd islands

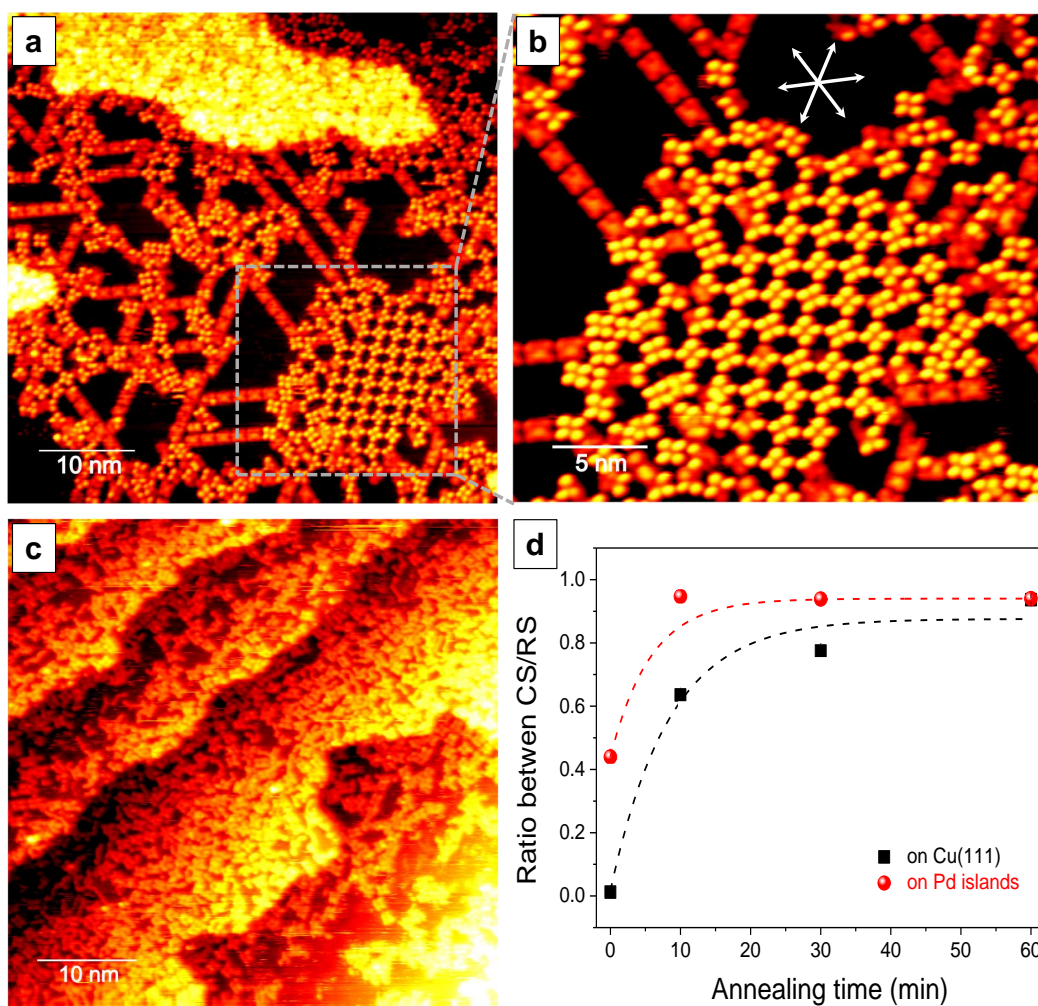


Figure 5.35: Representative STM images of 2H-TCNPP as function of the annealing time at 400 K (a)-(b) after 30 minutes and (c) after 60 minutes. $U = -1.44$ V and $I = 0.12$ nA. (d) Conversion ratio between the clover shape (CS) and inverted structure (IS) as a function of time (squares) and on Pd islands (spheres).

with subsequent diffusion to “Pd-free” regions of the Cu(111) surface or they have been catalyzed by Pd atoms in a Pd-Cu surface alloy that forms easily in Cu(111) as previously reported [174, 175].

In order to gain deeper insight into the 2D supramolecular ordered structures, we studied samples where 2D and 1D structures are coexisting after performing an annealing treatment at 400 K for 30 min. Thus, it is possible to determine the relation between the 2D ordered structure and the substrate orientations as shown in Figure 5.36 with high magnification and molecular resolution. We experimentally determined the unit cell of the porous network as: $\vec{a} = 2.8 \pm 0.1$ nm and $\vec{b} = 3.5 \pm 0.1$ nm with an internal angle of $90 \pm 2^\circ$, describing a rectangular molecular super-lattice with two clover shape motifs per

unit-cell. To establish a structural model for the clover shape motifs and determine what kind of molecule-substrate and molecule-molecule interactions are driving the formation of the peculiar structure it is necessary to understand the role of Pd on changing the appearance of 2H-TCNPP from the inverted structure to the clover shape. Previous studies reported that the yield of Cu porphyrin self-metalation is negligible at these temperatures [80]. Moreover, Cu-TCNPP does not exhibit clover shape motifs. Thus, one can discard porphyrin Cu-metalation as the source of the corresponding observation. As one alternative, one might consider porphyrin Pd-metalation. Quite generally, one can state that changes of the conformation of the pre-adsorbed molecules upon deposition of Fe, Co, and Pd are restricted to the saddle shape conformation instead of the clover shape conformation. Therefore, the clover shape motifs are likely to be caused by a different process than porphyrin metalation. One should not discard the possibility of Pd acting on the cyano termination, for example by promoting molecular dehydrogenation (e.g. from H₂ residual gas) and or forming Pd-CN bonds. For instance, Drain *et al.* [176] showed a strategy to form 2D porous network using porphyrins functionalized with pyridyl groups and Pd atoms as N-coordination linkers. In another work, Fendt *et al.* [177] reported that the catalytically activated process of hydrogen bonding in association with CN groups could promote upright-standing phenylene rings.

Since Pd has high affinity to hydrogen, [178] another possibility which appears reasonable are dehydrogenation processes within the porphyrin. One route would be a dehydrogenation and subsequent ring closure reaction of the phenyl and pyrrol groups. Such a reaction has been suggested by Di Santo *et al.* [152] and Wiengarten *et al.* [179] for tetraphenylporphyrins on Ag(111). The authors proposed dehydrogenation within the macrocycle with the formation of four new aryl-aryl carbon bonds when a ML is annealed at 550 K; two different conformations of the dehydrogenated molecule were observed, a spiral and a rectangular conformation. The same reaction was also proposed for 2H-TPP on Cu(111) by Xiao *et al.* [180] and Röckert *et al.* [181] as well as for 2HTPP and Ru-TPP on Ag(111) by Wiengarten *et al.* [179]. These authors studied the temperature-dependent porphyrin self-metalation and dehydrogenation process in great detail by x-ray photoelectron spectroscopy (XPS), STM and temperature programmed desorption (TPD). Upon annealing, they find progressive dehydrogenation yielding ring closure starting at 450 K, which results in a more planar configuration of the molecules. The successive ring closure

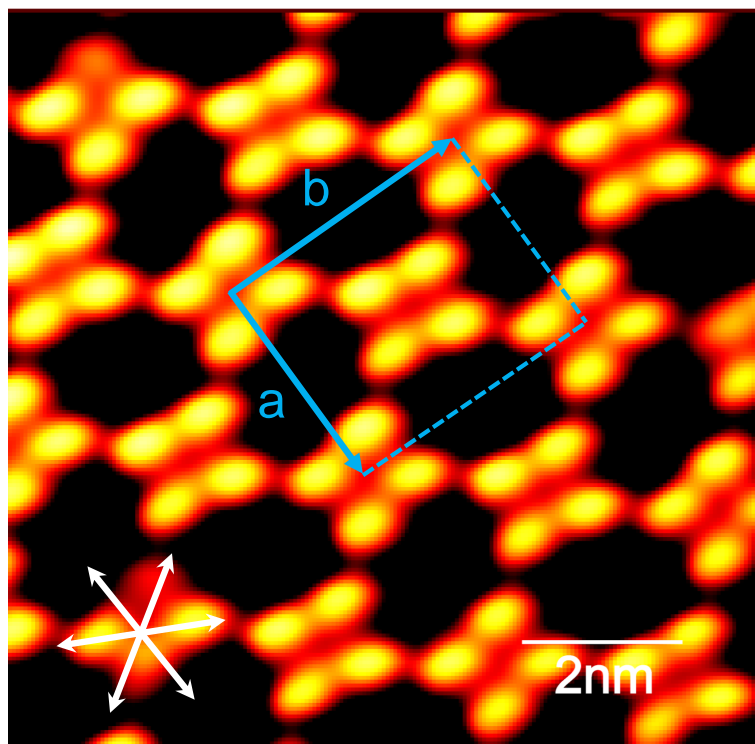


Figure 5.36: High-resolution STM image (9.5×9.5) nm² showing the lattice vectors of the periodic porous 2D network after 400 K annealing at 30 minutes. Tunneling parameters: $U = -1.44$ V and $I = 0.13$ nA.

reaction of the 4 phenyl rings with the neighboring pyrrole groups might explain the observed progressive formation of one, two, three and four leaves in the clover shape (see figure 5.34(b)). In Figure 5.37, we schematically display the reaction pathway leading to the spiral and the rectangular conformation after dehydrogenation (four leave clover) and correspondent experimental high-resolution STM images. Interestingly, the close inspection of Figure 5.36 indicated that both routes for ring closure can indeed be observed.

Searching for an alternative interpretation, we also found other examples in the literature describing changes on molecular conformation, particularly for 2H-porphyrins and 2H-phthalocyanines, due to the dehydrogenation of the pyrrole rings induced by the substrate or by adatoms [176, 177, 182–184] Auwärter *et al.* [183] reported a clover-like shape after tip-induced dehydrogenation of the two inner hydrogen atoms of 2HTPP on Ag(111), i.e., in a similar system. In addition, also Sperl *et al.* [182] showed a progressive dehydrogenation in the inner part of 2H-phthalocyanine induced by the STM tip that yields a similar appearance in the STM images, with one, two, and four leaves of the clover shape. However, neither the experimental data, nor the schematic model of Auwärter

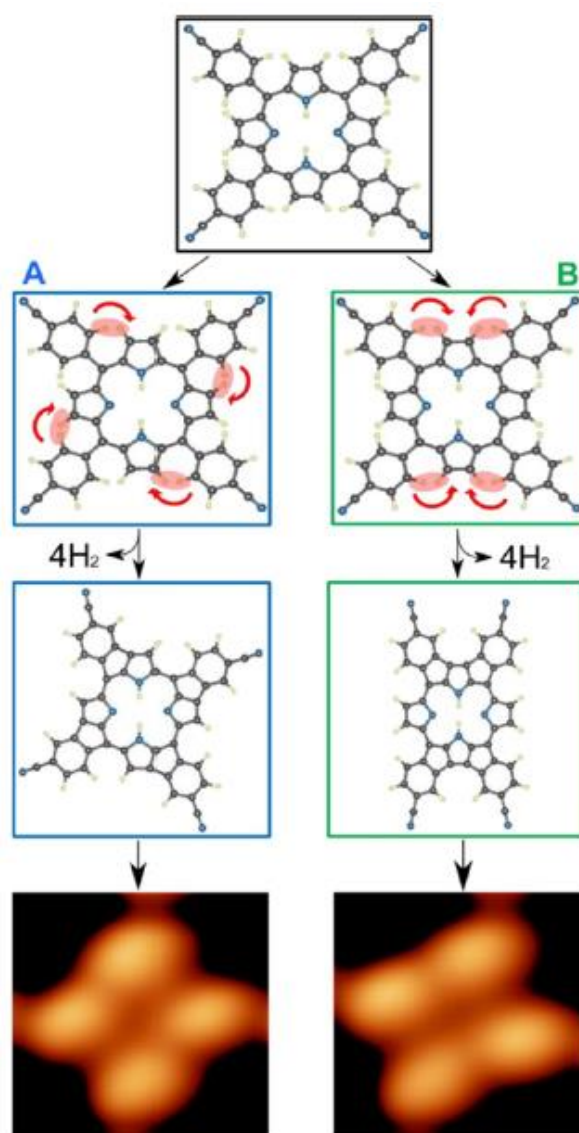


Figure 5.37: Schematic flat models for 2H-TCNPP molecules undergoing dehydrogenation and ring closure reaction, yielding spiral and rectangular structures and corresponding experimental STM images.

et al. and Sperl *et al.* are consistent with the existence of a three leaf species that we observe frequently. Therefore, it appears unlikely to us that observed clover shape could be indeed an TCNPP porphyrin with hydrogens removed from the imminic nitrogens by the presence of Pd.

The lateral arrangement in the long-range-ordered structure in Figure 5.36 can be described with a non-primitive unit cell containing two molecules and lattice vectors of $\vec{a} = 2.81$ nm and $\vec{b} = 3.53$ nm, which correspond to $(11 \times 8\sqrt{3})$ cells of Cu(111). We propose that this structure likely is stabilized by the interaction of the CN groups with Cu atoms from the Cu(111) surface, which could explain, why all individual leafs are slightly

distorted and rotated. In order to obtain a more detailed understanding with respect to the adsorption sites and the Cu mediated interactions, further studies based on density functional theory (DFT) calculations are required, which are however out of the scope of this thesis.

REMARKS

In summary, we have investigated the influence of Fe, Co and Pd on the self-assembly of 2H-TCNPP on Cu(111). After the deposition of Co and Fe, the molecules form 1D chains by metal CN-coordination aligned with the main crystallographic directions of Cu(111). After deposition of Pd, molecular chains are efficiently formed after annealing at 350 K only on the Pd-free regions of Cu(111), while on the Pd islands the molecules change their conformation to a clover shape appearance in STM. Furthermore, heating the sample to 400 K leads to the conversion of the molecules on the Cu(111) regions, from the inverted structure into the clover shape which breaks up the molecular chains and forms 2D supramolecular arrangements. At the same temperature, all observed molecules on Pd islands exhibit the clover shape. Thus, Pd plays a central role as catalyst in transforming 2H-TCNPP molecules to peculiar motif at a much lower temperature than Cu(111) and only in the presence of Pd the clover shape motifs can form stable 2D porous network on Cu(111). We suggest a dehydrogenation and subsequent ring closure reaction of the phenyl and pyrrol groups to explain the observed clover shape motif.

Conclusions and perspective

In this thesis, we studied the formation of molecular nanostructures on different reactive surfaces (Cu(111), Ag(111) and Gr/Ir (111)). The proposal, specifically, consists of understanding the very fundamental chemical and physical processes to establish effective ways on the synthesis of functional two-dimensional networks with halogenated tetraphenyl porphyrins (Cl₄TPP). The choice of the Cl element was strategic to study the activation of the surface-assisted Ullmann reaction, as well as its by-products. In parallel, we also studied the formation of organometallic networks from carbonitrile tetraphenyl porphyrins (2H- TCNPP) on Cu(111) with co-deposition of Pd atoms. Organometallic complexes are intermediate products of the surface polymerization reaction and, therefore, their study is extremely important. The combination of experimental techniques STM + XPS proved to be suitable since we were able to extract structural and chemical information from the intermediate and final products of the reactions induced on the surface. In addition, we had the opportunity to count on the complementarity of DFT calculations carried out by our theoretical collaborators, in which we were able to corroborate our results and also bring valuable information to the study. In general, we evaluated that the level of surface reactivity can be organized as follows: Gr < Ag < Cu. Thus, the dissociation of Cl terminations in the tetraphenyl porphyrins also follows the hierarchy for surface-assisted Ullmann coupling reaction.

For Cl₄TPP on Cu(111) we verified a strong interaction between molecules and surface, which is even capable of distorting the molecule in an “inverted” structure configuration. On the one hand, the strong interaction with the substrate hinders the mobility across the surface and, therefore, the ordered assembly between precursors. However, it favors the cleavage of Cl atoms of the molecule (close to RT), thus forming highly stable organometallic C–Cu–C species as final products. The combination of these factors makes it difficult to form a structured large-ordered 2D network, but it does indicate

the importance of the availability of adatoms for precise control of the dissociation and diffusion reactions on the surface.

In the case of Ag(111), the molecules less reactive to the substrate present wide diffusion and reorganize in a well-ordered supramolecular network. The adsorption has a saddle shape configuration that is well known in the literature. In an attempt to promote the formation of covalent bonds by a surface-assisted Ullmann-type coupling reaction, at temperatures above RT ($T \approx 400$ K) we obtain a new highly compact motif composed of completely dechlorinated molecules. The highly compact network, however, did not show covalent C–C interconnections between molecules. This is due to the fact that there is probably a lack of Ag adatoms available and steric hindrance in the highly compact overlayer.

For the weak interacting substrate Gr/Ir, we find a square compact self-assembly network stabilized by vdW intermolecular interaction. No reaction was induced over annealing and the molecules desorb completely from the surface at ~ 600 K, which made it difficult to control any kind of reactions in this system. Remarkably, the ML of Cl₄TPP protected the Gr sheet against H⁺ deposition and did not act as a porous network mask for controlled deposition as we expected. However, the Gr sheet on Ir(111) proved to be an interesting template for porphyrin-like molecules. Finally, the 2H-TCNPP on Cu(111) system showed, in the presence of Pd atoms, the transformation of 1D chains to stable 2D network upon mild annealing, suggesting that Pd plays a central role as a catalyst to the transformation.

The results herein presented show that for the construction of two-dimensional nanoarchitectures on coinage metal surfaces, it is necessary to have precise control of the available adatoms on the surface, as well as taking into account the ease (or not) of diffusion over the surface. At high temperatures, the concentration of adatoms increases significantly for Cu and to a lesser extent for Ag. The control of these atoms can also be done by controlled co-deposition by means of evaporators. The possible formation of highly stable organometallic intermediate compounds showed to be a problem for the effectiveness of the Ullmann reaction in ordered polymeric networks, especially for the Cl₄TPP on Cu(111) case. A possible route for future work is to perform sublimation at moderate temperatures, in order to instantly activate the halogen cleavage, giving room for diffusion and direct polymerization. This suggestion is especially suitable for the

Cl₄TPP on Ag(111) system since the easy diffusion on the surface could be interesting for regrouping large-ordered networks.

Finally, this study brings relevant information to the scientific community dedicated to the on-surface synthesis of polymeric two-dimensional networks, including new perspectives for the use of free-base porphyrins functionalized with Cl atoms. As a suggestion, an interesting next approach would be for tetraphenyl porphyrin molecules functionalized with F, which have few studies in the literature so far.

References

1. Senge, M. O., MacGowan, S. A. & O'Brien, J. M. Conformational control of cofactors in nature - the influence of protein-induced macrocycle distortion on the biological function of tetrapyrroles. *Chemical Communications* **51**, 17031–17063 (2015).
2. Storm, C. B. & Teklu, Y. Nitrogen–Hydrogen Tautomerism in Porphyrins and Chlorins. *Journal of the American Chemical Society* **94**, 1745–1747 (1972).
3. Schlabach, M. *et al.* NMR Study of Kinetic HH/HD/DH/DD Isotope Effects on the Tautomerism of Acetylporphyrin: Evidence for a Stepwise Double Proton Transfer. *Journal of the American Chemical Society* **115**, 4554–4565 (1993).
4. Limbach, H. H., Hennig, J., Kendrick, R. & Yannoni, C. S. Proton-Transfer Kinetics in Solids: Tautomerism in Free Base Porphines by ^{15}N CPMAS NMR. *Journal of the American Chemical Society* **106**, 4059–4060 (1984).
5. Merz, K. M. & Reynolds, C. H. Tautomerism in free base porphyrins: The porphyrin potential energy surface. *Journal of the Chemical Society, Chemical Communications*, 90–92 (1988).
6. Silvers, S. & Tulinsky, A. The Triclinic Crystal Form of $\alpha,\beta\gamma,\delta$ -Tetraphenylporphine. *Journal of the American Chemical Society* **86**, 927–928 (1964).
7. Fleischer, E. B., Miller, C. K. & Webb, L. E. Crystal and Molecular Structures of Some Metal Tetraphenylporphines. *Journal of the American Chemical Society* **86**, 2342–2347 (1964).
8. Gottfried, J. M. Surface chemistry of porphyrins and phthalocyanines. *Surface Science Reports* **70**, 259–379 (2015).

9. Brand, H. & Arnold, J. Recent developments in the chemistry of early transition metal porphyrin compounds. *Coordination Chemistry Reviews* **140**, 137–168 (1995).
10. Auwärter, W., Écija, D., Klappenberger, F. & Barth, J. V. Porphyrins at interfaces. *Nature Chemistry* **7**, 105–120 (2015).
11. Garah, M. E. *et al.* Molecular tectonics based nanopatterning of interfaces with 2D metal-organic frameworks (MOFs). *Chemical Communications* **50**, 12250–12253 (2014).
12. Klappenberger, F. Two-dimensional functional molecular nanoarchitectures - Complementary investigations with scanning tunneling microscopy and X-ray spectroscopy. *Progress in Surface Science* **89**, 1–55 (2014).
13. Mahmood, A. *et al.* Recent progress in porphyrin-based materials for organic solar cells. *Journal of Materials Chemistry A* **6**, 16769–16797 (2018).
14. Meng, L. *et al.* Organic and solution-processed tandem solar cells with 17.3 % efficiency. *Science* **361**, 1094–1098 (2018).
15. An, Q., Wang, J. & Zhang, F. Ternary polymer solar cells with alloyed donor achieving 14.13 % efficiency and 78.4 % fill factor. *Nano Energy* **60**, 768–774 (2019).
16. Burroughes, J. H. *et al.* Light-emitting diodes based on conjugated polymers. *Nature* **347**, 539–541 (1990).
17. Gutzler, R. & Perepichka, D. F. π -Electron Conjugation in Two Dimensions. *Journal of the American Chemical Society* **135**, 16585–16594 (2013).
18. Meng, Z., Stolz, R. M. & Mirica, K. A. Two-Dimensional Chemiresistive Covalent Organic Framework with High Intrinsic Conductivity. *Journal of the American Chemical Society* **141**, 11929–11937 (2019).
19. Bi, Y. G. *et al.* Ultrathin Metal Films as the Transparent Electrode in ITO-Free Organic Optoelectronic Devices. *Advanced Optical Materials* **7**, 1–23 (2019).
20. Sengupta, S. *et al.* Biosupramolecular nanowires from chlorophyll dyes with exceptional charge-transport properties. *Angewandte Chemie - International Edition* **51**, 6378–6382 (2012).

21. Sarikaya, M., Tamerler, C., Jen, A. K., Schulten, K. & Baneyx, F. Molecular biomimetics: nanotechnology through biology. *Nature Materials* **2**, 577–585 (2003).
22. Zhang, Q. *et al.* Assembling a Natural Small Molecule into a Supramolecular Network with High Structural Order and Dynamic Functions. *Journal of the American Chemical Society* **141**, 12804–12814 (2019).
23. Jiang, L. *et al.* Low-temperature, bottom-up synthesis of graphene via a radical-coupling reaction. *Journal of the American Chemical Society* **135**, 9050–9054 (2013).
24. Calogero, G., Alcón, I., Papior, N., Jauho, A. P. & Brandbyge, M. Quantum Interference Engineering of Nanoporous Graphene for Carbon Nanocircuitry. *Journal of the American Chemical Society* **141**, 13081–13088 (2019).
25. Lu, H. *et al.* On-Surface Fabrication of Small-Sized Nanoporous Graphene. *Journal of Physical Chemistry C* **123**, 14404–14407 (2019).
26. Cai, J. *et al.* Atomically precise bottom-up fabrication of graphene nanoribbons. *Nature* **466**, 470–473 (2010).
27. Chen, Y. C. *et al.* Molecular bandgap engineering of bottom-up synthesized graphene nanoribbon heterojunctions. *Nature Nanotechnology* **10**, 156–160 (2015).
28. Talirz, L., Ruffieux, P. & Fasel, R. On-Surface Synthesis of Atomically Precise Graphene Nanoribbons. *Advanced Materials* **28**, 6222–6231 (2016).
29. Kumar, A., Banerjee, K. & Liljeroth, P. Molecular assembly on two-dimensional materials. *Nanotechnology* **28** (2017).
30. Bazarnik, M., Brede, J., Decker, R. & Wiesendanger, R. Tailoring Molecular Self-assembly of Magnetic Phthalocyanine Molecules on Fe- and Co-Intercalated Graphene. *ACS Nano* **7**, 11341–11349 (2013).
31. Mao, J. *et al.* Tunability of supramolecular kagome lattices of magnetic phthalocyanines using graphene-based moiré patterns as templates. *Journal of the American Chemical Society* **131**, 14136–14137 (2009).
32. Corso, M. *et al.* Boron Nitride Nanomesh. *Science* **303**, 217–220 (2004).
33. Schlickum, U. *et al.* Metal-organic honeycomb nanomeshes with tunable cavity size. *Nano Letters* **7**, 3813–3817 (2007).

34. Barth, J. V., Costantini, G. & Kern, K. Engineering atomic and molecular nanostructures at surfaces. *Nature* **437**, 671–679 (2005).
35. Gates, B. D. *et al.* New approaches to nanofabrication: Molding, printing, and other techniques. *Chemical Reviews* **105**, 1171–1196 (2005).
36. Auwärter, W. Hexagonal boron nitride monolayers on metal supports: Versatile templates for atoms, molecules and nanostructures. *Surface Science Reports* **74**, 1–95 (2019).
37. Dong, L., Gao, Z. A. & Lin, N. Self-assembly of metal–organic coordination structures on surfaces. *Progress in Surface Science* **91**, 101–135 (2016).
38. De Feyter, S. & De Schryver, F. C. Two-dimensional supramolecular self-assembly probed by scanning tunneling microscopy. *Chemical Society Reviews* **32**, 139–150 (2003).
39. Slater, A. G., Beton, P. H. & Champness, N. R. Two-dimensional supramolecular chemistry on surfaces. *Chemical Science* **2**, 1440–1448 (2011).
40. Kudernac, T., Lei, S., Elemans, J. A. & De Feyter, S. Two-dimensional supramolecular self-assembly: Nanoporous networks on surfaces. *Chemical Society Reviews* **38**, 402–421 (2009).
41. Shen, Y. *et al.* Self-assembling in fabrication of ordered porphyrins and phthalocyanines hybrid nano-arrays on HOPG. *CrystEngComm* **15**, 5526–5531 (2013).
42. Rojas, G. *et al.* Self-assembly and properties of nonmetalated tetraphenyl-porphyrin on metal substrates. *Journal of Physical Chemistry C* **114**, 9408–9415 (2010).
43. Lepper, M. *et al.* "Inverted" porphyrins: A distorted adsorption geometry of free-base porphyrins on Cu(111). *Chemical Communications* **53**, 8207–8210 (2017).
44. Ryan, P. T. *et al.* Validation of the inverted adsorption structure for free-base tetraphenyl porphyrin on Cu(111). *Chemical Communications* **56**, 3681–3684 (2020).
45. Rojas, G. *et al.* Surface state engineering of molecule-molecule interactions. *Physical Chemistry Chemical Physics* **14**, 4971–4976 (2012).
46. Stark, M. *et al.* Coverage dependent disorder-order transition of 2H-tetraphenylporphyrin on Cu(111). *Langmuir* **29**, 4104–4110 (2013).

47. Lepper, M. *et al.* Adsorption Behavior of a Cyano-Functionalized Porphyrin on Cu(111) and Ag(111): From Molecular Wires to Ordered Supramolecular Two-Dimensional Aggregates. *Journal of Physical Chemistry C* **121**, 26361–26371 (2017).
48. Buchner, F. *et al.* Ordering aspects and intramolecular conformation of tetraphenylporphyrins on Ag(111). *Physical Chemistry Chemical Physics* **12**, 13082–13090 (2010).
49. Kanuru, V. K. *et al.* Sonogashira coupling on an extended gold surface in vacuo: Reaction of phenylacetylene with iodobenzene on Au(111). *Journal of the American Chemical Society* **132**, 8081–8086 (2010).
50. Zhong, D. *et al.* Linear alkane polymerization on a gold surface. *Science* **334**, 213–216 (2011).
51. Ullmann, F. & Bielecki, J. Ueber Synthesen in der Biphenylreihe. *Berichte der deutschen chemischen Gesellschaft* **34**, 2174–2185 (1901).
52. Lackinger, M. Surface-assisted Ullmann coupling. *Chemical Communications* **53**, 7872–7885 (2017).
53. Bischoff, F. *et al.* How surface bonding and repulsive interactions cause phase transformations: Ordering of a prototype macrocyclic compound on Ag(111). *ACS Nano* **7**, 3139–3149 (2013).
54. Lukasczyk, T. *et al.* Interaction of cobalt(II) tetraarylporphyrins with a Ag(111) surface studied with photoelectron spectroscopy. *Journal of Physical Chemistry C* **111**, 3090–3098 (2007).
55. Diller, K. *et al.* Investigating the molecule-substrate interaction of prototypic tetrapyrrole compounds: Adsorption and self-metalation of porphine on Cu(111). *Journal of Chemical Physics* **138** (2013).
56. Auwärter, W. *et al.* Site-specific electronic and geometric interface structure of Co-tetraphenyl-porphyrin layers on Ag(111). *Physical Review B - Condensed Matter and Materials Physics* **81**, 1–14 (2010).
57. Iancu, V., Deshpande, A. & Hla, S. W. Manipulating Kondo temperature via single molecule switching. *Nano Letters* **6**, 820–823 (2006).

58. Scheybal, A. *et al.* Induced magnetic ordering in a molecular monolayer. *Chemical Physics Letters* **411**, 214–220 (2005).
59. Bhandary, S. *et al.* Manipulation of spin state of iron porphyrin by chemisorption on magnetic substrates. *Physical Review B - Condensed Matter and Materials Physics* **88**, 1–9 (2013).
60. Parkin, S. *et al.* Magnetically engineered spintronic sensors and memory. *Proceedings of the IEEE* **91**, 661–679 (2003).
61. Berner, S. *et al.* Activity boost of a biomimetic oxidation catalyst by immobilization onto a gold surface. *Journal of Catalysis* **244**, 86–91 (2006).
62. Den Boer, D. *et al.* Detection of different oxidation states of individual manganese porphyrins during their reaction with oxygen at a solid/liquid interface. *Nature Chemistry* **5**, 621–627 (2013).
63. Hulsken, B. *et al.* Real-time single-molecule imaging of oxidation catalysis at a liquid-solid interface. *Nature Nanotechnology* **2**, 285–289 (2007).
64. Xue, T. *et al.* Graphene-supported hemin as a highly active biomimetic oxidation catalyst. *Angewandte Chemie - International Edition* **51**, 3822–3825 (2012).
65. Sedona, F. *et al.* Tuning the catalytic activity of Ag(110)-supported Fe phthalocyanine in the oxygen reduction reaction. *Nature Materials* **11**, 970–977 (2012).
66. Moresco, F. *et al.* Conformational changes of single molecules induced by scanning tunneling microscopy manipulation: a route to molecular switching. *Physical Review Letters* **86**, 672–675 (2001).
67. Auwärter, W. *et al.* Self-assembly and conformation of tetrapyrrolyl-porphyrin molecules on Ag(111). *Journal of Chemical Physics* **124** (2006).
68. Auwärter, W. *et al.* Conformational adaptation and selective adatom capturing of tetrapyrrolyl-porphyrin molecules on a copper (111) surface. *Journal of the American Chemical Society* **129**, 11279–11285 (2007).
69. Donovan, P., Robin, A., Dyer, M. S., Persson, M. & Raval, R. Unexpected deformations induced by surface interaction and chiral self-assembly of CoII-tetraphenylporphyrin (Co-TPP) adsorbed on Cu(110): A combined STM and periodic DFT study. *Chemistry - A European Journal* **16**, 11641–11652 (2010).

70. Seufert, K. *et al.* Cis-dicarbonyl binding at cobalt and iron porphyrins with saddle-shape conformation. *Nature Chemistry* **3**, 114–119 (2011).
71. Holliday, B. J. & Mirkin, C. A. Strategies for the Construction of Supramolecular Compounds through Coordination Chemistry. *Angewandte Chemie - International Edition* **40**, 2022–2043 (2001).
72. Barth, J. V. Molecular architectonic on metal surfaces. *Annual Review of Physical Chemistry* **58**, 375–407 (2007).
73. Tait, S. L. *et al.* Metal-organic coordination interactions in Fe-terephthalic acid networks on Cu(100). *Journal of the American Chemical Society* **130**, 2108–2113 (2008).
74. Abdurakhmanova, N. *et al.* Superexchange-mediated ferromagnetic coupling in two-dimensional Ni-TCNQ networks on metal surfaces. *Physical Review Letters* **110**, 1–5 (2013).
75. Björk, J. *et al.* STM fingerprint of molecule-atom interactions in a self-assembled metal-organic surface coordination network on Cu(111). *Physical Chemistry Chemical Physics* **12**, 8815–8821 (2010).
76. Gottardi, S. *et al.* Cyano-Functionalized Triarylamine on Au(111): Competing Intermolecular versus Molecule/Substrate Interactions. *Advanced Materials Interfaces* **1**, 1–10 (2014).
77. Reichert, J. *et al.* Competing interactions in surface reticulation with a prochiral dicyanitrile linker. *Journal of Physical Chemistry C* **117**, 12858–12863 (2013).
78. Tseng, T. C. *et al.* Two-dimensional metal-organic coordination networks of Mn-7,7,8,8-tetracyanoquinodimethane assembled on Cu(100): Structural, electronic, and magnetic properties. *Physical Review B - Condensed Matter and Materials Physics* **80**, 1–6 (2009).
79. Urgel, J. I. *et al.* Controlling coordination reactions and assembly on a Cu(111) supported boron nitride monolayer. *Journal of the American Chemical Society* **137**, 2420–2423 (2015).

80. Lepper, M. *et al.* Controlling the Self-Metalation Rate of Tetraphenylporphyrins on Cu(111) via Cyano Functionalization. *Angewandte Chemie - International Edition* **57**, 10074–10079 (2018).
81. Barton, D. *et al.* Formation of Organometallic Intermediate States in On-Surface Ullmann Couplings. *Chemistry - A European Journal* **23**, 6190–6197 (2017).
82. Bieri, M. *et al.* Porous graphenes: Two-dimensional polymer synthesis with atomic precision. *Chemical Communications*, 6919–6921 (2009).
83. Basagni, A. *et al.* Molecules-oligomers-nanowires-graphene nanoribbons: A bottom-up stepwise on-surface covalent synthesis preserving long-range order. *Journal of the American Chemical Society* **137**, 1802–1808 (2015).
84. Zhang, H. *et al.* On-surface synthesis of rylene-type graphene nanoribbons. *Journal of the American Chemical Society* **137**, 4022–4025 (2015).
85. Treier, M. *et al.* Surface-assisted cyclodehydrogenation provides a synthetic route towards easily processable and chemically tailored nanographenes. *Nature Chemistry* **3**, 61–67 (2011).
86. Fan, Q., Zhu, J. & Gottfried, J. in *Encyclopedia of Interfacial Chemistry* (ed Wandelt, K.) 343–353 (Elsevier, Oxford, 2018).
87. Fan, Q., Gottfried, J. M. & Zhu, J. Surface-Catalyzed C-C Covalent Coupling Strategies toward the Synthesis of Low-Dimensional Carbon-Based Nanostructures. *Accounts of Chemical Research* **48**, 2484–2494 (2015).
88. Lewis, E. A., Murphy, C. J., Liriano, M. L. & Sykes, E. C. H. Atomic-scale insight into the formation, mobility and reaction of Ullmann coupling intermediates. *Chemical Communications* **50**, 1006–1008 (2014).
89. Lewis, E. A., Murphy, C. J., Pronschinske, A., Liriano, M. L. & Sykes, E. C. Nanoscale insight into C-C coupling on cobalt nanoparticles. *Chemical Communications* **50**, 10035–10037 (2014).
90. Grill, L. *et al.* Nano-architectures by covalent assembly of molecular building blocks. *Nature Nanotechnology* **2**, 687–691 (2007).

91. Eichhorn, J. *et al.* On-surface ullmann coupling: The influence of kinetic reaction parameters on the morphology and quality of covalent networks. *ACS Nano* **8**, 7880–7889 (2014).
92. Eichhorn, J. in *Encyclopedia of Interfacial Chemistry* (ed Wandelt, K.) 406–413 (Elsevier, Oxford, 2018).
93. Björk, J., Hanke, F. & Stafström, S. Mechanisms of halogen-based covalent self-assembly on metal surfaces. *Journal of the American Chemical Society* **135**, 5768–5775 (2013).
94. Binnig, G., Rohrer, H., Gerber, C. & Weibel, E. Tunneling through a controllable vacuum gap. *Applied Physics Letters* **40**, 178–180 (1982).
95. Lounis, S. *Theory of Scanning Tunneling Microscopy* (2014). arXiv: 1404.0961.
96. Binnig, G., Rohrer, H., Gerber, C. & Weibel, E. Surface Studies by Scanning Tunneling Microscopy. *Phys. Rev. Lett.* **49**, 57–61 (1982).
97. Binnig, G. *et al.* Tunneling spectroscopy and inverse photoemission: Image and field states. *Physical Review Letters* **55**, 991–994 (1985).
98. Crommie, M., Lutz, C. & Eigler, D. Imaging standing waves in a 2D electron gas. *Nature* **363**, 524–527 (1993).
99. Stipe, B. C., Rezaei, M. A. & Ho, W. Inducing and viewing the rotational motion of a single molecule. *Science* **279**, 1907–1909 (1998).
100. Heinrich, A. J., Gupta, J. A., Lutz, C. P. & Eigler, D. M. Single-Atom Spin-Flip Spectroscopy. *Science* **306**, 466–469 (2004).
101. Hirjibehedin, C. F., Lutz, C. P. & Heinrich, A. J. Spin coupling in engineered atomic structures. *Science* **312**, 1021–1024 (2006).
102. Wu, S. W., Ogawa, N. & Ho, W. Atomic-scale coupling of photons to single-molecule junctions. *Science* **312**, 1362–1365 (2006).
103. Eigler, M. D. & Schweizer, K. E. Positioning single atoms with a scanning tunnelling microscope. *Nature* **344**, 524–526 (1990).
104. Chen, C. J. *Introduction to scanning tunneling microscopy* 2nd ed. (Oxford University Press, 2007).

105. Bocquet, M. L. & Sautet, P. STM and chemistry: A qualitative molecular orbital understanding of the image of CO on a Pt surface. *Surface Science* **360**, 128–136 (1996).
106. Mizutani, W., Shigeno, M., Ono, M. & Kajimura, K. Voltage-dependent scanning tunneling microscopy images of liquid crystals on graphite. *Applied Physics Letters* **56**, 1974–1976 (1990).
107. Khajetoorians, A. A. *et al.* Itinerant nature of atom-magnetization excitation by tunneling electrons. *Physical Review Letters* **106**, 6–9 (2011).
108. Pascual, J. I. *et al.* Seeing molecular orbitals. *Chemical Physics Letters* **321**, 78–82 (2000).
109. Repp, J., Meyer, G., Stojković, S. M., Gourdon, A. & Joachim, C. Molecules on insulating films: Scanning-tunneling microscopy imaging of individual molecular orbitals. *Physical Review Letters* **94**, 1–4 (2005).
110. Mizutani, W., Shigeno, M., Kajimura, K. & Ono, M. Tunneling through a deformed potential. *Ultramicroscopy* **42-44**, 236–241 (1992).
111. Spong, J. K. *et al.* Contrast mechanism for resolving organic molecules with tunneling microscopy. *Nature* **338**, 137–139 (1989).
112. Lang, N. D. Apparent barrier height in scanning tunneling microscopy. *Physical Review B* **37**, 10395–10398 (1988).
113. Weber, R. & Peria, W. Work function and structural studies of alkali-covered semiconductors. *Surface Science* **14**, 13–38 (1969).
114. Hertz, H. Ueber einen Einfluss des ultravioletten Lichtes auf die electrische Entladung. *Annalen der Physik* **267**, 983–1000 (1887).
115. Einstein, A. Über einen die Erzeugung und Verwandlung des Lichtes betreffenden heuristischen Gesichtspunkt. *Annalen der Physik* **322**, 132–148 (1905).
116. Millikan, R. A. A Direct Photoelectric Determination of Planck's " h ". *Phys. Rev.* **7**, 355–388 (1916).
117. Reinert, F. & Hüfner, S. Photoemission spectroscopy—from early days to recent applications. *New Journal of Physics* **7**, 97–97 (2005).

118. Hüfner, S. *Photoelectron Spectroscopy—Principles and Application* 3rd ed. (Springer, 2003).
119. Hofmann, P. *Surface Physics: An Introduction* 1st ed. (self-published, 2013).
120. Flechtner, K. *et al.* Surface-confined two-step synthesis of the complex (ammine)(meso-tetraphenylporphyrinato)-zinc(II) on Ag(111). *Journal of Physical Chemistry C* **111**, 5821–5824 (2007).
121. Chiang, T.-C., Kaindl, G. & Mandel, T. Layer-resolved shifts of photoemission and Auger spectra from physisorbed rare-gas multilayers. *Phys. Rev. B* **33**, 695–711 (2 Jan. 1986).
122. Briggs, D. & Seah, M. *Practical Surface Analysis, Auger and X-ray Photoelectron Spectroscopy* 1st ed. (Wiley, 1990).
123. Arrhenius, S. Über die Reaktionsgeschwindigkeit bei der Inversion von Rohrzucker durch Säuren. *Zeitschrift für Physikalische Chemie* **4U** (2017).
124. Barth, J. Transport of adsorbates at metal surfaces: from thermal migration to hot precursors. *Surface Science Reports* **40**, 75–149 (2000).
125. Marbach, H. & Steinrück, H. P. Studying the dynamic behaviour of porphyrins as prototype functional molecules by scanning tunnelling microscopy close to room temperature. *Chemical Communications* **50**, 9034–9048 (2014).
126. Nečas, D. & Klapetek, P. Gwyddion: An open-source software for SPM data analysis. *Central European Journal of Physics* **10**, 181–188 (2012).
127. Horcas, I. *et al.* WSXM: A software for scanning probe microscopy and a tool for nanotechnology. *Review of Scientific Instruments* **78** (2007).
128. Eichberger, M. *et al.* Dimerization boosts one-dimensional mobility of conformationally adapted porphyrins on a hexagonal surface atomic lattice. *Nano Letters* **8**, 4608–4613 (2008).
129. Weckesser, J., Barth, J. V., Cai, C., Müller, B. & Kern, K. Binding and ordering of large organic molecules on an anisotropic metal surface: PVBA on Pd (110). *Surface Science* **431**, 168–173 (1999).

130. Buchner, F. *et al.* Diffusion, rotation, and surface chemical bond of individual 2 H-tetraphenylporphyrin molecules on Cu(111). *Journal of Physical Chemistry C* **115**, 24172–24177 (2011).
131. Janiak, C. A critical account on π - π stacking in metal complexes with aromatic nitrogen-containing ligands. *Journal of the Chemical Society, Dalton Transactions*, 3885–3896 (2000).
132. Hunter, C. A., Lawson, K. R., Perkins, J. & Urch, C. J. Aromatic interactions. *Journal of the Chemical Society, Perkin Transactions 2*, 651–669 (2001).
133. Xu, D. *et al.* π - π Interaction of Aromatic Groups in Amphiphilic Molecules Directing for Single-Crystalline Mesostructured Zeolite Nanosheets. *Nature Communications* **5**, 1–9 (2014).
134. Albrecht, F., Bischoff, F., Auwärter, W., Barth, J. V. & Repp, J. Direct Identification and Determination of Conformational Response in Adsorbed Individual Nonplanar Molecular Species Using Noncontact Atomic Force Microscopy. *Nano Letters* **16**, 7703–7709 (2016).
135. Jarvis, S. P. *et al.* Physisorption Controls the Conformation and Density of States of an Adsorbed Porphyrin. *Journal of Physical Chemistry C* **119**, 27982–27994 (2015).
136. Mielke, J. *et al.* Adatoms underneath single porphyrin molecules on Au(111). *Journal of the American Chemical Society* **137**, 1844–1849 (2015).
137. Bui, T. T. T., Dahaoui, S., Lecomte, C., Desiraju, G. R. & Espinosa, E. The nature of halogen halogen interactions: A model derived from experimental charge-density analysis. *Angewandte Chemie - International Edition* **48**, 3838–3841 (2009).
138. Bosch, E. & Barnes, C. L. Triangular Halogen-Halogen-Halogen Interactions as a Cohesive Force in the Structures of Trihalomesitylenes. *Crystal Growth and Design* **2**, 299–302 (2002).
139. Zhang, Z. & Lagally, M. G. Atomistic processes in the early stages of thin-film growth. *Science* **276**, 377–383 (1997).

140. Wagner, C. D. & Muilenberg, G. E. *Handbook of X-ray Photoelectron Spectroscopy : A Reference Book of Standard Data for Use in X-ray Photoelectron Spectroscopy* (Eden Prairie: Perkin-Elmer Corp., 1979).
141. Perdew, J. P., Burke, K. & Ernzerhof, M. Generalized Gradient Approximation Made Simple. *Phys. Rev. Lett.* **77**, 3865–3868 (1996).
142. Grimme, S., Antony, J., Ehrlich, S. & Krieg, H. A consistent and accurate ab initio parametrization of density functional dispersion correction (DFT-D) for the 94 elements H-Pu. *The Journal of Chemical Physics* **132**, 154104 (2010).
143. Riss, A. *et al.* Imaging single-molecule reaction intermediates stabilized by surface dissipation and entropy. *Nature Chemistry* **8**, 678–683 (2016).
144. Yokoyama, T., Yokoyama, S., Kamikado, T. & Mashiko, S. Nonplanar adsorption and orientational ordering of porphyrin molecules on Au(111). *Journal of Chemical Physics* **115**, 3814–3818 (2001).
145. Yokoyama, T., Yokoyama, S., Kamikado, T., Okuno, Y. & Mashiko, S. Selective assembly on a surface of supramolecular aggregates with controlled size and shape. *Nature* **413**, 619–621 (2001).
146. Lafferentz, L. *et al.* Controlling on-surface polymerization by hierarchical and substrate-directed growth. *Nature Chemistry* **4**, 215–220 (2012).
147. Moreno-López, J. C. *et al.* Roles of Precursor Conformation and Adatoms in Ullmann Coupling: An Inverted Porphyrin on Cu(111). *Chemistry of Materials* **31**, 3009–3017 (2019).
148. Brede, J. *et al.* Dynamics of molecular self-ordering in tetraphenyl porphyrin monolayers on metallic substrates. *Nanotechnology* **20** (2009).
149. Merz, L. & Ernst, K. H. Unification of the matrix notation in molecular surface science. *Surface Science* **604**, 1049–1054 (2010).
150. Beamson, G. & Briggs, D. *High resolution XPS of organic polymers - The Scienta ESCA 300 data base* (John Wiley & Sons, 1992).
151. Bowker, M., Wolfindale, B., King, D. A. & Lamble, G. The coadsorption of K and Cl on Ag(100): Electronic, kinetic and thermodynamic surface modification by promotion. *Surface Science* **192**, 95–106 (1987).

152. Di Santo, G. *et al.* Supramolecular engineering through temperature-induced chemical modification of 2h-tetraphenylporphyrin on Ag(111): Flat phenyl conformation and possible dehydrogenation reactions. *Chemistry - A European Journal* **17**, 14354–14359 (2011).
153. Ceccatto Dos Santos, A. *et al.* Cyano-Functionalized Porphyrins on Cu(111) from One-Dimensional Wires to Two-Dimensional Molecular Frameworks: On the Role of Co-Deposited Metal Atoms. *Chemistry of Materials* **32**, 2114–2122 (2020).
154. Bowker, M. & Waugh, K. C. The adsorption of chlorine and chloridation of Ag(111). *Surface Science* **134**, 639–664 (1983).
155. Balog, R. *et al.* Controlling hydrogenation of graphene on Ir(111). *ACS Nano* **7**, 3823–3832 (2013).
156. Balog, R. *et al.* Bandgap opening in graphene induced by patterned hydrogen adsorption. *Nature Materials* **9**, 315–319 (2010).
157. Kyhl, L., Balog, R., Angot, T., Hornekær, L. & Bisson, R. Hydrogenated graphene on Ir(111): A high-resolution electron energy loss spectroscopy study of the vibrational spectrum. *Physical Review B* **93**, 1–9 (2016).
158. Grånäs, E. *et al.* Oxygen intercalation under graphene on Ir(111): Energetics, kinetics, and the role of graphene edges. *ACS Nano* **6**, 9951–9963 (2012).
159. Jørgensen, J. H. *et al.* Symmetry-Driven Band Gap Engineering in Hydrogen Functionalized Graphene. *ACS Nano* **10**, 10798–10807 (2016).
160. Bostwick, A. *et al.* Quasiparticle transformation during a metal-insulator transition in graphene. *Physical Review Letters* **103**, 1–4 (2009).
161. N'Diaye, A. T., Coraux, J., Plasa, T. N., Busse, C. & Michely, T. Structure of epitaxial graphene on Ir(111). *New Journal of Physics* **10** (2008).
162. Busse, C. *et al.* Graphene on Ir(111): Physisorption with chemical modulation. *Physical Review Letters* **107**, 1–4 (2011).
163. De Campos Ferreira, R. C. *et al.* Unraveling the Atomic Structure of Fe Intercalated under Graphene on Ir(111): A Multitechnique Approach. *Chemistry of Materials* **30**, 7201–7210 (2018).

164. Coraux, J., N'Diaye, A. T., Busse, C. & Michely, T. Structural coherency of graphene on Ir(111). *Nano Letters* **8**, 565–570 (2008).
165. Standop, S. *et al.* Ion impacts on graphene/Ir(111): Interface channeling, vacancy funnels, and a nanomesh. *Nano Letters* **13**, 1948–1955 (2013).
166. N'Diaye, A. T., Bleikamp, S., Feibelman, P. J. & Michely, T. Two-dimensional Ir cluster lattice on a graphene moiré on Ir(111). *Physical Review Letters* **97**, 1–4 (2006).
167. Lacovig, P. *et al.* Growth of dome-shaped carbon nanoislands on Ir(111): The intermediate between carbidic clusters and quasi-free-standing graphene. *Physical Review Letters* **103**, 14–17 (2009).
168. Hüfner, S. & Wertheim, G. K. Core-line asymmetries in the x-ray photoemission spectra of metals: A comment. *Phys. Rev. B* **11**, 5197–5198 (1975).
169. De Campos Ferreira, R. C. *et al.* Supramolecular Ordering and Reactions of a Chlorophenyl Porphyrin on Ag(111). *The Journal of Physical Chemistry C* (2020).
170. Wu, Y. *et al.* High-frequency, scaled graphene transistors on diamond-like carbon. *Nature* **472**, 74–78 (2011).
171. Buchner, F. *et al.* Chemical fingerprints of large organic molecules in scanning tunneling microscopy: Imaging adsorbate-substrate coupling of metalloporphyrins. *Journal of Physical Chemistry C* **113**, 16450–16457 (2009).
172. Klyatskaya, S. *et al.* Surface-confined self-assembly of Di-carbonitrile polyphenyls. *Advanced Functional Materials* **21**, 1230–1240. ISSN: 1616301X (2011).
173. Klappenberger, F. *et al.* Uniform π -system alignment in thin films of template-grown dicarbonitrile-oligophenyls. *Advanced Functional Materials* **21**, 1631–1642 (2011).
174. De Siervo, A. *et al.* Pd on Cu(1 1 1) studied by photoelectron diffraction. *Surface Science* **504**, 215–222 (2002).
175. Bach Aaen, A., Laegsgaard, E., Ruban, A. V. & Stensgaard, I. Submonolayer growth of Pd on Cu(111) studied by scanning tunneling microscopy. *Surface Science* **408**, 43–56 (1998).

176. Drain, C. M. *et al.* Designing supramolecular porphyrin arrays that self-organize into nanoscale optical and magnetic materials. *Proceedings of the National Academy of Sciences of the United States of America* **99**, 6498–6502 (2002).
177. Fendt, L. A. *et al.* Modification of supramolecular binding motifs induced by substrate registry: Formation of self-assembled macrocycles and chain-like patterns. *Chemistry - A European Journal* **15**, 11139–11150 (2009).
178. Konda, S. K. & Chen, A. Palladium based nanomaterials for enhanced hydrogen spillover and storage. *Materials Today* **19**, 100–108 (2016).
179. Wiengarten, A. *et al.* Surface-Assisted Cyclodehydrogenation; Break the Symmetry, Enhance the Selectivity. *Chemistry - A European Journal* **21**, 12285–12290 (2015).
180. Xiao, J. *et al.* Temperature-dependent chemical and structural transformations from 2H-tetraphenylporphyrin to copper(II)-tetraphenylporphyrin on Cu(111). *Journal of Physical Chemistry C* **116**, 12275–12282 (2012).
181. Röckert, M. *et al.* Coverage- and temperature-dependent metalation and dehydrogenation of tetraphenylporphyrin on Cu(111). *Chemistry - A European Journal* **20**, 8948–8953 (2014).
182. Sperl, A., Kröger, J. & Berndt, R. Controlled metalation of a single adsorbed phthalocyanine. *Angewandte Chemie - International Edition* **50**, 5294–5297 (2011).
183. Auwärter, W. *et al.* A surface-anchored molecular four-level conductance switch based on single proton transfer. *Nature Nanotechnology* **7**, 41–46 (2012).
184. Vörden, D. v. *et al.* Communication: Substrate induced dehydrogenation: Transformation of octa-ethyl-porphyrin into tetra-benzo-porphyrin. *The Journal of Chemical Physics* **138**, 211102 (2013).
185. Bardeen, J. Tunnelling from a Many-Particle Point of View. *Phys. Rev. Lett.* **6**, 57–59 (1961).
186. Tersoff, J. & Hamann, D. R. Theory and Application for the Scanning Tunneling Microscope. *Phys. Rev. Lett.* **50**, 1998–2001 (1983).
187. Tersoff, J. & Hamann, D. R. Theory of the scanning tunneling microscope. *Physical Review B* **31**, 805–813 (1985).

188. Chen, C. J. Tunneling matrix elements in three-dimensional space: The derivative rule and the sum rule. *Physical Review B* **42**, 8841–8857 (1990).
189. Chen, C. J. Origin of atomic resolution on metal surfaces in scanning tunneling microscopy. *Physical Review Letters* **65**, 448–451 (1990).
190. Jones, R. O. Density functional theory: Its origins, rise to prominence, and future. *Rev. Mod. Phys.* **87**, 897–923 (2015).
191. Hohenberg, P. & Kohn, W. Inhomogeneous Electron Gas. *Phys. Rev.* **136**, B864–B871 (1964).
192. Kohn, W. & Sham, L. J. Self-Consistent Equations Including Exchange and Correlation Effects. *Phys. Rev.* **140**, A1133–A1138 (1965).
193. Cohen, A. J., Mori-Sánchez, P. & Yang, W. Challenges for Density Functional Theory. *Chemical Reviews* **112**, 289–320 (2012).
194. Burke, K. Perspective on density functional theory. *The Journal of Chemical Physics* **136**, 150901 (2012).
195. Larsen, A. H., Vanin, M., Mortensen, J. J., Thygesen, K. S. & Jacobsen, K. W. Localized atomic basis set in the projector augmented wave method. *Phys. Rev. B* **80**, 195112 (2009).
196. Mortensen, J. J., Hansen, L. B. & Jacobsen, K. W. Real-space grid implementation of the projector augmented wave method. *Phys. Rev. B* **71**, 035109 (2005).
197. Enkovaara, J. *et al.* Electronic structure calculations with GPAW: A real-space implementation of the projector augmented-wave method. *Journal of Physics Condensed Matter* **22** (2010).
198. Klimeš, J., Bowler, D. R. & Michaelides, A. Chemical accuracy for the van der Waals density functional. *Journal of Physics Condensed Matter* **22** (2010).
199. Hjorth Larsen, A. *et al.* The atomic simulation environment - A Python library for working with atoms. *Journal of Physics Condensed Matter* **29** (2017).
200. VandeVondele, J. *et al.* Quickstep: Fast and accurate density functional calculations using a mixed Gaussian and plane waves approach. *Computer Physics Communications* **167**, 103–128 (2005).

Appendix A

Bardeen Approach

The theory presented in section 4.1.1 are considerations of a series of results based on the Bardeen approach method [185], known as the Transfer Hamiltonian method, later improved by Tersoff and Hamann [186, 187] and Chen [188, 189]. Theoretical approaches described by the method, however simple they may seem, it brings a more fundamental understanding of some important physical quantities that enlight us how an STM actually works. For example, the tunnel current depends on the work function of the tip and sample, as well as the LDOS of the sample, the tip-sample interaction, the applied voltage, the shape of the tip apex, etc. These are properties that can vary during measurements and, therefore, influence the capture of images and contrasts, directly interfering on the interpretation of experimental results observed by the STM.

Bardeen initially proposed a one-particle process, i.e. mutual interactions between electrons are neglected which is a reasonable approximation in the low tunneling regime, and elastic tunneling, i.e. no loss of electron energy [95]. Looking at Figure A.1, both ψ^S and ψ^T states must satisfy the Schroedinger equation

$$i\hbar \frac{\partial \psi^i}{\partial t} = \left(-\frac{\hbar^2}{2m} \frac{\partial^2}{\partial z^2} + U_T + U_S \right) \psi^i \quad (\text{A.1})$$

with $\psi^i = \psi_\mu^i e^{-iE_\mu^i t/\hbar}$ depending on both spatial and temporal coordinates and U_T and U_S are tip and sample potential, respectively.

The time-evolution problem can be treated with perturbation theory. The essential objective is finding the probability in which the tip states will be populated by the electrons from sample, or vice-versa, depending on the bias applied. The state of the whole system can be represented by a linear combination as follows:

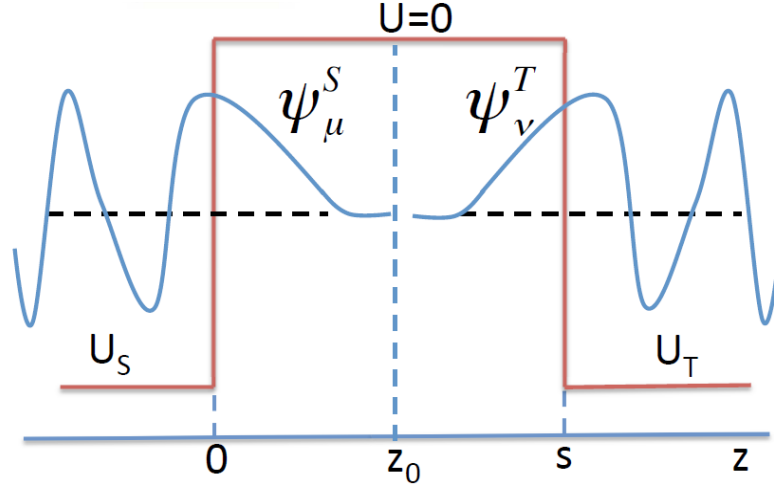


Figure A.1: Schematic illustration for the Bardeen approach to a one-dimensional potential well. The image shows the states of the approaching tip (ψ^T) and sample (ψ^S). The wave functions of both electrodes decay into the vacuum while the tunneling can only take place if they are sufficiently closer. Figure adapted from reference [95].

$$\psi = a_\mu(t)\psi_\mu^S e^{-iE_\mu^S t/\hbar} + \sum_{\nu=1}^{\infty} c_\nu(t)\psi_\nu^T e^{-iE_\nu^T t/\hbar} \quad (\text{A.2})$$

with $a_\mu(t)$ e $c_\nu(t)$ coefficients to be determined by A.1 and that $a_\mu(-\infty) = 1$ and $c_\nu(-\infty) = 0$. Notably, ψ^S and ψ^T originate from different Hamiltonians, but according to Bardeen approach, we shall assume approximately orthogonal states $\int \psi_\mu^{T*} \psi_\nu^S d^3r \approx 0$. Substituting A.2 in A.1 and projecting on the state ψ^T , we obtain the coefficient c_ν and consequently, the tunneling probability per unit time by $\frac{d|c_\nu(t)|^2}{dt}$ that becomes

$$P_{\mu\nu}(t) = \frac{2\pi}{\hbar} \delta(E_\mu^S - E_\nu^T) |M_{\mu\nu}|^2 \quad (\text{A.3})$$

the Fermi Golden-rule.

$M_{\mu\nu} = \langle \psi_\nu^T | U_T | \psi_\mu^S \rangle$ defines the tunneling matrix, which describes the projection of the initial ψ^S perturbed by the potential U_T of the tip onto the final ψ^T . If U_T is non-zero only in the T electrode volume (at $z > s$) in Figure A.1, the expression is validated only in that interval. The expression can be converted into a surface integral.

$$M_{\mu\nu} = \frac{\hbar^2}{2m} \int_{\Sigma} [\psi_\mu^S \nabla \psi_\nu^{T*} - \psi_\nu^{T*} \nabla \psi_\mu^S] \cdot d\vec{S} \quad (\text{A.4})$$

in which is calculated on the surface separation between the volume that defines sample and tip.

Therefore, the tunnel current is proportional to $P_{\mu\nu}(t)$ and the elastic tunneling is guaranteed by $\delta(E_\mu^S - E_\nu^T)$. Until now, we have dealt with the single state tunneling process $\psi_\mu^S \rightarrow \psi_\nu^T$, but the tip and substrate are characterized by a continuous spectrum, so we must sum over all μ and ν states. At elevated temperatures, the fermi edge can describe the occupied states by the Fermi-Dirac distribution $f(E - E_F) = (1 + \exp[(E - E_F)/K_B T])^{-1}$. Thus, assuming a bias voltage V between tip and sample, the tunnel current from sample at thermal equilibrium to the tip is:

$$I_{S \rightarrow T} = \frac{4\pi e}{\hbar} \sum_{\nu, \mu} f(E_\mu^S - E_F^S) [1 - f(E_\nu^T - E_F^T)] |M_{\mu\nu}|^2 \delta(E_\nu^T - E_\mu^S - eV) \quad (\text{A.5})$$

And from the tip to the sample:

$$I_{T \rightarrow S} = \frac{4\pi e}{\hbar} \sum_{\nu, \mu} f(E_\mu^T - E_F^T) [1 - f(E_\nu^S - E_F^S)] |M_{\mu\nu}|^2 \delta(E_\nu^T - E_\mu^S - eV) \quad (\text{A.6})$$

In order to consider both tip and sample density of states, $n(E) : \Sigma_\mu \rightarrow \int n(E) dE$ and considering approximations for $k_B T \ll 1$ and small bias voltage, the current is reduced to

$$I = \frac{4\pi e}{\hbar} V n^T(E_F^T) n^S(E_F^S) |M_{\mu\nu}|^2 \quad (\text{A.7})$$

where n^S and n^T are the density of states (DOS) of substrate and the tip, respectively. Therefore, by performing an STM experiment, we are accessing the occupied and unoccupied electronic states of the tip and sample, depending on the bias applied.

Notably, in Bardeens approach, knowing the convolution of the electronic states of the tip to sample is an important and crucial factor to derive the tunneling current. However, it is a great challenge to understand how tip states could be modified by different apex geometries. This motivated Tersoff and Hamann [187] to simplify these states into an arbitrarily localized one, treating it as a single atom with an s-wave function and a radius R located at the r_0 position relative to the surface sample. With this simplification, the tip properties can be factorized out of the problem and, consequently, the STM measurements results (or images) provides information of the surface alone.

The most relevant result of the TH model is that the tunneling matrix M is directly proportional to the value of the sample wave function evaluated at position r_0 . Considering the limit for small bias voltage V , the expression for tunneling conductance is

$$G \equiv \frac{I}{V} \approx 0.1 R^2 e^{2\gamma R} n^S(\vec{r}_0, E_F) \quad (\text{A.8})$$

$$n^S(\vec{r}_0, E_F) \equiv \sum \left| \psi_\mu^S(\vec{r}_0) \right|^2 \delta(E_\mu^S - E_F) \quad (\text{A.9})$$

where n^S is the local density of states (LDOS) of the sample at the Fermi level evaluated at r_0 tip center position.

The TH model proved to be very effective on the interpretation of images with characteristic sizes $\geq 10\text{\AA}$ (surface reconstruction, adsorbates on the sample, large defects, etc), but does not consider the complexity of convolution between electronic states of the tip and sample that may eventually occur in experimental observation. An extension of the TH approach proposed by Julian Chen introduced electronic states from the tip up to $l = 2$. In summary, the results show that the tunneling matrix elements M are related to the “derivatives” of the sample wave functions at the center of the apex atoms [189] with respect to z . Thus, in special for p_z and d_{z^2} orbitals, the density current is strongly affected and the consequent large corrugation amplitudes could be able to explain atomic resolution that was not well characterized by the TH s-wave approach. Indeed, tungsten or platinum-iridium alloy (PtIr) tips that present d_{z^2} localized states orbitals are extensively used in experiments to achieve atomic-resolution STM images.

Appendix B

Density Functional Theory calculations

Density Functional Theory (DFT) is a numerical approximation method used to describe the atomistic electronic structure. It is a technique that has been gaining a lot of strength and space in the fields of chemistry and physics for the last twenty years due to its practicality and efficiency in the study of molecular structures and chemical reactions in complex systems [190]. The theory has its origin in 1964 with Hohenberg and Kohn [191] who proved that the external potential of a system is a function of its most fundamental state. In other words, the electronic density $\rho(\mathbf{r})$ (observable in Cartesian space) is used to describe a complicated many-body physical problem and, from that, extract the ground state energy. In the following year, Kohn and Sham [192] formalized the method defining self-consistent equations that must be solved for a set of orbitals that yields the exact electronic structure $\rho(\mathbf{r})$ of the problem [193]. In a very succinct way, the Kohn-Sham theory formulates that the ground-state energy of a many-body system can be expressed as:

$$E[\rho] = T_s[\rho] + V_{ne}[\rho] + J[\rho] + E_{XC}[\rho] \quad (\text{B.1})$$

where T_s , V_{ne} , and J represent the explicit terms of kinetic energy, nucleus electrons potential energy, and the classical electron-electron repulsion energy, respectively. The key remaining term E_{XC} is the exchange-correlation functional that represents everything else defined to make the expression above exact [194]. Thus, the challenge of the method is summed up in the search for an effective functional that describes the effect of many

bodies using the single-particle formalism and reasonably represents the system under study.

Particularly, in the study described here, DFT is an important aid tool that allows us to reasonably describe the molecular geometry in its most fundamental adsorption configuration, accurately predict the dimension of the activation energy barriers of chemical reactions, as well as an acceptable description of van der Waals (intermolecular) interactions. Through the implemented calculations, we can draw conclusions and infer, from comparisons with the experimental results, which types of products and by-products are involved in the on-surface reactions. The main objective of this section is to indicate the employed codes, the atomic orbitals basis set, and the exchange-correlation functionals (XC) used in each studied system. All calculations and simulations were performed by our collaborators of the Yachay Tech University at the Imbabura cluster.

Cl₄TPP on Cu(111)

All DFT calculations were performed using a linear combination of atomic orbitals (LCAO) [195] with the projector-augmented wave method [196] code GPAW [197]. For the adsorbed species, we employed a double- ζ -polarized (DZP) basis set and for the surface of Cu(111), we used the single- ζ -polarized set (SZP). Three types of XC functions were used: (1) the generalized gradient approximation for the XC as implemented by Perdew, Burke and Ernzerhof (PBE) [141]; (2) the PBE including van der Waals (vdW) interactions at the Grimme’s D3 level (PBE-D3) [142] and (3) the PBE including vdW interactions self-consistently (vdW-DF2) [198].

We used a grid spacing of $h \approx 0.2 \text{ \AA}$ and performed structural relaxation of the relevant species until a maximum force of $\leq 0.03 \text{ eV/\AA}$ was obtained. To model the Cu(111) surface, we have employed a $15 \times 14 \times 3$ supercell of $3.823 \times 3.095 \times 2.417 \text{ nm}^3$, frozen to the experimental coordinates ($a = 0.361 \text{ nm}$), with more than 1.5 nm of vacuum between repeated slabs.

STM image simulations were performed with TH approximation [187] in a constant current mode using a bias of -1.5 V relative to the Fermi level as implemented in the atomic simulation environment (ASE) code [199]. To estimate the C-Cl and C-C bond distances in the transition states during direct dechlorination and a Cu adatom-mediated Ullmann coupling reaction, we have performed nudged elastic band calculations

for a chlorinated benzene with the anchoring C atom constrained to the same height and/or position as the relevant atom in Cl₄TPP was then estimated by fixing either the C-Cl or C-C bond distances and performing an otherwise unconstrained surface relaxation on the frozen Cu(111) surface slab.

Cl₄TPP on Ag(111)

All calculations were made by the generalized gradient approximation to the exchange and correlation PBE and Grimme’s D3 method (PBE-D3) [142] to include vdW interactions as we modeling physisorbed molecules.

Ag(111) surface was modeled using the experimental lattice constant $a = 4.09$ Å with the low adsorbate coverage limit modeled using $12 \times 12 \times 3$ slab ($3.471 \times 3.006 \times 2.506$ nm³) unit cell. Ag atoms were kept frozen and relaxing only the adsorbate. For the DFT calculations we used Quickstep (QS) [200] module of the CP2K code, which solves the electronic problem using a hybrid basis set approach that combines Gaussian and plane wave basis sets. All CP2K calculations employed a $3 \times 3 \times 1$ k -point mesh, an electron temperature of $T = 300$ K ≈ 25 meV, and adsorbates were structurally relaxed until a maximum force of ≈ 0.05 eV/Å was obtained.

DFT calculations were independently verified with the PAW method code GPAW [196, 197], employing a LCAO to represent the Kohn-Sham wave functions [195] with a SZP basis set for the Ag slab and DZP basis set for the adsorbates. We employed a grid spacing of $h \approx 0.2$ Å and electronic temperature of 0.1 eV.

All STM image simulations were performed with GPAW’s energy-resolved electronic density within the TH approximation [187] in constant current mode as implemented in the ASE code [199] to visualize states below the Fermi level.